

Technical Design Report for:

# $\bar{\text{PANDA}}$

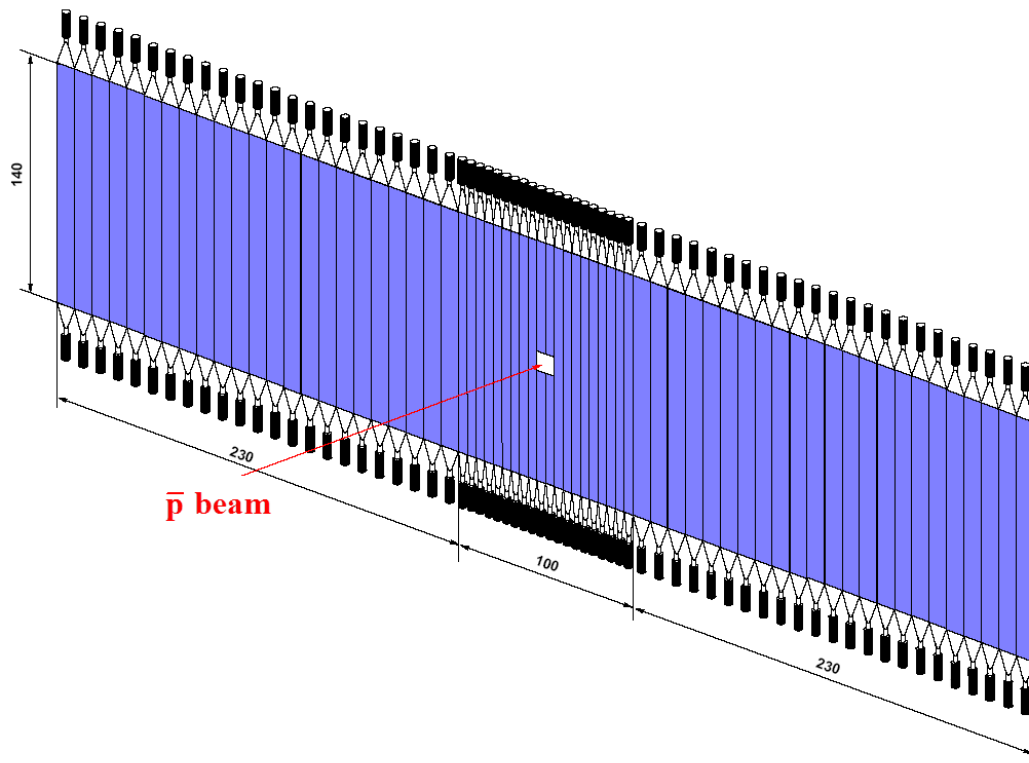
## Forward Time of Flight detector (FToF wall)

(AntiProton Annihilations at Darmstadt)

### Strong Interaction Studies with Antiprotons

$\bar{\text{PANDA}}$  Collaboration

January 19, 2018



**Cover:** General view of the forward time-of-flight (FToF) scintillation wall positioned at 7.5 meter downstream of the target in the Forward Spectrometer of the  $\bar{P}$ ANDA experiment. This document describes in details the design and performance of the FToF wall detector.

# The $\bar{P}$ ANDA Collaboration

2017-04-01 03:15:01

Aligarh Muslim University, Physics Department, **Aligarh**, India  
B. Singh

Universität Basel, **Basel**, Switzerland  
W. Erni, B. Krusche, M. Steinacher, N. Walford

Institute of High Energy Physics, Chinese Academy of Sciences, **Beijing**, China  
B. Liu, H. Liu, Z. Liu, X. Shen, C. Wang, J. Zhao

Ruhr-Universität Bochum, Institut für Experimentalphysik I, **Bochum**, Germany  
M. Albrecht, T. Erlen, F. Feldbauer, M. Fink, M. Fritsch, J. Haase, F.H. Heinsius, T. Held,  
T. Holtmann, I. Keshk, H. Koch, B. Kopf, M. Kuhlmann, M. Kümmel, S. Leiber, M. Mikirtychyants,  
P. Musiol, A. Mustafa, M. Pelizäus, A. Pitka, J. Pychy, M. Richter, C. Schnier, T. Schröder, C. Sowa,  
M. Steinke, T. Triffterer, U. Wiedner

Rheinische Friedrich-Wilhelms-Universität Bonn, **Bonn**, Germany  
M. Ball, R. Beck, C. Hammann, B. Ketzer, M. Kube, P. Mahlberg, M. Rossbach, C. Schmidt,  
R. Schmitz, U. Thoma, M. Urban, D. Walther, C. Wendel, A. Wilson

Università di Brescia, **Brescia**, Italy  
A. Bianconi

Institutul National de C&D pentru Fizica si Inginerie Nucleara "Horia Hulubei", **Bukarest-Magurele**,  
Romania  
M. Bragadireanu, D. Pantea

P.D. Patel Institute of Applied Science, Department of Physical Sciences, **Changa**, India  
B. Patel

University of Technology, Institute of Applied Informatics, **Cracow**, Poland  
W. Czyzycki, M. Domagala, G. Filo, J. Jaworowski, M. Krawczyk, E. Lisowski, F. Lisowski,  
M. Michałek, P. Poznański, J. Płazek

IFJ, Institute of Nuclear Physics PAN, **Cracow**, Poland  
K. Korcyl, A. Kozela, P. Kulesa, P. Lebedowicz, K. Pysz, W. Schäfer, A. Szczurek

AGH, University of Science and Technology, **Cracow**, Poland  
T. Fiutowski, M. Idzik, B. Mindur, K. Swientek

Instytut Fizyki, Uniwersytet Jagiellonski, **Cracow**, Poland  
J. Biernat, B. Kamys, S. Kistryn, G. Korcyl, W. Krzemien, A. Magiera, P. Moskal, A. Pyszniaik,  
Z. Rudy, P. Salabura, J. Smyrski, P. Strzempek, A. Wronska

FAIR, Facility for Antiproton and Ion Research in Europe, **Darmstadt**, Germany  
I. Augustin, R. Böhm, I. Lehmann, D. Nicmorus Marinescu, L. Schmitt, V. Varentsov

GSI Helmholtzzentrum für Schwerionenforschung GmbH, **Darmstadt**, Germany  
M. Al-Turany, A. Belias, H. Deppe, N. Divani Veis, R. Dzhygadlo, H. Flemming, A. Gerhardt,  
K. Götzen, A. Gromliuk, L. Gruber, R. Karabowicz, R. Kliemt, M. Krebs, U. Kurilla, D. Lehmann,  
S. Löchner, J. Lühning, U. Lynen, F. Nerling, H. Orth, M. Patsyuk, K. Peters, T. Saito, G. Schepers, C.  
J. Schmidt, C. Schwarz, J. Schwiening, A. Täschner, M. Traxler, C. Ugur, B. Voss, P. Wiczorek,  
A. Wilms, M. Zühlsdorf

Veksler-Baldin Laboratory of High Energies (VBLHE), Joint Institute for Nuclear Research, **Dubna**,  
Russia

V. Abazov, G. Alexeev, V. A. Arefiev, V. Astakhov, M. Yu. Barabanov, B. V. Batyunya, Y. Davydov,  
V. Kh. Dodokhov, A. Efremov, A. Fechtchenko, A. G. Fedunov, A. Galoyan, S. Grigoryan, E.

K. Koshurnikov, Y. Yu. Lobanov, V. I. Lobanov, A. F. Makarov, L. V. Malinina, V. Malyshev, A. G. Olshevskiy, E. Perevalova, A. A. Piskun, T. Pocheptsov, G. Pontecorvo, V. Rodionov, Y. Rogov, R. Salmin, A. Samartsev, M. G. Sapozhnikov, G. Shabratova, N. B. Skachkov, A. N. Skachkova, E. A. Strokovsky, M. Suleimanov, R. Teshev, V. Tokmenin, V. Uzhinsky, A. Vodopianov, S. A. Zaporozhets, N. I. Zhuravlev, A. Zinchenko

University of Edinburgh, **Edinburgh**, United Kingdom  
D. Branford, D. Glazier, D. Watts

Friedrich Alexander Universität Erlangen-Nürnberg, **Erlangen**, Germany  
M. Böhm, A. Britting, W. Eyrich, A. Lehmann, M. Pfaffinger, F. Uhlig

Northwestern University, **Evanston**, U.S.A.  
S. Dobbs, K. Seth, A. Tomaradze, T. Xiao

Università di Ferrara and INFN Sezione di Ferrara, **Ferrara**, Italy  
D. Bettoni, V. Carassiti, A. Cotta Ramusino, P. Dalpiaz, A. Drago, E. Fioravanti, I. Garzia, M. Savrie

Frankfurt Institute for Advanced Studies, **Frankfurt**, Germany  
V. Akishina, S. Gorbunov, I. Kisel, G. Kozlov, M. Pugach, M. Zyzak

INFN Laboratori Nazionali di Frascati, **Frascati**, Italy  
P. Gianotti, C. Guaraldo, V. Lucherini

INFN Sezione di Genova, **Genova**, Italy  
A. Bersani, G. Bracco, M. Macri, R. F. Parodi

Justus Liebig-Universität Gießen II. Physikalisches Institut, **Gießen**, Germany  
K. Biguenko, K.T. Brinkmann, V. Di Pietro, S. Diehl, V. Dormenev, M. Düren, E. Etzelmüller, M. Galuska, E. Gutz, C. Hahn, A. Hayrapetyan, M. Kesselkaul, K. Kreutzfeldt, W. Kühn, T. Kuske, J. S. Lange, Y. Liang, V. Metag, M. Moritz, M. Nanova, R. Novotny, T. Quagli, S. Reiter, A. Riccardi, J. Rieke, C. Rosenbaum, M. Schmidt, R. Schnell, H. Stenzel, U. Thöring, M. N. Wagner, T. Wasem, B. Wohlfahrt, H.G. Zaunick

IRFU, CEA, Université Paris-Saclay, **Gif-sur-Yvette Cedex**, France  
E. Tomasi-Gustafsson

University of Glasgow, **Glasgow**, United Kingdom  
D. Ireland, G. Rosner, B. Seitz

Birla Institute of Technology and Science, Pilani, K K Birla Goa Campus, **Goa**, India  
P.N. Deepak, A. Kulkarni

KVI-Center for Advanced Radiation Technology (CART), University of Groningen, **Groningen**, Netherlands

A. Apostolou, M. Babai, M. Kavatsyuk, P. J. Lemmens, M. Lindemulder, H. Loehner, J. Messchendorp, P. Schakel, H. Smit, M. Tiemens, J. C. van der Weele, R. Veenstra, S. Vejdani, S. Vejdani

Gauhati University, Physics Department, **Guwahati**, India  
K. Dutta, K. Kalita

Indian Institute of Technology Indore, School of Science, **Indore**, India  
A. Kumar, A. Roy

Fachhochschule Südwestfalen, **Iserlohn**, Germany  
H. Sohlbach

Forschungszentrum Jülich, Institut für Kernphysik, **Jülich**, Germany  
M. Bai, L. Bianchi, M. Büscher, L. Cao, A. Cebulla, R. Dossall, A. Erven, V. Fracassi, A. Gillitzer, F. Goldenbaum, D. Grunwald, A. Herten, Q. Hu, L. Jokhovets, G. Kemmerling, H. Kleines, A. Lai, A. Lehrach, R. Nellen, H. Ohm, S. Orfanitski, D. Prasuhn, E. Precipe, J. Pütz, J. Ritman, E. Rosenthal, S. Schadmand, T. Seifick, V. Serdyuk, G. Sterzenbach, T. Stockmanns, P. Wintz, P. Wüstner, H. Xu

Chinese Academy of Science, Institute of Modern Physics, **Lanzhou**, China  
S. Li, Z. Li, Z. Sun, H. Xu

INFN Laboratori Nazionali di Legnaro, **Legnaro**, Italy  
V. Rigato

Lunds Universitet, Department of Physics, **Lund**, Sweden  
L. Isaksson

Johannes Gutenberg-Universität, Institut für Kernphysik, **Mainz**, Germany  
P. Achenbach, A. Aycock, O. Corell, A. Denig, M. Distler, M. Hoek, A. Karavdina, W. Lauth, Z. Liu,  
H. Merkel, U. Müller, J. Pochodzalla, S. Sanchez, S. Schlimme, C. Sfienti, M. Thiel

Helmholtz-Institut Mainz, **Mainz**, Germany  
H. Ahmadi, S. Ahmed, S. Bleser, L. Capozza, M. Cardinali, A. Dbeyssi, M. Deiseroth, A. Ehret,  
B. Fröhlich, D. Kang, D. Khanef, R. Klasen, H. H. Leithoff, D. Lin, F. Maas, S. Maldaner,  
M. Martínez, M. Michel, M. C. Mora Espí, C. Morales Morales, C. Motzko, O. Noll, S. Pflüger,  
D. Rodríguez Piñeiro, A. Sanchez-Lorente, M. Steinen, R. Valente, M. Zambrana, I. Zimmermann

Research Institute for Nuclear Problems, Belarus State University, **Minsk**, Belarus  
A. Fedorov, M. Korjik, O. Missevitch

Moscow Power Engineering Institute, **Moscow**, Russia  
A. Balashoff, A. Boukharov, O. Malyshev, I. Marishev

Institute for Theoretical and Experimental Physics, **Moscow**, Russia  
P. Balanutsa, V. Balanutsa, V. Chernetsky, A. Demekhin, A. Dolgolenko, P. Fedorets, A. Gerasimov,  
V. Goryachev

Nuclear Physics Division, Bhabha Atomic Research Centre, **Mumbai**, India  
V. Chandratre, V. Datar, D. Dutta, V. Jha, H. Kumawat, A.K. Mohanty, A. Parmar, A. K. Rai,  
B. Roy, G. Sonika

Westfälische Wilhelms-Universität Münster, **Münster**, Germany  
C. Fritzs, S. Grieser, A.K. Hergemöller, B. Hetz, N. Hüsken, A. Khoukaz, J. P. Wessels

Suranaree University of Technology, **Nakhon Ratchasima**, Thailand  
K. Khosonthongkee, C. Kobdaj, A. Limphirat, P. Srisawad, Y. Yan

Budker Institute of Nuclear Physics, **Novosibirsk**, Russia  
E. Antokhin, A. Yu. Barnyakov, M. Barnyakov, K. Beloborodov, V. E. Blinov, V. S. Bobrovnikov, I.  
A. Kuyanov, K. Martin, A. P. Onuchin, S. Pivovarov, E. Pyata, S. Serednyakov, A. Sokolov,  
Y. Tikhonov

Novosibirsk State University, **Novosibirsk**, Russia  
A. E. Blinov, S. Kononov, E. A. Kravchenko

Institut de Physique Nucléaire, CNRS-IN2P3, Univ. Paris-Sud, Université Paris-Saclay, 91406, **Orsay**  
**cedex**, France

E. Atomssa, R. Kunne, D. Marchand, B. Ramstein, J. van de Wiele, Y. Wang

Dipartimento di Fisica, Università di Pavia, INFN Sezione di Pavia, **Pavia**, Italy  
G. Boca, S. Costanza, P. Genova, P. Montagna, A. Rotondi

Charles University, Faculty of Mathematics and Physics, **Prague**, Czech Republic  
M. Bodlak, M. Finger, M. Finger, A. Nikolovova, M. Pesek, M. Peskova, M. Pfeffer, I. Prochazka,  
M. Slunicka

Czech Technical University, Faculty of Nuclear Sciences and Physical Engineering, **Prague**, Czech  
Republic

P. Gallus, V. Jary, J. Novy, M. Tomasek, M. Virius, V. Vrba

Institute for High Energy Physics, **Protvino**, Russia  
V. Abramov, N. Belikov, S. Bukreeva, A. Davidenko, A. Derevschikov, Y. Goncharenko, V. Grishin,  
V. Kachanov, V. Kormilitsin, A. Levin, Y. Melnik, N. Minaev, V. Mochalov, D. Morozov, L. Nogach,  
S. Poslavskiy, A. Ryazantsev, S. Ryzhikov, P. Semenov, I. Shein, A. Uzunian, A. Vasiliev, A. Yakutin

Sikaha-Bhavana, Visva-Bharati, WB, **Santiniketan**, India  
U. Roy

University of Sidney, School of Physics, **Sidney**, Australia  
B. Yabsley

National Research Centre "Kurchatov Institute" B. P. Konstantinov Petersburg Nuclear Physics  
Institute, Gatchina, **St. Petersburg**, Russia  
S. Belostotski, G. Gavrilov, A. Izotov, S. Manaenkov, O. Miklukho, D. Veretennikov, A. Zhdanov  
Stockholms Universitet, **Stockholm**, Sweden  
K. Makonyi, M. Preston, P.E. Tegner, D. Wölbing  
Kungliga Tekniska Högskolan, **Stockholm**, Sweden  
T. Bäck, B. Cederwall

Veer Narmad South Gujarat University, Department of Physics, **Surat**, India  
S. Godre

Politecnico di Torino and INFN Sezione di Torino, **Torino**, Italy  
F. Balestra, F. Iazzi, R. Introzzi, A. Lavagno, J. Olave

Università di Torino and INFN Sezione di Torino, **Torino**, Italy  
A. Amoroso, M. P. Bussa, L. Busso, M. Destefanis, L. Fava, L. Ferrero, M. Greco, J. Hu, L. Lavezzi,  
M. Maggiora, G. Maniscalco, S. Marcello, S. Sosio, S. Spataro

INFN Sezione di Torino, **Torino**, Italy  
D. Calvo, S. Coli, P. De Remigis, A. Filippi, G. Giraud, S. Lusso, G. Mazza, M. Mignone, A. Rivetti,  
R. Wheadon

Università di Trieste and INFN Sezione di Trieste, **Trieste**, Italy  
R. Birsa, F. Bradamante, A. Bressan, A. Martin

Uppsala Universitet, Institutionen för fysik och astronomi, **Uppsala**, Sweden  
H. Calen, W. Ikegami Andersson, T. Johansson, A. Kupsc, P. Marciniowski, M. Papenbrock,  
J. Pettersson, K. Schönning, M. Wolke

The Svedberg Laboratory, **Uppsala**, Sweden  
B. Galnander

Instituto de Física Corpuscular, Universidad de Valencia-CSIC, **Valencia**, Spain  
J. Diaz

Sardar Patel University, Physics Department, **Vallabh Vidynagar**, India  
V. Pothodi Chackara

National Centre for Nuclear Research, **Warsaw**, Poland  
A. Chlopik, G. Kesik, D. Melnychuk, B. Slowinski, A. Trzcinski, M. Wojciechowski, S. Wronka,  
B. Zwieglinski

Österreichische Akademie der Wissenschaften, Stefan Meyer Institut für Subatomare Physik, **Wien**,  
Austria  
P. Bühler, J. Marton, D. Steinschaden, K. Suzuki, E. Widmann, S. Zimmermann, J. Zmeskal

Editors:	Stanislav Belostotski	Email: <a href="mailto:belostot@mail.desy.de">belostot@mail.desy.de</a>
	Anton Izotov	Email: <a href="mailto:izotov@mail.desy.de">izotov@mail.desy.de</a>
	Oleg Miklukho	Email: <a href="mailto:miklukho@pnpi.spb.ru">miklukho@pnpi.spb.ru</a>
	Yury Naryshkin	Email: <a href="mailto:yury.naryshkin@cern.ch">yury.naryshkin@cern.ch</a>
	Denis Veretennikov	Email: <a href="mailto:denis_v@mail.desy.de">denis_v@mail.desy.de</a>
	Andrei Zhdanov	Email: <a href="mailto:zhdanov@pnpi.spb.ru">zhdanov@pnpi.spb.ru</a>
Technical Coordinator:	Lars Schmitt	Email: <a href="mailto:l.schmitt@gsi.de">l.schmitt@gsi.de</a>
Deputy:	Anastasios Belias	Email: <a href="mailto:a.belias@gsi.de">a.belias@gsi.de</a>
Spokesperson:	Klaus Peters	Email: <a href="mailto:k.peters@gsi.de">k.peters@gsi.de</a>
Deputy:	Tord Johansson	Email: <a href="mailto:tord.johansson@physics.uu.se">tord.johansson@physics.uu.se</a>

---



## Preface

This document is a Technical Design Report (TDR) which presents the status of the  $\overline{\text{PANDA}}$  Forward Time-of-Flight (FToF) wall design. The FToF wall is a system of large scintillation counters which intends to detect, per event basis the timestamps of particles emitted within the acceptance of the  $\overline{\text{PANDA}}$  Forward spectrometer. The overall timing resolution of the system is better than 100 ps. The FToF wall is assumed to be used for Particle Identification (PID) of forward going hadrons with momenta below 4 GeV by time-of-flight criterion.

---

The use of registered names, trademarks, *etc.* in this publication does not imply, even in the absence of specific statement, that such names are exempt from the relevant laws and regulations and therefore free for general use.

# Contents

---

<b>Preface</b>	<b>ix</b>	References . . . . .	22
<b>1 Executive summary</b>	<b>1</b>	<b>4 Physics case of FToF, MC study</b>	<b>25</b>
1.1 The scientific program of the PANDA experiment . . . . .	1	4.1 Forward spectrometer time-of-flight PID . . . . .	25
1.2 The PANDA spectrometer and Time-of-Flight detectors . . . . .	1	4.2 Count rate and background estimations . . . . .	27
1.3 The Forward ToF wall functions . . . . .	3	4.3 $\Lambda$ hyperon detection with FToF wall . . . . .	32
1.4 Technical requirements for the FToF wall . . . . .	3	4.4 Interplay between FToF wall and SciTil detectors . . . . .	33
1.5 The Forward ToF wall design . . . . .	3	4.5 Time-dependent Monte Carlo simulation . . . . .	36
1.6 Prototyping . . . . .	4	4.6 Optimization of the scintillator thickness and light guide configuration . . . . .	36
1.7 Monte Carlo simulation . . . . .	4	4.7 PID and time resolution variants . . . . .	37
1.8 Design validation . . . . .	5	References . . . . .	37
References . . . . .	5	<b>5 Experimental study of prototypes</b>	<b>39</b>
<b>2 The PANDA experiment</b>	<b>7</b>	5.1 Study of photodetectors using test-station . . . . .	39
2.1 High Energy Storage Ring (HESR) . . . . .	7	5.1.1 Test-station. General remarks. . . . .	39
2.2 The targets . . . . .	7	5.1.2 Investigation of PMTs . . . . .	39
2.3 The Detector . . . . .	8	5.1.3 Measurement of SiPM characteristics . . . . .	40
2.4 Target Spectrometer . . . . .	8	5.2 Study of prototypes using proton beam . . . . .	43
2.5 Forward Spectrometer . . . . .	10	5.2.1 Introduction . . . . .	43
2.6 Particle identification system . . . . .	10	5.2.2 Test of scintillation counter prototypes at the PNPI synchrotron . . . . .	43
2.7 Data Acquisition . . . . .	10	5.2.3 Readout electronics . . . . .	45
2.8 Infrastructure . . . . .	11	5.2.4 Data analysis . . . . .	46
References . . . . .	11	5.2.5 Tests with 730 MeV protons . . . . .	48
<b>3 Technical design considerations of the FToF wall</b>	<b>13</b>	5.2.6 Tests with 920 MeV protons . . . . .	48
3.1 General requirements . . . . .	13	5.2.7 Measurements with 2000 MeV proton test beam of COSY accelerator . . . . .	49
3.2 Plastic scintillators . . . . .	13	5.2.8 Comments on the necessity of hit position measurements and time resolution . . . . .	51
3.3 Energy depositions and dynamic range . . . . .	14		
3.4 Selection of photodetectors . . . . .	16		
3.4.1 Photomultiplier Tubes . . . . .	16		
3.4.2 Silicon Photomultipliers . . . . .	17		
3.5 Readout electronics . . . . .	17		
3.6 Mechanics, cabling, integration . . . . .	20		
3.7 Safety regulation . . . . .	20		
3.8 Summary . . . . .	20		

5.3	Summary of experimental study of prototypes . . . . .	52
5.4	Outlook for further experimental studies . . . . .	54
	References . . . . .	55
<b>6</b>	<b>Calibration and monitoring</b>	<b>57</b>
	References . . . . .	58
<b>7</b>	<b>Project management</b>	<b>59</b>
7.1	Responsibility . . . . .	59
7.2	Work packages . . . . .	59
7.3	Timelines and milestones . . . . .	59
<b>8</b>	<b>Conclusion</b>	<b>63</b>
	<b>Acknowledgments</b>	<b>64</b>

# 1 Executive summary

---

## 1.1 The scientific program of the $\bar{\text{P}}\text{ANDA}$ experiment

The  $\bar{\text{P}}\text{ANDA}$  (AntiProton ANihilation at DArmstadt) experiment [1] is one of the key projects at the future Facility for Antiproton and Ion Research (FAIR), which is currently under construction at GSI, Darmstadt. The FAIR accelerators will deliver primary proton and ion beams, as well as secondary beams of  $\bar{p}$  or radioactive ions of high intensity and high quality.

The  $\bar{\text{P}}\text{ANDA}$  experiment will perform precise studies of  $\bar{p}p$  annihilations and reactions of  $\bar{p}$  with nucleons of heavier nuclear targets. It will benefit from  $\bar{p}$  beams with unprecedented intensity and quality provided by the High Energy Storage Ring (HESR) in the momentum range from 1.5 to 15 GeV/c. In a high momentum resolution mode (HR) of HESR the relative momentum spread of the beam is reduced to  $5 \times 10^{-5}$  with  $10^{10}$  circulating  $\bar{p}$  at the peak luminosity of  $2 \times 10^{31} \text{cm}^{-2} \text{s}^{-1}$ . In a high luminosity mode (HL) the peak luminosity reaches  $2 \times 10^{32} \text{cm}^{-2} \text{s}^{-1}$  at the same target density. The relative momentum spread in this regime is expected to be about  $10^{-4}$ . The HR and HL modes are established to meet the challenging requirements of the  $\bar{\text{P}}\text{ANDA}$  experimental program.

The  $\bar{\text{P}}\text{ANDA}$  experiment exploits an extraordinary physics potential of the projected high quality  $\bar{p}$  beams. The main experimental topics of the hadron physics program [2][3][4] are briefly itemized in the following.

Charmonium Spectroscopy. Precise measurements of all states below and above the open charm threshold is of great importance for QCD. All charmonium states can be formed directly in  $\bar{p}p$  annihilation in the invariant mass range  $2.25 < M(\bar{p}p) < 5.46$  GeV. At full luminosity,  $\bar{\text{P}}\text{ANDA}$  will be able to collect several thousand  $\bar{c}c$  states per day. By means of beam momentum scans, it will be possible to measure masses with accuracies of the order of 100 keV and widths to 10%, or better.

Search for Gluonic Excitations. One of the main challenges of hadron physics is a search for gluonic excitations: i.e., hadrons consisting of pure glue and hybrids, which consist of a  $\bar{q}q$  pair and excited glue. Due to additional gluon degrees of freedom,

these objects may have exotic quantum numbers  $J/\psi$ , which make their experimental identification easier. Specifically, further exploration of recently discovered  $X$ ,  $Y$ , and  $Z$  ( $\bar{c}c$  like) states is assumed, as well as searches for multi-quark (quark molecule) states.

Electromagnetic Processes. It has been shown that a study of proton form factors is feasible in the time-like region by measuring the  $\bar{p}p \rightarrow e^+e^-$  exclusive channel up to  $S = 14$  GeV<sup>2</sup>. The statistical precision of these measurements is expected to surpass essentially that of the existing to date world data. In order to access the “unphysical region”  $S < (2M_p)^2$  the inelastic  $\bar{p}p \rightarrow e^+e^-\pi^0$  channel is also planned to be studied.

Study of Hadrons in Nuclear Matter. So far, experiments have been focused on the light quark sector. The high-intensity  $\bar{p}$  beam of up to 15 GeV/c will allow one an extension of this program to the charm sector both for hadrons with hidden and open charm.

Hyperon Physics. The  $\bar{p}$  beam at FAIR allows to efficiently produce hypernuclei with more than one strange hadron, making  $\bar{\text{P}}\text{ANDA}$  competitive with the planned dedicated experiments. Another aspect of the hyperon (and charm) physics is the measurement of the cross sections and polarization parameters in exclusive reactions like  $\bar{p}p \rightarrow \bar{\Lambda}\Lambda$ ,  $\bar{p}p \rightarrow \bar{\Xi}\Xi$ ,  $\bar{p}p \rightarrow \bar{\Omega}\Omega$ ,  $\bar{p}p \rightarrow \bar{\Lambda}_c\Lambda_c$ . The study of production of multi-strange and charm baryons is of particular interest.

There are also many other important and challenging topics, like, e.g., CP violation in the hyperon sector, which are still under investigation and not presented in the experimental program discussed above.

## 1.2 The $\bar{\text{P}}\text{ANDA}$ spectrometer and Time-of-Flight detectors

The  $\bar{\text{P}}\text{ANDA}$  experiment is designed to achieve  $4\pi$  solid angle coverage, high resolution for tracking, good particle identification, high precision calorimetry, high rate capabilities, with a versatile readout and event selection. A detailed description of the  $\bar{\text{P}}\text{ANDA}$  detector can be found in

Ref.[5]. The  $\bar{p}$  beam interacts with a cluster or pellet hydrogen target, or with a deuterium or heavy nucleus target. The detector is composed of two magnetic spectrometers: the Target Spectrometer (TS), based on a superconducting solenoid magnet and the Forward Spectrometer (FS) based on a dipole magnet. The TS is designed to provide a  $4\pi$  solid angle coverage around interaction point, while the FS is used to cover small polar angles in the forward region.

The  $\bar{\text{P}}\text{ANDA}$  spectrometers comprise a variety of sub-detectors dedicated to measure tracks of produced particles, their energy deposit, Cerenkov light and timing. The most important characteristics are listed below:

- Possibility of mass scan with resolution of 100 keV
- Event rate capability of  $2 \times 10^7 \text{ s}^{-1}$
- Practically  $4\pi$  acceptance with high detection efficiency
- Momentum resolution of 0.01
- Event start time reconstruction at picosecond level
- Good enough secondary vertex resolution (e.g. for  $D$ -meson decay reconstruction)
- Excellent particle identification ( $\gamma$ ,  $e$ ,  $\mu$ ,  $\pi$ ,  $K$ ,  $p$ )
- Wide range of photon detection (1 MeV - 10 GeV)

In this report, timing measurements are of particular interest. Timing information is foreseen in several  $\bar{\text{P}}\text{ANDA}$  sub-detectors (e.g. barrel DIRC or Forward RICH). The high time resolution at the picosecond level will be provided for the  $\bar{\text{P}}\text{ANDA}$  experiment with two dedicated time-of-flight detectors: the Barrel ToF in the TS and the Forward ToF wall in the FS.

In addition, the dipole ToF detector was proposed for detection of low momentum particles strongly deflected to the left and to the right by the magnetic field within the dipole. The dipole ToF would consist of two sets of scintillation counters (left and right sub-detector) to detect particles of the opposite charges. It was conceived to equip each sub-detector with 10 scintillation counters placed in the rear part of the dipole magnet. The height of scintillation slabs and their width was

preliminary designed to be 100 and 10 cm, respectively, thus that each sub-detector formed a wall with sensitive area of 100 by 100  $\text{cm}^2$ .

Given a high level of the magnetic field in the dipole, magnetic-field-protected photo-detectors must be utilized for the dipole TOF readout. According to tests in PNPI the PMT187, production of the “Electron” firm in St. Petersburg, could stand (keeping its high timing resolution properties) against magnetic field up to 0.5 T. The latter is essentially less than the level of magnetic field in the rear part of the dipole. In general, using PMTs looks unrealistic in this case.

Another option is to use SiPM’s (Avalanche Micro-Pixel Photo Diodes). Thus investigation of timing characteristics of KETEK PM6660 with sensitive to irradiated photons active area of 36  $\text{mm}^2$  showed a very promising result: time resolution ( $\sigma$ ) of 66 ps has been measured. Practical application of SiPMs will however require additional R&D like thorough study of their radiation hardness, design of appropriate readout, cooling problem, etc. Also, the dipole TOF technical design must comply with design of the  $\bar{\text{P}}\text{ANDA}$  Forward Tracking system (FT). The latter has not yet been totally finalized.

The dipole TOF configuration was not optimized as it ought to be a subject to a Monte Carlo study based on specific physics cases. Previously done Monte Carlo simulations showed that the count rate of the secondary hadrons detected with the dipole TOF detector at maximum luminosity is in general very low. Additional MC simulations which would include several benchmark reactions according to the  $\bar{\text{P}}\text{ANDA}$  experimental program are needed to demonstrate importance and necessity of the dipole TOF detector. Proceeding from the above considerations the dipole ToF is not included in this TDR which is dedicated to the ToF wall only. However, given strong physics motivations for the dipole TOF are demonstrated it will be presented in a separate document later.

The PNPI group from the National Research Center “Kurchatov Institute”, B.P.KONSTANTINOV PETERSBURG NUCLEAR PHYSICS INSTITUTE is responsible for the design and construction of the Forward Time-of-Flight (FToF) wall which is presented in the report. The PNPI group is the only one working on this project.

The FToF wall detector is essential both for the startup period when the Modular Start Version (MSV) of the  $\bar{\text{P}}\text{ANDA}$  experiment will be realized

and for the data taking period with  $\overline{\text{PANDA}}$  in its full configuration.

### 1.3 The Forward ToF wall functions

Particle identification of low momentum hadrons. One important function of the FToF wall is to measure the time of flight of forward particles emitted within the FS acceptance under laboratory angles below  $5^\circ$  and  $10^\circ$  in the vertical and horizontal directions, respectively. The wall is assumed to be positioned at 7.5 m downstream of the  $\overline{\text{PANDA}}$  target. Being positioned downstream of the FS dipole, it must have a large sensitive area: 560 cm (width)  $\times$  140 cm (height). Together with the information on the particle momentum and its track length as provided by the dipole spectrometer equipped with the forward tracking system (FT), the FToF wall should identify the hadrons ( $\pi$ ,  $K$  and  $p$  and their antiparticles) by the time-of-flight criterion. A reliable  $p/K$  and  $K/\pi$  separation is possible at the momenta below 4.3 and 3 GeV, respectively, provided that the time resolution of the FToF detector is better than 100 ps. Note that this low momentum range is typically below the FRICH thresholds where there is no guarantee for the hadron detection with a high efficiency.

No dedicated start counter in the interaction point area is foreseen for the  $\overline{\text{PANDA}}$  detector. The time-of-flight information is assumed to be obtained by using the time correlations between the responses of two or more scintillation counters of the FToF wall. Additionally, the combined information of the FToF wall and Barrel ToF can be used. The time of flight is extracted offline, partly in the combination with other criteria, similar to the HADES experiment at GSI [6].

Determination of the event start  $T_0$ . As it has been mentioned above, there is no dedicated start counter in the  $\overline{\text{PANDA}}$  spectrometer design. On the other hand, the determination of the antiproton-target interaction time stamp (event start)  $T_0$  is one of the crucial point for data analysis. The time stamp of a particle detected with a FToF wall counter, may be used for the rough determination of the  $T_0$ . For a relativistic particle, time-of-flight from the Interaction Point to the FToF wall position is about  $25 + \Delta$  ns where  $\Delta$  is not a large additional time-variation due to the sort of a particle, its scattering angle and momentum analyzed with the help of the FS. Thus

for the momenta larger than 1 GeV  $\Delta$  is typically less than 20 ns. The  $T_0$  can be determined much more precisely if a FToF wall particle hit is independently identified, e.g., with FRICH or Forward (Shashlyk) Calorimeter, or Forward Muon range system, and the particle track is reconstructed with the FT system. A procedure of the  $T_0$  determination is also worked out independently by the BToF group which makes  $T_0$  extraction very reliable and precise in the  $\overline{\text{PANDA}}$  detector, in particular, when the two detectors are involved.

Providing information on energy deposition. The energy deposition of the particles detected with the FToF wall is estimated to vary from 5 to 50 MeV (Sec. 3.3). Once using the time-over-threshold (TOT) method for the amplitude correction in timing measurements, this information is automatically available and can be extracted.

### 1.4 Technical requirements for the FToF wall

The main technical conditions are listed below:

- The time resolution must be better than 100 ps
- The FToF wall is positioned at 7.5 m downstream of the target
- The sensitive area of the scintillation wall is 5.6 m (width)  $\times$  1.4 m (height)
- The scintillation wall should withstand a high counting rate corresponding to the maximal luminosity of the  $\overline{\text{PANDA}}$  experiment
- The dynamic range of the detector should cover all possible variations of energy deposition in the scintillators

### 1.5 The Forward ToF wall design

The technical requirements can be satisfied using commercially available components. The detector is modularized to be built of scintillation counters assembled of plastic scintillation slabs with good timing characteristics (e.g. Bicron 408) and the fast PMT readout. The counters are placed at 7.5 m downstream of the target, forming the wall with a sensitive area according to the technical requirements.

The wall consists of 66 scintillation counters: 20 counters in the central part and 46 counters in the side parts (23 counters on each side). The height of all the plastic scintillator slabs is 140 cm, and their thickness is 2.5 cm, while the width of the slabs is 5 cm and 10 cm for the central and side parts, respectively. Each scintillator is coupled on both ends by fast PMTs. The Hamamatsu PMTs R4998 (1") and R2083 (2"), for the slabs of 5 and 10 cm width will be used, respectively. There are many firms around the world producing photomultiplier tubes. There are also some firms in Russia (e.g. "Electron" in St.Petersburg). According to our opinion, the Hamamatsu PMTs can be characterized as the most reliable with a well-guaranteed specification. The R4998 and R2083 Hamamatsu tubes have been tested by us during a long period in the process of prototyping together with some other PMTs. The performance of the Hamamatsu PMT was found to be the best. The light guides made of Plexiglas are of the truncated cone (fish tail) configuration with different dimensions for the PMT of 1" or 2" diameter. In the center of the wall a rectangular hole (size: 20 cm  $\times$  20 cm) is left open through which the beam pipe passes. It is placed off-center because of the deflection of the circulating beam by the PANDA dipole. The readout electronics is based on FPGA systems with four TRB-3 platforms and 18 PADIWA3 front-end interface [7, 8, 9] modules. The supporting frame of the FToF detector is positioned on a rail. An option to roll out the system to the service position is foreseen.

## 1.6 Prototyping

All the photodetectors used for prototyping were preliminary tested at the PNPI test station using electrons from  $\beta$ -decay of the radioactive  $^{90}\text{Sr}$  source. After the correction for the time walk, the time resolution of about 40-50 ps has been obtained for the Hamamatsu R4998 and 2083 PMTs.

The tests with large scintillators have been performed using the proton beams of the PNPI synchrocyclotron and the COSY accelerator in Jülich. The final tests have been made in PNPI with the help of the MAP magnetic spectrometer selecting the 920 MeV secondary protons elastically scattered off a hydrogen target. The scintillation counter prototypes were placed in the focal plane of the spectrometer. The momentum resolution was about 1%. The hit position on the slab was determined with 1 mm precision. The dependencies of the time resolution on the hit position, en-

**Table 1.1:** Samples of scintillation counters tested using 920 MeV protons at PNPI

Slab dimensions, cm	Photomultiplier tube	Time resolution (weighted mean), ps
140 $\times$ 10 $\times$ 2.5	Hamamatsu R2083	65
140 $\times$ 5 $\times$ 2.5	Hamamatsu R4998	60

ergy deposition (scintillator thickness), scintillation slab width and count rate load were investigated. The raw time resolution ( $\sigma$ ) varied from 140 to 230 ps. After applying the amplitude and hit position corrections the resolution better than 100 ps was obtained (the weighted mean of both PMTs:  $1/\sigma^2 = 1/\sigma_{PMT1}^2 + 1/\sigma_{PMT2}^2$ ). It must be noted that the variations of the time resolution  $\sigma$  along the plastic scintillator were found to be small. The selected prototypes scintillation counters are given in Table 1.1.

## 1.7 Monte Carlo simulation

A number of Monte Carlo (MC) studies have been performed in order to validate the detector design. It has been shown that at the maximal luminosity ( $2 \times 10^{32} \text{ cm}^2\text{s}^{-1}$ ) the overall counting rate in the central part of the FToF wall will not exceed 2 MHz, which determines the detector granularity. The latter is also a compromise on the detector cost. The background from the secondary  $e^+e^-$  pairs is negligible at the lepton momenta above 2 GeV. It stays below  $10^5 \text{ s}^{-1}$  at the smaller momenta.

At a 10 GeV  $\bar{p}$  beam, the multiple hit probability in the FToF wall is almost 50% and the probability of FToF $\times$ BToF coincidences is about 40%. These numbers are essential for the efficiency of the time-of-flight analysis.

It has been shown that the intensive  $\bar{\Lambda}$  peak is autonomously reconstructed with the FToF wall which can be used for the detector tuning and calibration.

## 1.8 Design validation

The design is validated by Monte Carlo simulations. The timing resolution of the large scintillation counter has been experimentally measured and the resolution ( $\sigma$ ) below 100 ps has been obtained. The results of the experimental “on-beam” tests meet the requirements of the PANDA experiment.

## References

- [1] M. Kotulla et al. Strong interaction studies with antiprotons. Letter of intent for PANDA (Antiproton Annihilations at Darmstadt). 2004.
- [2] Nora Brambilla and Ulf-G. Meißner. Studies of Hadron Structure and Interactions with the PANDA Experiment at FAIR. 2015.
- [3] B. Singh. Study of doubly strange systems using stored antiprotons. *Nucl. Phys.*, A954:323–340, 2016.
- [4] M. F. M. Lutz et al. Physics Performance Report for PANDA: Strong Interaction Studies with Antiprotons. 2009.
- [5] M. Kotulla et al. Technical Progress Report for PANDA: Strong Interaction Studies with Antiprotons. 2005.
- [6] G. Agakishiev et al. The High-Acceptance Dielectron Spectrometer HADES. *Eur. Phys. J.*, A41:243–277, 2009.
- [7] A. Neiser et al. TRB3: a 264 channel high precision TDC platform and its applications. *JINST*, 8:C12043, 2013.
- [8] I. Fröhlich et al. TRB for HADES and FAIR experiments at GSI. In *Astroparticle, particle and space physics, detectors and medical physics applications. Proceedings, 10th Conference, ICATPP 2007, Como, Italy, October 8-12, 2007*, pages 973–977, 2008.
- [9] F. Gonnella, V. Kozhuharov, and M. Raggi. Time over threshold in the presence of noise. *Nucl. Instrum. Meth.*, A791:16–21, 2015.



## 2 The $\bar{\text{P}}\text{ANDA}$ experiment

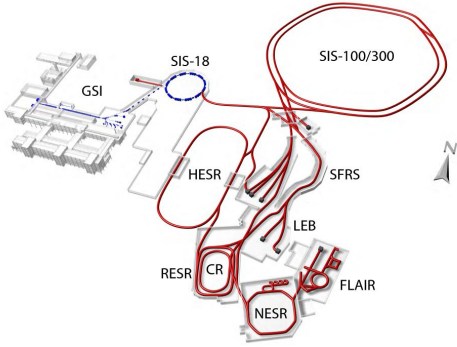


**Figure 2.1:** Schematic view of the FAIR layout incorporating the current GSI installations and future installations: the SIS100 synchrotron the storage and cooler ring complex including CR (RESR) and HESR

### 2.1 High Energy Storage Ring (HESR)

A schematic view of the future FAIR layout with the HESR [1] and HESR lattice with the  $\bar{\text{P}}\text{ANDA}$  setup are shown in Fig. 2.1 and Fig. 2.2. The HESR is designed to store  $10^{11}$  antiprotons. For the startup (MSV) period, FAIR will provide  $10^{10}$  stored  $\bar{p}$ . With a high density internal target (target thickness  $\sim 10^{15}$  atoms/cm<sup>2</sup>), the peak luminosity will be  $\sim 10^{31}$  cm<sup>-2</sup>s<sup>-1</sup>. For a design value of  $10^{11}$  stored  $\bar{p}$  with the beam momenta from 1.5 GeV/c to 15 GeV/c the luminosity will be higher by one order of magnitude. In this case the anticipated number of interactions with the target is estimated to be about  $10^7$  s<sup>-1</sup>.

Two complementary operating modes of HESR are planned which are named a high luminosity and a high resolution mode, respectively. The high luminosity mode with  $\Delta p/p = 10^{-4}$ , stochastic cooling and the target thickness of  $4 \times 10^{15}$  cm<sup>-2</sup> will provide an average luminosity of up to  $L = 1.6 \times 10^{32}$  cm<sup>-2</sup>s<sup>-1</sup>.

In the high resolution mode, a lower beam momentum spread  $\Delta p/p = 5 \times 10^{-5}$  will be achieved with electron cooling for momenta up to  $p = 8.9$  GeV/c. This operation will be mainly used in the conjunction with a cluster jet target which will not impose a time structure onto the event rate. The cycle-averaged luminosity is expected to be

$$L = 1.6 \times 10^{31} \text{ cm}^{-2}\text{s}^{-1}.$$

As an example, the luminosity profile for several cycles is shown in Fig. 2.3. In the beam preparation target-off regime, the precooled  $\bar{p}$  are injected to HESR and accelerated/decelerated depending on the request by the experimental program's beam energy. The luminosity drop down occurs mostly due to the multiple scattering off the internal target atoms. A transverse and longitudinal cooling will be used to compensate an increase of betatron oscillations (which result in transverse beam blow up) and to achieve a low momentum spread, respectively. While stochastic cooling will be applicable over the whole momentum range, an electron cooling is foreseen in the range from 1.5 GeV/c to 8.9 GeV/c with a possible upgrade to 15 GeV/c.

### 2.2 The targets

The installation of various targets is foreseen in the  $\bar{\text{P}}\text{ANDA}$  detector. In order to reach the design luminosity of  $2 \times 10^{32}$  cm<sup>-2</sup>s<sup>-1</sup> at  $10^{11}$  stored  $\bar{p}$  in the HESR the hydrogen target thickness must be  $4 \times 10^{15}$  atoms per cm<sup>2</sup>. Both, a Cluster-Jet Target (CJT) and a Pellet Target (PT) are being prepared. The CJT is foreseen for the startup period. The CJT provides hydrogen clusters smaller than 10 mm. The hydrogen density can be adjusted along with the reducing the number of circulating  $\bar{p}$  which allows one to take data at a constant luminosity. The latter is an important practical advantage of this technique.

The PT produces a stream of frozen hydrogen micro-spheres (pellets) traversing the beam perpendicularly. A pellet size of 25  $\mu\text{m}$  at a pellet rate of 25 kHz and a fall speed of 80 m/s imply that the necessary target thickness will be reached.

One technical challenge lies in keeping the whole target line under high vacuum over the distance of 2.1 m between the injection nozzle and the interaction point, plus the same distance until the target particles are dumped in an efficient catcher.

The CJT is homogeneous in space and time whereas a pellet target with an average inter-pellet spacing of 3 mm exhibits large density variations on the 10-100  $\mu\text{s}$  timescale.

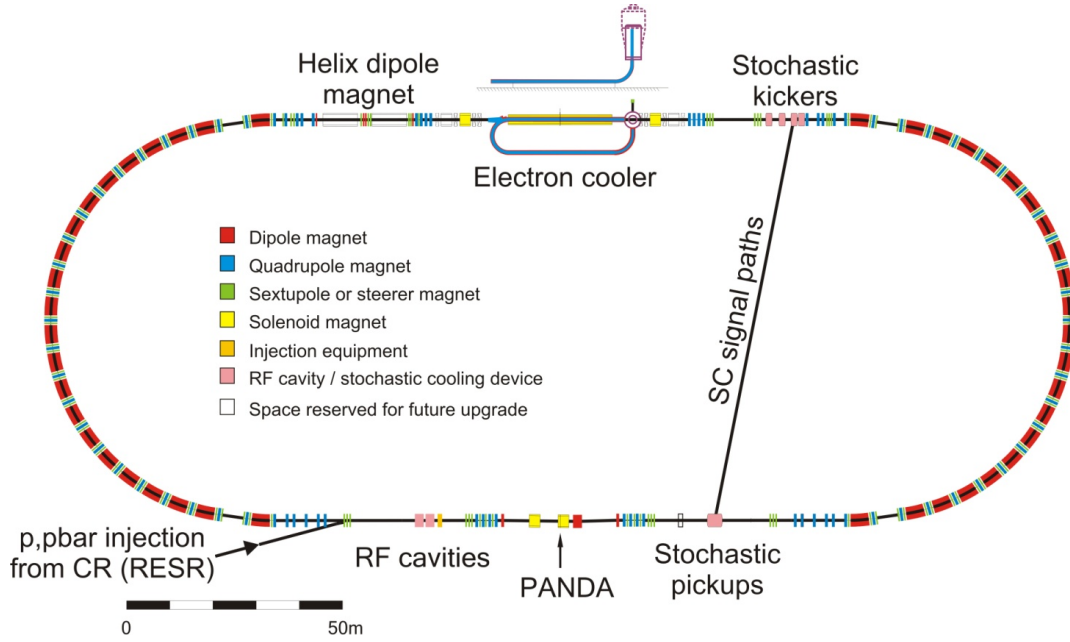


**Figure 2.2:** Layout of HESR. The beam injected from the left into the lower straight section. The total lattice circumference is 575 m. The circulating beam deflection of the spectrometer dipole magnet of the PANDA detector is compensated

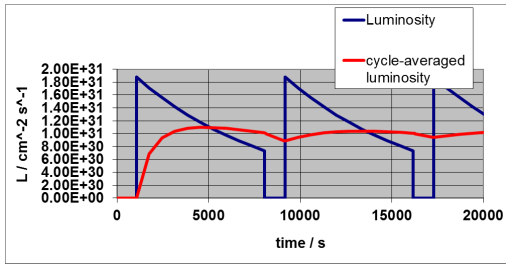


**Figure 2.3:** Time dependent macroscopic luminosity profile for several operation cycles with constant target density (blue curve). Red curve shows cycle-averaged luminosity

An extension of the targets to heavier gases such as deuterium, nitrogen, or argon is possible.

## 2.3 The Detector

Fig. 2.4 shows the detector viewed with partial cut-outs. As a fixed target experiment, the PANDA detector consists of two parts: the Target Spectrometer (TS) and the Forward Spectrometer (FS). The  $\bar{p}$  beam is scattered off a cluster-jet or pellet target. Exclusive measurements of  $\bar{p}p$  reactions requires simultaneous measurements of hadrons, leptons and photons with

the high multiplicities (up to 10 - 12 particles per event).

The physics requirements for the detectors are:

- Practically  $4\pi$  acceptance with high detection efficiency
- Event rate capability of  $2 \times 10^7 \text{ s}^{-1}$
- Momentum resolution not worse than 0.01
- High precision track reconstruction system
- Good event start time reconstruction
- Reliable particle identification ( $\gamma$ ,  $e$ ,  $\mu$ ,  $\pi$ ,  $K$ ,  $p$ )
- Wide range of photon detection (1 MeV - 10 GeV)

## 2.4 Target Spectrometer

The TS, which is almost hermetically sealed to avoid solid angle gaps and with a compact inner volume, consists of a solenoid magnet with a field of 2 T and a set of detectors for the energy determination of neutral and charged particles as well as for the tracking and PID for charged tracks

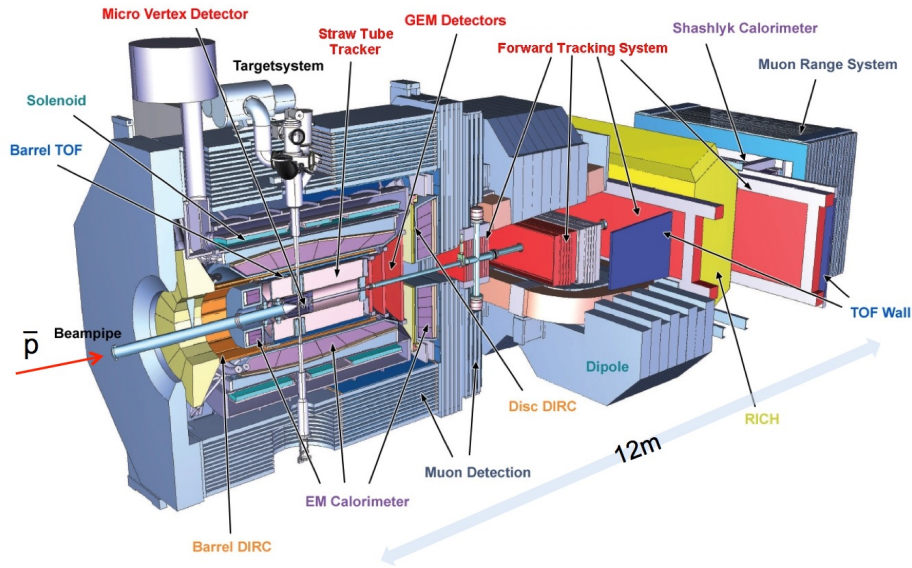


**Figure 2.4:** Side view of with the Target Spectrometer (TS) on the left side, and the Forward Spectrometer (FS) starting with the dipole magnet center on the right. The  $\bar{p}$  beam enters from the left

housed within the superconducting solenoid magnet.

The silicon Micro-Vertex Detector (MVD) surrounds closely the beam pipe in the target area, providing secondary vertex sensitivity for particles with the decay lengths of the order of  $100 \mu\text{m}$ . The main tracker is a straw tube tracker (STT).

There will be several Gas Electron Multiplier (GEM) tracking stations in the forward direction. The tracking detectors MVD and STT also provide information on the specific energy loss in their data stream.

Two Internally Reflected Cherenkov light (DIRC) detectors are to be located within the TS. Compared to other types of Ring Imaging Cherenkov (RICH) counters the possibility of using thin radiators and placing the readout elements outside the acceptance favors the use of DIRC designs as Cherenkov imaging detectors for PID. The Barrel DIRC covers the polar angles  $\theta$  from  $22^\circ$  to  $140^\circ$  inside the TS. The Disc DIRC covers the polar angles  $\theta$  from  $10^\circ$  to  $22^\circ$  in the horizontal plane and  $5^\circ$  to  $22^\circ$  in the vertical plane. For the analysis of the DIRC data the tracking information is needed, as the Cherenkov angle is measured between the Cherenkov photon direction and the momentum vector of the radiating particle.

The Scintillation Tile (SciTil) Hodoscope, or Barrel Time-of-Flight (BToF), serves as precise ( $< 100 \text{ ps}$ ) timing detector cylindrically surrounding

the target. It consists of small scintillator tiles read out by Silicon Photo-Multipliers (SiPMs) and is attached to the support frame outside the Barrel DIRC providing reasonable  $\pi/K$  separation below  $1 \text{ GeV}/c$ . This sub-detector is providing timing information on the picosecond level. The interplay between BToF detector and the FToF wall (which is the topic of this report) is considered in details in this document.

The lead tungstate (PWO) crystals of the electromagnetic calorimeter (EMC) are read out with Avalanche Photo Diodes (APD) or vacuum pentodes. Both, the light output and the APD performance improve with lower temperature. Thus, the plan is to operate the EMC detectors at  $T = -25^\circ \text{C}$ . The EMC is composed of the backward end-cap, the barrel part and the forward end-cap, all housed within the solenoid magnet return yoke.

Besides the detection of photons, the EMC is also the most powerful detector for the identification of electrons.

The return yoke for the solenoid magnet in the TS is laminated to accommodate layers of drift tubes for muon detection. They form a range stack, with the inner muon layer being able to detect low energy muons and the cumulated iron layer thickness in front of the outer layers providing enough hadronic material to stop the high energy pions. A similar lamination and instrumentation of the iron is foreseen in the downstream door of the yoke augmented by the addition of the muon

filter located in between the TS and the FS.

## 2.5 Forward Spectrometer

The FS angular acceptance has an ellipsoidal form with a maximum angular acceptance of  $\pm 10^\circ$  horizontally and  $\pm 5^\circ$  vertically w.r.t. the beam direction.

The tracking section of the FS is incorporated before, after and within the large gap of a dipole magnet providing bending power of 2 T·m with a  $B$ -field perpendicular to the forward tracks. The other parts are placed further downstream outside the dipole magnet.

An aerogel RICH detector will be located right behind the dipole magnet followed by the Forward Time-of-Flight wall (FToF) which also covers the detection of slow particles below the Cherenkov light threshold.

The FToF wall will be described in detail in the following sections as the report is dedicated to this detector.

In addition to the FToF wall, the dipole ToF detector was originally conceived. A high level of the magnetic field is a challenge in designing this detector which suggests the use of SiPMs for readout, not tested up to now with large plastic scintillators. Future challenges are the difficult access, the necessity of electronics cooling and the mechanical interference with the forward tracking system. However, the physical motivation for this system is not evident. Monte Carlo simulations show that the count rate of the hadron hits within the dipole ToF detector is very low even at maximum luminosity. Once the physics case of this detector is clearly demonstrated it will be designed and presented in a separate document.

the secondary electron/positron energy is measured by the Shashlyk type electromagnetic calorimeter consisting of 1404 modules of  $55 \times 55 \text{ mm}^2$  cell size covering  $2.97 \times 1.43 \text{ m}^2$ .

Forward emitted muons are detected with the Muon Range System.

The determination of the luminosity is provided by the detector based on four layers of monolithic active pixel sensors close to the beam pipe detecting scattered  $\bar{p}$  under small angles.

## 2.6 Particle identification system

The charged particle identification (PID) will combine the information from the time-of-flight with event start timestamp information, tracking,  $dE/dx$  and energy deposition, and calorimetry information with the output from the Cherenkov detectors. A combined analysis of the TS and FS using kinematic constraints is extremely important. Thus, the information on time-of-flight and  $T_0$  criteria can be applied by analyzing BToF×FToF coincidences probability of about 50%.

## 2.7 Data Acquisition

The data flow and processing is spatially separated into the Front End Electronics (FEE) part located on the actual detector subsystems and the Data Acquisition (DAQ), located off-detector in the counting room.

The FEE comprises the analog electronics, digitization, low level preprocessing and optical data transmission to the DAQ system.

While each sub-detector implements the detector specific FEE systems, the DAQ features a common architecture and hardware for the complete detector.

Operating the  $\bar{\text{P}}\text{ANDA}$  detector at the interaction rates of  $2 \times 10^7$ , typical event sizes of 4 - 20 kB lead to mean data rates of  $\sim 200 \text{ GB/s}$ .

The  $\bar{\text{P}}\text{ANDA}$  DAQ design does not use fixed hardware based triggers but features a continuously sampling system where the various subsystems are synchronized with a precision time stamp distribution system.

The event selection is based on the real-time feature extraction, filtering and high level correlations.

The main elements of the  $\bar{\text{P}}\text{ANDA}$  DAQ are the data concentrators, the compute nodes and high speed interconnecting networks. The data concentrators aggregate data via point-to-point links from the FEE and the compute nodes provide feature extraction, event building and physics driven event selection.

A data rate reduction of about 1000 is envisaged in order to write the event data of interest to permanent storage.

The peak rates above the mean data rate of  $\sim 200$

GB/s and increased pile-up may occur due to  $\bar{p}$  beam time structure, target thickness fluctuations (in case of the pellet target) and luminosity variations during the HESR operation cycle.

Therefore, FPGA based compute nodes serve as the basic building blocks for the  $\bar{P}$ ANDA DAQ system exploiting a parallel and pipelined processing to implement the various real-time tasks, while the multiple high speed interconnects provide a flexible scalability to meet the rate demands.

## 2.8 Infrastructure

The detector is located below the ground in an experimental hall, encased in a smaller tunnel-like concrete structure, partially fixed, partially made of removable blocks. Most subsystems connect their FEE components via cables and tubes (placed in movable cable ducts) to the installations in the counting house, where three levels are foreseen to accommodate cooling, gas supplies, power supplies, electronics, DAQ and work space.

## References

- [1] B. Lorentz, A. Lehrach, R. Maier, D. Prasuhn, H. Stockhorst, and R. Tolle. HESR Linear Lattice Design. *Conf. Proc.*, C0806233:MOPC112, 2008.



## 3 Technical design considerations of the FToF wall

---

### 3.1 General requirements

There is a big variety of photodetectors used in high energy physics experiments for time-of-flight measurements. Some recent reports dedicated to fast and ultra-fast photodetectors developed for modern physics applications can be found in [1, 2, 3, 4, 5, 6, 7, 8, 9, 10, 11, 12].

The time-of-flight detector under consideration (FToF wall) is subject to the following technical requirements:

- The time resolution must be better than 100 ps;
- The FToF wall is positioned at 7.5 m downstream of the target (interaction point);
- The sensitive area of the scintillation wall is 5.6 m width  $\times$  1.4 m height;
- The thickness of plastic scintillators should not exceed 2.5 cm in order not to deteriorate the performance of the forward electromagnetic calorimeter located downstream of the FToF wall;
- The scintillation wall should withstand a high counting rate corresponding to maximal luminosity of the  $\bar{P}$ ANDA experiment;
- The dynamic range of the detector should cover all possible variations of energy deposition in the scintillators;
- The FToF wall must work at nonzero fringe field of the  $\bar{P}$ ANDA dipole magnet (up to 80 G by absolute value);
- The opening in the wall for the vacuum beam pipe must be foreseen.

These requirements can be met easily by a system of commercial scintillators and photodetectors. It seems reasonable that the system will be consisting of individual scintillation counters. The height of a scintillation slab is to be taken equal to a vertical dimension of the required sensitive area, i.e., 140 cm. The granularity is subject to an admitted counting rate load. According to the MC simulations results (Sec. 4), the charge particle count

rate of an individual scintillation counter based on the slab, with width 5 cm in the central part of the wall and 10 cm in both side parts, will not exceed 0.6 MHz. The suggested configuration of the scintillation wall in  $xy$ -plane (perpendicular to the spectrometer axis  $z$ ) is shown in Fig. 3.1. The thickness of all slabs in the wall is 2.5 cm (see Sec. 5). The energy loss of relativistic hadrons passing through the slab is about 5 MeV, with the number of produced photons per MeV being  $10^4$ . Also shown in Fig. 3.1 the opening which serves to pass the beam vacuum pipe through the wall. It is asymmetrically located as the FS dipole deflects the  $\bar{p}$  beam from the spectrometer axis in the horizontal plane by  $2.2^\circ$ , which results in the deviation of 11.1 cm at the wall position. In order to provide this opening (vacuum pipe diameter at FToF position is 180 mm), four slabs in the central part must be cut.

For a large plastic scintillator a precise measurement of particle hit position is crucial for timing resolution: 1 mm uncertainty in hit position along the slab, i.e. along  $y$ -axis in Fig. 3.1, corresponds to 5.9 ps in time (see discussion related to the linear fitting in Fig. 5.26, Sec. 5.2). It is planned that the information on the hit position will be provided by the Forward Tracking System. An expected uncertainty in  $y$  in this case will be on the level of 2-3 mm. Another option is the "mean-timer variant" as described in Sec. 5.2. In this case the hit position uncertainty is ruled out. In practice, both variants might be combined. This, however, is not the case for the four central slabs which must be cut in order the beam pipe could pass through. The hit positions information obtained with the FTS can only be used for those counters.

### 3.2 Plastic scintillators

A set of parameters of plastic scintillators which are typically in use for the particle detection is given in Table 3.1. The best timing parameters (rise time and decay time) displayed in the Table 3.1 belongs to BC-404. On the other hand, the light attenuation length of BC-404 is significantly smaller than that of BC-408. The latter param-

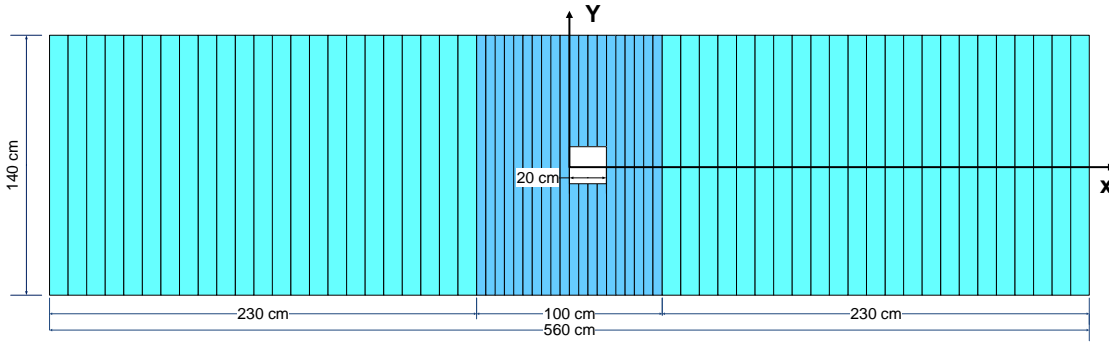


**Figure 3.1:** Configuration of the FToF wall assembled of scintillation slabs: central part (dark blue) consists of 20 scintillation counters, the side parts (light blue) consist of 23 counters each. The width of the slabs is 5 cm (10 cm) in the central (side) part. The opening for the beam vacuum pipe at  $x = 11.1$  cm is indicated

eter is very important for a large acceptance system like the FToF wall under consideration. Since the BC-408 time properties are very close to the best ones listed in Table 3.1, we select this plastic scintillator as the basic material for the FToF wall scintillation counters.

The maximum of BC-408 emission spectrum shown in Fig. 3.2 is 425 nm (blue light) which corresponds well to the maximum of PDE (photon detection efficiency) of most fast photodetectors (photomultiplier tubes or silicon photomultiplier).

### 3.3 Energy depositions and dynamic range

Most of the particles to be detected with the FToF wall are relativistic hadrons, muons and electrons. The smaller the particle momentum, the larger the stopping power and energy loss. Protons with the energy of 50 MeV are stopped in the plastic scintillator of 2.5 cm thickness (Fig. 3.3). This range of 2.5 cm for other (lighter) particles corresponds to smaller energies, e.g., this energy is 5 MeV for electrons. Therefore, for low energy particles, the energy deposition of 50 MeV is a maximum implying that the particle tracks are practically perpendicular to the wall surface. The minimum energy range to explore corresponds to MIP (minimum ionizing particle), i.e. 1.9 MeV  $g^{-1}cm^2$ . Respectively, the minimum energy deposition is 4.83 MeV (for BC-408 with density 1.032  $g/cm^3$ ). Consequently, the expected range of variation of light pulses related to the energy deposition spread (maximum over minimum) is given

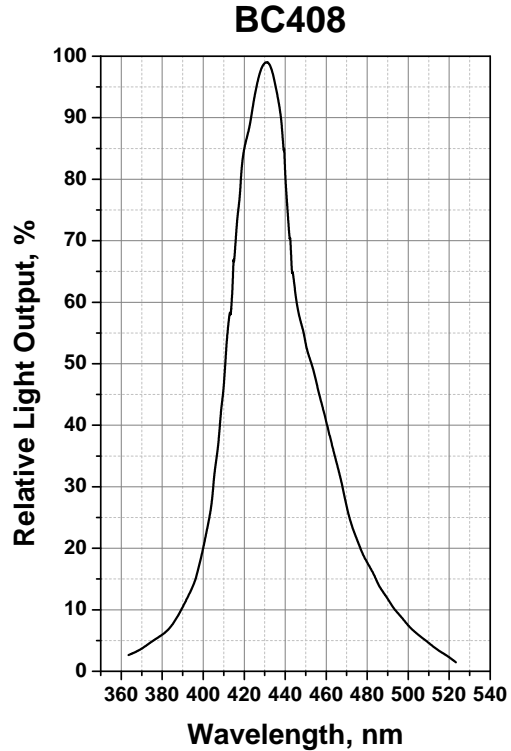


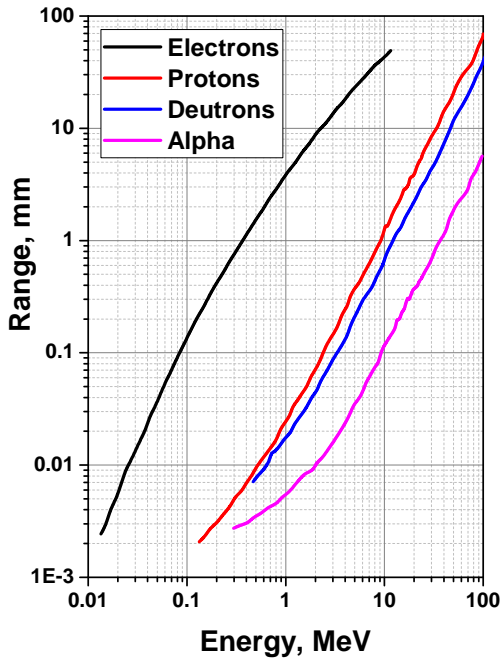
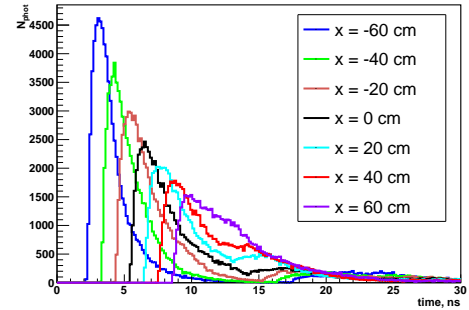
**Figure 3.2:** Emission spectrum of BC-408

by a factor of 10.

Another source of light pulse variations comes from the attenuation of the light propagating along the slab. For the BC-408 narrow slab of 140 cm length this factor is  $e^{\frac{140}{210}} = 1.95$ . A light propagation through the BC-408 under ideal wrapping condition (no photon escapes the plastic volume) has been simulated using the GEANT4 package. The time dependence of light pulses produced by 500 MeV protons traversing a  $10 \times 140 \times 2.5$   $cm^3$

**Table 3.1:** Properties of plastic scintillators produced by BICRON [13]

Properties	BC-400	BC-404	BC-408	BC-412	BC-416
Light output, % anthracene	65	68	64	60	38
Rise time, ns	0.9	0.7	0.9	1.0	-
Decay time, ns	2.4	1.8	2.1	3.3	4.0
Pulse width FWHM, ns	2.7	2.2	2.5	4.2	5.3
Light atten. length, cm	160	140	210	210	210
Wavelength of max. emission, nm	428	408	425	434	434
No. of H-atoms per cm <sup>3</sup> ( $\times 10^{22}$ )	5.23	5.21	5.23	5.23	5.25
No. of C-atoms per cm <sup>3</sup> ( $\times 10^{22}$ )	4.74	4.74	4.74	4.74	4.73
No. of e <sup>-</sup> per cm <sup>3</sup> ( $\times 10^{22}$ )	3.37	3.37	3.37	3.37	3.37
Principal uses/applications	General purpose	Fast counting	Large area ToF	Large area	Large area

**Figure 3.3:** Ranges of charged particles in plastic scintillator**Figure 3.4:** Light pulse shapes detected at one end of the plastic scintillator for various hit positions  $x$ 

slab perpendicular to its surface (i.e. passing

along 2.5 cm slab thickness) are shown in Fig. 3.4. Here  $x$  indicate the hit position along the scintillator,  $x = 0$  being in the middle of the slab. The light pulse is assumed to be detected by a photodetector fastened to the light guide which is glued to one end of the plastic scintillator at  $x = -70$  cm. Concerning timing measurements, the front part of the light pulse is important and one may conclude that the additional variation of the pulse amplitude from one end of the plastic scintillator to the other is given by a factor of 3.

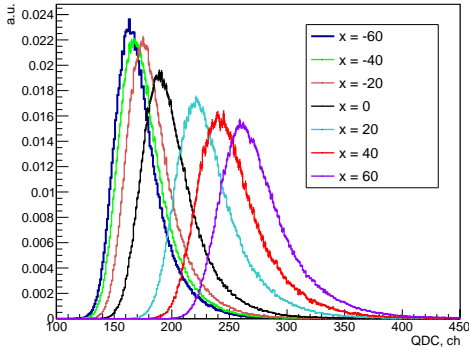


**Figure 3.5:** Amplitude distributions of the light pulses in QDC channels for various positions of the 920 MeV proton hits (Sec. 5). The light was read-out with the PMT R4998 coupled at one end with the  $140 \times 5 \times 2.5 \text{ cm}^3$  BC-408 slab

This result was confirmed experimentally where the integrated light pulses produced in a  $140 \times 5 \times 2.5 \text{ cm}^3$  scintillator exposed with 920 MeV protons has been measured with QDC (Sec. 5). The result is presented in Fig. 3.5.

In conclusion, considering both, the energy deposition spread (a factor of 10) and the light attenuation effect (a factor of 3) in the plastic scintillator the dynamic range of the detected light pulses is given by a factor (max/min) of 30.

## 3.4 Selection of photodetectors

### 3.4.1 Photomultiplier Tubes

The PhotoMultiplier Tubes (PMTs) are widely used and very well studied photodetectors. Most of the information on PMTs considered below is presented in the Hamamatsu handbook [14]. The time response parameters of a PMT are mainly determined by the dynode structure and a number of stages. The best candidates are linear-focused PMTs with the rise time in the range of 0.7 to 3 ns. The ultra-fast microchannel plate (MCP) PMTs with rise time 0.1-0.3 ns are too expensive, as well as mesh-type PMTs. The latter can operate in a magnetic field up to 0.6 T [15] which is not required in our case. In Table 3.2, the characteristics of conventional linear-focused and fine-mesh PMTs are compared. The time response is mainly determined by the electron transition time (ETT). For the time resolution, the most important char-

acteristics are the rise time and transition time spread (TTS). The TTS is defined as the timing uncertainty of the anode signal arrival for a single electron hitting the photocathode.

It is important to remember that all the time characteristics ( $\tau$ ) are improved by an increase of the applied voltage  $V$ . Since the kinetic energy of electrons accelerated in a PMT is proportional to the applied voltage for their relative change one may use an approximate formula:  $\frac{\delta\tau}{\tau} \simeq -\frac{1}{2} \frac{\delta V}{V}$ .

As it has been mentioned above the main feature of the mesh PMTs is that their high performance is guaranteed in a rather strong magnetic field while the time resolution is about the same as that for linear focusing PMTs. The price, however, is typically 3 to 4 times higher. The conventional PMTs are sensitive even to a moderate magnetic field and thus must be properly protected.

The dipole induced magnetic field at the FToF wall position does not exceed 80 G by an absolute value [16]. In the horizontal plane ( $y = 0$ ), it is maximal at the spectrometer axis ( $x = y = 0$ ,  $z = 7.5 \text{ m}$ ) and drops to 30 G at  $x = 3 \text{ m}$ . The  $B_y$  component at  $x = y = 0$  drops down to 22 G at the wall position ( $z = 7.5 \text{ m}$ ) as shown in Table 3.3.

The behavior of the conventional and fine-mesh PMTs in a moderate (below 0.5 T) magnetic field was investigated in [15]. The magnetic field affects the gain of a PMT depressing the output anode signal. This results in an increase of the time walk when using a standard readout electronic scheme with leading edge discriminators and thus worsens the timing resolution. The effect of a magnetic field on the PMT response depends on many factors like PMT position with respect to the magnetic field vector, its dimensions, number and type of stages, etc. A common solution is to use a composite shielding consisting of a thin  $\mu$ -metal envelope as the inner shield and an outer iron cylinder. The  $\mu$ -metal shielding is arranged such that to protrude over the PMT surface by about the tube diameter. As has been shown in [17] the conventional PMT R4998 operates satisfactorily for longitudinal magnetic field (along the PMT axis) up to  $B_z \simeq 60 \text{ G}$  and transverse field  $B_\perp \simeq 150 \text{ G}$  using only a 1 mm thick  $\mu$ -metal shield. With a composite shielding the transverse field had no effect up to 600 G. Various variants of composite shielding are considered in details in [15].

As the  $B_z$  component of the stray field at the FToF wall position stays well below the admitted value stated above and the transverse component

**Table 3.2:** Characteristics of conventional linear-focused and fine-mesh PMTs

	R4998	R9800	R2083	R5505	R7761	R5924
PMT type	linear-focused	linear-focused	linear-focused	fine-mesh	fine-mesh	fine-mesh
Tube diameter	1"	1"	2"	1"	1.5"	2"
No. stages	10	8	8	15	19	19
Q.E. at peak	0.2	0.25	0.2	0.23	0.23	0.22
Gain ( $\times 10^6$ )	5.7	1.0	2.5	0.5	10.	10.
$e^-$ transit time, ns	10	11	16	5.6	7.5	9.5
Rise Time, ns	0.7	1.0	0.7	1.5	2.1	2.5
TTS, ns	0.16	0.27	0.37	0.35	0.35	0.44
HV <sub>max</sub> , V	2500	1500	3500	2300	2300	2300

**Table 3.3:** Change of  $B_y$  component along spectrometer  $z$  axis

$z$ , m	6.9	7.0	7.1	7.2	7.3	7.4	7.5
$B_y$ , G	101	76	58	45	35	28	22

$B_{\perp}$  does not exceed 100 G, a simple shielding with a 1 mm  $\mu$ -metal shielding (see above) is sufficient. The PMT with the  $\mu$ -metal shield is to be placed in a iron cylinder of a few mm thickness. As far as cost consideration is an issue, the sort of iron and housing thickness must be chosen according to the experimentally obtained information on the dipole stray field at the FToF wall position.

It must be noted that while the fine-mesh PMTs can operate in a rather high longitudinal magnetic field ( $B_z \simeq 0.6$  T), however, they are very sensitive to the transverse component, i.e., it is required that the axis of a PMT must be aligned along the field direction.

### 3.4.2 Silicon Photomultipliers

A big advantage of the silicon photomultipliers (SiPMs) is their insensitivity to the magnetic field. No sensitivity to the magnetic field as high as 4 T has been experimentally observed as reported in [18]. An example of time characteristics for a single electron case is shown in Fig. 3.6. The quantum efficiency of SiPMs is typically around 80%, while for the PMT it is not higher than some 40%. There are some other merits of the SiPMs like compactness, low operation voltage, relatively low cost, etc. On the other hand the radiation

hardness and aging effects are still subject to experimenting. The studies at the PNPI test station of several samples of KETEK 6660 SiPM showed good time characteristics, just a little worse than those for the fast PMTs (Sec. 5). SiPMs are used in high energy physics experiments with the scintillators of moderate sizes [19]. In the case of large scintillation walls, the conventional PMTs are traditionally used. The reason is mostly due to the relatively small active area of the SiPMs. While the active area of a KETEK 6660 SiPM is  $0.6 \text{ cm} \times 0.6 \text{ cm} = 0.36 \text{ cm}^2$  the active area covered with a 1" (2") PMT is larger, by a factor of 50 (200). This fact cannot be compensated by the higher quantum efficiency of the SiPMs. The use of many SiPMs might appear as a possible design choice but it would complicate the electronic readout scheme and the calibrations. Yet the advantages of SiPMs certainly motivate further technical developments aimed at SiPM applications also for a large scintillator readout.

## 3.5 Readout electronics

As described in Sec. 5, the experimental study of prototypes of the FToF scintillation counter has been performed with the help of fast electronics modules available in the PNPI. In the  $\overline{\text{P}}\text{ANDA}$  experiment, it is planned to use a compact FPGA based platform, such as TRB-3 with PADIWA FEE interfaces developed in GSI. The TRB platform is a multi-purpose Trigger and Readout Board with an on-board DAQ functionality developed for the HADES experiment upgrade [20, 21, 22]. This compact multi-functional

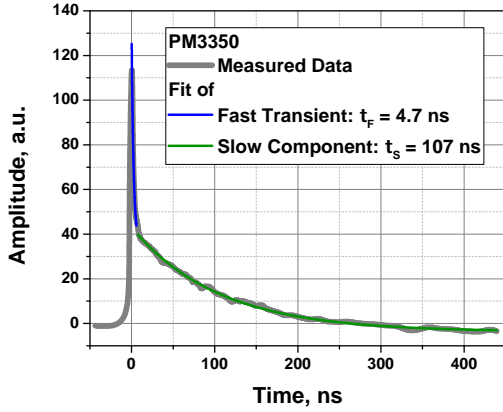


**Figure 3.6:** Single photoelectron pulse shape for KETEK PM 3350 SiPM

FPGA based readout board is assumed to be widely used in PANDA and CBM experiments at FAIR.

The TRB-3 and two examples of the PADIWA modules are shown in Fig. 3.7 and Fig. 3.8, respectively. The TRB-3 readout board contains 264 individual high timing resolution (8 ps) TDC channels for LVDS signals. Table 3.4 lists basic features of the TRB3 platform.

The PADIWA module - a 16 channel discriminator - produces LVDS signals both by the front and trailing edge of a PMT analog signal provided the height of the PMT pulse exceeds a fixed PADIWA threshold. The LVDS signals are sent to a TRB which provides a Time-Over-Threshold information.

The time resolution of the PADIWA and TRB-3 based electronics was measured using a fast generator. Fig. 3.9 shows the time difference histogram measured with signals 50 mV/10 ps from the generator. The time resolution of 30 ps is practically insensitive to an increase of the pulse amplitude (by a factor of 2). The resolution gets somewhat worse (35 ps) if the pulse amplitude was reduced by 50%.

The FPGA temperature of the tested TRB-3 was controlled. It was first cooled to 21 °C with the help of fans, and then ventilation was stopped. After 40 min without ventilation the FPGA temperature increased to 29.5 °C without any noticeable effect on the time resolution.

Electronics tests are based on the Time-over-threshold (TOT) method which has recently become very popular [23][24]. The PADIWA LVDS signals define the signal time-stamp-start and its

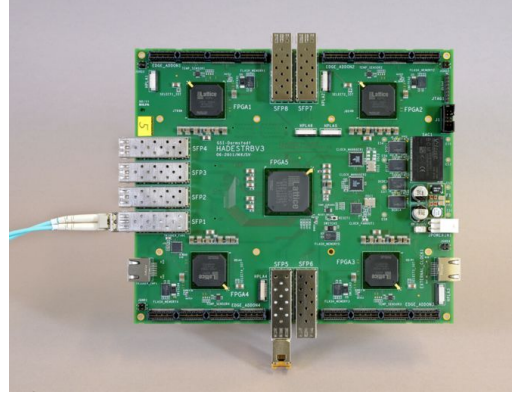


**Figure 3.7:** TRB-3. Functionality is described in text

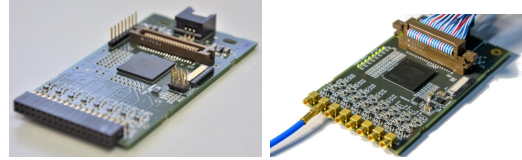


**Figure 3.8:** PADIWA3 (left) and PADIWA-AMPS2 (right). Functionality is described in text

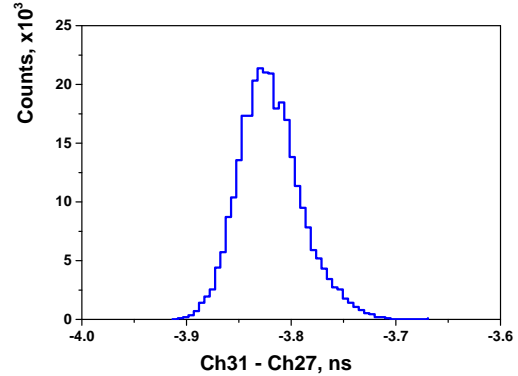


**Figure 3.9:** TDC time resolution of  $\sigma \sim 30$  ps has been measured

width  $\tau$ . As the pulse amplitude (or integrated charge over threshold) is proportional to  $\tau$ , one may use it for the amplitude correction for the time walk. One should remember, however, that this method has a limited dynamic range and linearity. Thus, the method must be very well adjusted to the particular experiment requirements.

Measurements of the TRB-3 platform with photodetectors were carried out in the PNPI. The measurements were performed at the PNPI test station with two KETEK SiPMs coupled face to

**Table 3.4:** Some basic features of the TRB3 platform

Item	Value
Supply Voltage	48 V (40-50V), galvanically isolated on board
Power Supply Current	0.5A minimum without additional electronic boards
GbE-connectivity	max. 95 MBytes/s transfer per link
GbE-slow-control	up to 400 registers/transfer, speed depends on GbE latency
Connectivity	Max. 8 SFPs, each 2Gbit/s on board. With hub add-on: max. 32 SFP 4 AddONs on top (208 pin), 1 AddOn on bottom
Max Readout Trigger Rate	about 300 KHz (depending on configuration and network size)
Max Hit Rate	50 MHz (burst of 63 hits)
TDC Channels	260 (Single edge detection)
Time Precision	< 20 ps
Minimum pulse width	< 500 ps

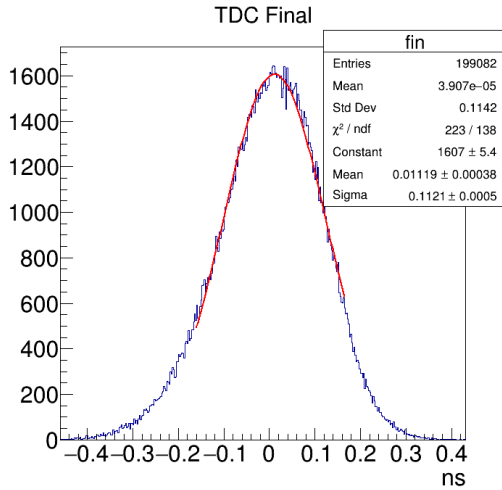


**Figure 3.10:** Time resolution curve obtained at the PNPI test station with two KETEK SiPMs after TOT corrections:  $\sigma = 112$  ps. Raw result (without correction) was twice worse (220 ps).

face to a small  $6 \times 6 \times 9$  mm<sup>3</sup> plastic scintillator. The plastic scintillator was irradiated with a collimated radioactive <sup>90</sup>Sr source (as described in detail in Sec. 5). The resulting time resolution spectrum is shown in Fig. 3.10.

Very recently, tests of the PADIWA3+TRB-3 readout electronics has been repeated at the PNPI test station in configuration presented in Fig. 5.1 (Sec. 5.1.2) where PMT0 and PMT1 were both Hamamatsu R4998. The contribution from electronics to the timing resolution was again controlled using a fast generator. It was found to be  $\sigma = 20$  ps. In this measurement the radioactive source was not collimated which increased the time walk due to uncertainty in track position in the scintillator to some 28 ps. Raw timing resolu-

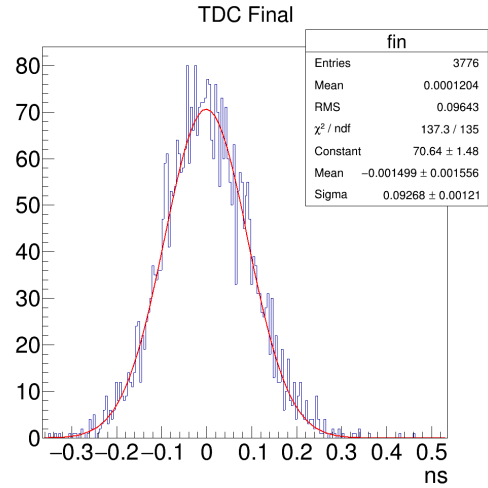


**Figure 3.11:** Time difference between PMT0 and PMT1 corrected by TOT.

tion of  $\sigma = 130$  ps was obtained. After amplitude correction using TOT method it was reduced to 92 ps (Fig. 3.11). The latter, being corrected for electronics contribution and time walk in the scintillator, corresponds to 50 ps per one PMT which meets the requirement of PANDA experiment.

**Connectivity.** One FToF wall hit corresponds to a 265 bit word containing all the service and data information. The overall count rate of target related particles is expected not to exceed 2-3 MHz. For the central part of the wall, the count rate of individual counters is less than 1 MHz because of the granularity which is twice higher than that in the side parts. The average hit multiplicity is about 1.5. The total FToF wall data flow is estimated to be about 150 MB/s, which would be less than 40 MBytes/s per one TRB-3 if four

TRB-3s are in use.

### 3.6 Mechanics, cabling, integration

Fig. 3.12 and Fig. 3.13 show schematically the front and side views of the FToF wall with a supporting frame. The bearing beams of the frame are made of duralumin HX4080E-8 profile. The wall consists of two halves positioned on a rail from the left and from the right side of the beam pipe. Vertical stability of the system is provided with a rail suspended on the ceiling. In order to move the system into the service position a removable extension to the rails is foreseen.

Fig. 3.14 shows an assembly of two scintillation counters (lower part of the FToF wall) at the border between the central and side parts of the detector. The light guides made of Plexiglas are glued to the scintillators with BC-600 optical cement. The BC-408 is the originally planned material of the scintillation slab. In order to compromise the cost and quality it might be replaced with EJ200, or similar, as presented in Sec. 7. The wrapping is aluminized mylar and black PVC covering. The optical contact between the light-guide and photocathode is provided with silicone elastomers. The active dividers are situated between the connectors and the PMT (not shown in Fig. 3.14). The housings are cylinders with walls of 2 mm thickness made of a magnetic steel (e.g. steel-10). For protection against low level dipole stray field (transverse component) two layers of  $\mu$ -metal shield fully covering both the PMT and a part of the light -guides are applied.

The weight of the FToF detector together with the supporting frame, the wheels and the rail is estimated to be 800 kg, with the plastic scintillators and PMTs with housing being about a half of this value.

The number of readout channels (number of PMT output signals) is 132. In the case of PADIWA3, one needs 9 PADIWA modules. For reliable operation at the picosecond level the cables for PMT analog and LVDS pulses must be short: the analog signal (LVDS) cable should not exceed 50 (200) cm. Proceeding from dimensions of the FToF wall detector, four TRB-3 modules are to be used to collect LVDS signals from the PADIWA3 frontend interfaces. As an example, 10 TRB-3 modules with PADIWA frontends at Juelich test beam were used providing 2400 channels at

10MHz count rate [25]. The PADIWA and TRB-3 modules are assumed to fasten to the frame over and below the sensitive area of the detector.

HV and LV power supply. It is assumed to provide HV power supply for the PMTs using two HV patch panels at the left and right side of the supporting frame. It is planned to use the HV power supply source similar to that worked out by the PNPI Electronic department for the NUSTAR-R3B experiment at FAIR (1000 PMT channels) [26]. The maximal HV of 3500V is needed (for R2083 PMT). It is implied that both R2083 and R4998 PMT will be equipped with active dividers [27]. The scheme of an active divider which has already been tested with the R4998 PMT is presented in Fig. 3.15. Note that the maximum counting rate about 1 MHz is expected for the FToF central part with these PMTs.

The LV power supply: one module for four TRB-3 (+48V,  $4 \times 0.5A$ ) and four units for PADIWA-2 (+5V,  $18 \times 0.3A$ ) will also be positioned at the frame.

### 3.7 Safety regulation

The design details and construction of the FToF wall detector will be performed according to the safety requirements of FAIR and the European and German safety regulations. In the FToF wall case, a potential source of danger is a high voltage power supply (HV). The maximum possible high voltage value (negative) is 3500V. In order to ensure the protection of all personnel against hazardous voltage supplies, HV-lines, patch panels and connectors the several well seen overall markings will be made. All the HV and LV power supply sources will be properly grounded. Two different regimes, subjects to the safety rules, are foreseen for HV on and off variants and the panel with the corresponding announcements - "High Voltage On" or "High Voltage off" - will be functioning. All cabling and connections will be used according to up-to-date standards.

### 3.8 Summary

The main task of the FToF wall is to detect on event basis the timestamps of particles hits in one or more scintillation blocks. Time resolution must be better than 100 ps. The  $\bar{P}$ ANDA experiment operates in a triggerless mode and a dedicated start counter is not foreseen. Thus, the PID analysis

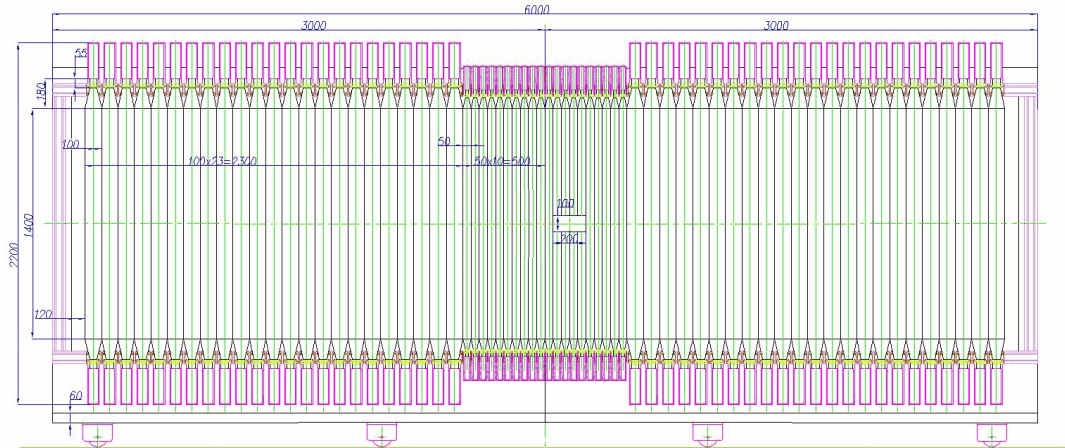


**Figure 3.12:** Schematic view of the FToF wall with the supporting frame placed on a rail.

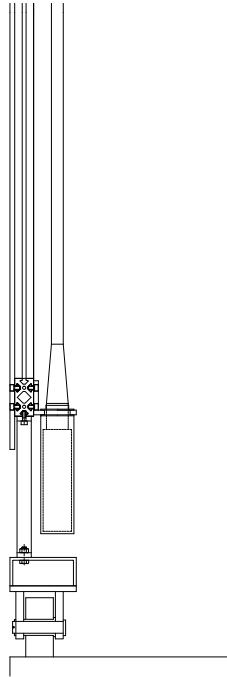


**Figure 3.13:** Side view of the FToF wall (cross section).

per event should mostly be done offline by analyzing the whole set of the information obtained by all other  $\bar{P}$ ANDA sub-detectors. In particular, an interplay with other timing detectors, like the SciTil, is important. In simple cases, however, like elastic  $\bar{p}$  scattering or  $\bar{\Lambda} \rightarrow \bar{p}\pi^+$  decay, only measurements of charge particle momenta are needed for the unambiguous identification. The latter must be widely used for an event start determination and detector calibration.

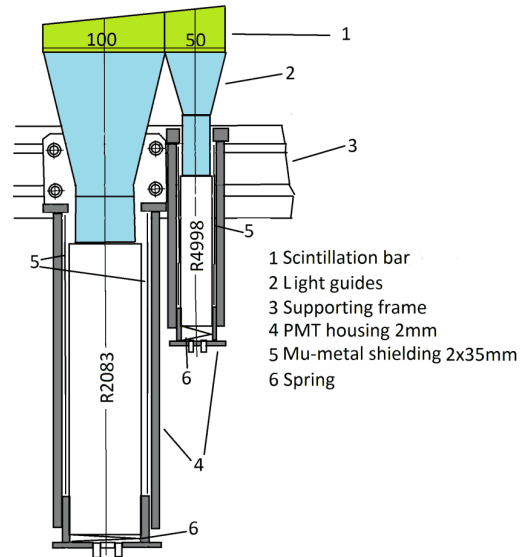


**Figure 3.14:** The assembly of two PMTs in the border between central and side parts of the FToF wall. Mu-metal covers PMT beyond front face (see text).

To summarize, it is proposed to build the FToF wall made of BC-408 plastic scintillator (or equivalent EJ200, see comment to Sec. 7.5) forming the active area of the wall as shown in Fig. 3.1. Each scintillation counter consists of a scintillation slab and two fast PMTs situated at the each end of the slab. In the central part of the wall the slabs with dimensions 5 cm (width)  $\times$  140 cm (height)  $\times$  2.5 cm (thickness) are viewed through the light guides with 1" PMTs. The number of counters in the central part is 20. The side parts with the slabs of 10 cm width are equipped with the 2"

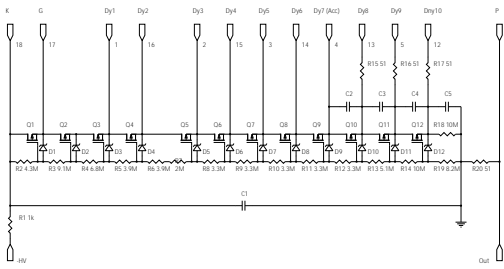


**Figure 3.15:** Scheme of active divider tested with Hamamatsu R4998 PMT

PMTs with appropriate light guides. The number of counters in each side part is 23. All PMTs are vertically positioned such that all their axes are parallel to the  $y$ -axis of the PANDA detector. The calculated value of the  $B_y$  component of the magnet dipole stray field does not exceed 20 - 30 G while the transverse component is less than 100 G. This allows one to arrange magnetic field shielding with the help of a 1 mm thick  $\mu$ -metal (inner shield). The cylindrical iron housing of 2 mm thickness serves as outer shielding.

A time resolution at the level of 200 - 250 ps can be obtained online. A better time resolution (of 60 - 80 ps) would be reached in the offline analysis by applying amplitude and hit position corrections to raw time distributions. In the test and prototyping period, conventional readout electronics consisting of leading edge-discriminators LEDs, time-digital-converters TDCs and amplitude (charge)-digital converters ADC (QDC) have been used. The electronics resolution is usually dominated by the TDC resolution which must not be worse than 25 ps. In the PANDA experiment it is planned to implement the readout electronics TRB3, the FPGA-based TDC modules developed in GSI [28].

## References

- [1] Jean-Francois Genat, Gary Varner, Fukun Tang, and Henry J. Frisch. Signal Processing for Pico-second Resolution Timing Measurements. *Nucl. Instrum. Meth.*, A607:387–393, 2009.
- [2] Luc Bonnet, Junhui Liao, and Krzysztof Piotrkowski. Study on GASToF A 10 ps resolution timing detector. *Nucl. Instrum. Meth.*, A762:77–84, 2014.
- [3] I. Deppner et al. The CBM Time-of-Flight wall - a conceptual design. *JINST*, 9(10):C10014, 2014.
- [4] Arno Knapitsch, Etienne Auffray, Christian W. Fabjan, Jean-Louis Leclercq, Xavier Letartre, Radoslaw Mazurczyk, and Paul Lecoq. Effects of Photonic Crystals on the Light Output of Heavy Inorganic Scintillators. *IEEE Trans. Nucl. Sci.*, 60(3):2322–2329, 2013.
- [5] R. X. Yang et al. MRPC detector for the BESIII E-ToF upgrade. *JINST*, 9(09):C09032, 2014.
- [6] Robert J. Abrams, Charles M. Ankenbrandt, Gene Flanagan, Steven Kahn, M. Notani, and Henry J. Frisch. Applications of Fast Time-of-Flight System. *Phys. Procedia*, 37:650–658, 2012.
- [7] N. Harnew. TORCH: A Large-Area Detector for Precision Time-of-Flight Measurements at LHCb. *Phys. Procedia*, 37:626–633, 2012.
- [8] Y. Arita. Verification of Focusing System for Time-of-Propagation Counter. *Phys. Procedia*, 37:621–625, 2012.
- [9] T. Kajimoto et al. Measurements and parameterization of neutron energy spectra from targets bombarded with 120 GeV protons. *Nucl. Instrum. Meth.*, B337:68–77, 2014.
- [10] P. Moskal et al. Test of a single module of the J-PET scanner based on plastic scintillators. *Nucl. Instrum. Meth.*, A764:317–321, 2014.
- [11] R. Jeffrey Wilkes. Time synchronization improvements in the T2K long-baseline neutrino experiment. *PoS*, Neutel2013:083, 2013.
- [12] M. Bonesini, R. Bertoni, A. de Bari, and M. Rossella. Construction of a Fast Diode-Laser based Calibration System for Time-of-Flight Systems. *PoS*, EPS-HEP2013:004, 2013.
- [13] Bicron specifications “bc-400/bc-404/bc-408/bc-412/bc-412”. [http://www.phys.ufl.edu/courses/phy4803L/group\\_I/muon/bicron\\_bc400-416.pdf](http://www.phys.ufl.edu/courses/phy4803L/group_I/muon/bicron_bc400-416.pdf).
- [14] Hamamatsu Photonics K.K. Photomultiplier tubes: Basics and applications, edition 3a, 2007.
- [15] M. Bonesini, R. Bertoni, A. de Bari, and Rossella. M. Behaviour in Magnetic Fields of Fast Conventional and Fine-Mesh Photomultipliers. *Nucl. Instrum. Meth.*, A693:130–137, 2012.

- [16] PANDA collaboration. Technical progress report for panda, 2014.
- [17] R. Bertoni et al. The design and commissioning of the MICE upstream time-of-flight system. *Nucl. Instrum. Meth.*, A615:14–26, 2010.
- [18] E. Garutti, M. Groll, A. Karakash, and S. Reiche. Magnetic field dependence studies for silicon photomultiplier. 2004.
- [19] Paolo W. Cattaneo, Matteo De Gerone, Flavio Gatti, Miki Nishimura, Wataru Ootani, Massimo Rossella, and Yusuke Uchiyama. Development of High Precision Timing Counter Based on Plastic Scintillator with SiPM Readout. *IEEE Trans. Nucl. Sci.*, 61(5):2657–2666, 2014.
- [20] I. Fröhlich et al. TRB for HADES and FAIR experiments at GSI. In *Astroparticle, particle and space physics, detectors and medical physics applications. Proceedings, 10th Conference, ICATPP 2007, Como, Italy, October 8-12, 2007*, pages 973–977, 2008.
- [21] A. Gil, D. Belver, P. Cabanelas, E. Castro, J. Diaz, J. A. Garzon, D. Gonzalez-Diaz, W. Koenig, and M. Traxler. Front-end electronics of the HADES RPC wall: Full sector test. In *Proceedings, 2008 IEEE Nuclear Science Symposium, Medical Imaging Conference and 16th International Workshop on Room-Temperature Semiconductor X-Ray and Gamma-Ray Detectors (NSS/MIC 2008 / RTSD 2008)*, pages 1561–1563, 2008.
- [22] C. Ugur, S. Linev, J. Michel, T. Schweitzer, and M. Traxler. A novel approach for pulse width measurements with a high precision (8 ps RMS) TDC in an FPGA. *JINST*, 11(01):C01046, 2016.
- [23] T. Orita, K. Shimazoe, and H. Takahashi. The dynamic time-over-threshold method for multi-channel {APD} based gamma-ray detectors. *Nuclear Instruments and Methods in Physics Research Section A: Accelerators, Spectrometers, Detectors and Associated Equipment*, 775:154 – 161, 2015.
- [24] I. Kipnis et al. A time-over-threshold machine: The readout integrated circuit for the BaBar silicon vertex tracker. *IEEE Trans. Nucl. Sci.*, 44:289–297, 1997.
- [25] A Neiser, J Adamczewski-Musch, M Hoek, W Koenig, G Korcyl, S Linev, L Maier, J Michel, M Palka, M Penschuck, M Traxler, C Ugur, and A Zink. Trb3: a 264 channel high precision tdc platform and its applications. *Journal of Instrumentation*, 8(12):C12043, 2013.
- [26] Hvds3200, the distributed high voltage system for neuland spectrometer. [http://hepd.pnpi.spb.ru/hepd/events/abstract/2015/20151103\\_HVDS3200.pdf](http://hepd.pnpi.spb.ru/hepd/events/abstract/2015/20151103_HVDS3200.pdf).
- [27] V. A. Kalinnikov. Low powered transistor divider for PMT. 2005.
- [28] Michael Traxler, Wolfgang Koenig, Jan Michel, Marek Palka, and Cahit Uğur. Fpga-based tdc: Trb3 and applications, 2013.



## 4 Physics case of FToF, MC study

### 4.1 Forward spectrometer time-of-flight PID

The Forward Spectrometer (FS) is dedicated to detect particles emitted under the laboratory angles below  $5^\circ$  and  $10^\circ$  in the vertical and horizontal directions, respectively. Although these angles do not seem to be large, a substantial fraction of the particles produced at the target by the beam occurs within this FS acceptance. Generally, the hadrons related to the target proton (or target nucleus) fragmentation are predominantly emitted within the TS while those fragmenting from the beam antiproton are strongly peaked forward in the laboratory frame and thus detected in the FS. All elastically scattered  $\bar{p}$ , as well as most of the produced anti-baryons, are moving forward at very small laboratory angles. This is also true for the anti-hyperon decay product. Thus, as the PandaROOT MC shows, decay products of a inclusive  $\bar{\Lambda}$  production ( $\bar{p} + p \rightarrow \bar{\Lambda} + X, \bar{\Lambda} \rightarrow \bar{p} + \pi^+$ ) are detected with the FToF wall with a high geometrical efficiency of about 20%. Note that for a hyperon produced in  $\bar{p}p$  collision the laboratory polar angle is always kinematically limited. Take as an example the binary production  $\bar{p} + p \rightarrow \bar{\Lambda}_c + \Lambda_c$  at  $p_{beam} = 15$  GeV, the  $\theta_{Lab}^{lim}$  being equal to  $5.58^\circ$ . Most of  $\bar{\Lambda}_c$  hyperons are expected to be produced at the angles below  $\theta_{Lab}^{lim}$  because of the reaction dynamics which implies a small transverse momentum of the produced hyperons. The strange  $\bar{\Lambda}$  from the  $\bar{\Lambda}_c \rightarrow \bar{\Lambda} + \pi^-$  is then detected with a high probability with the FS thus resulting in low background contamination.

Hadron identification is realized in the FS with the help of the FToF wall and forward RICH detectors. While the forward RICH provides effective hadron separation for the momenta above 2 GeV for pions and above 4 GeV for protons (here speed of light  $c = 1$ ), [1] the FToF detector could provide hadron ID at particle momenta below 4 GeV.

The time-of-flights between the target (Interaction Point, IP) and the scintillation wall positioned at 7.5 m downstream of the IP for pions, kaons, protons and charged leptons are shown in Fig. 4.1. The values of ToF ranges from 53.1 ns for proton momentum of 0.5 GeV to 25 ns for relativistic particles.

Besides the forward low momentum hadrons PID, an important function of the FToF wall is that it provides information on the event time stamp in a scintillation block. For a relativistic particle (for a hadron with momenta larger than 3-4 GeV) this information helps to reconstruct the event start time in the IP with a precision of a few ns (Fig. 4.1). Provided the particle is identified either as a hadron or a charged lepton (muon or electron), this precision could be improved to some 100 ps which is the planned time resolution of the FToF detector.

The FToF capabilities for hadron identification of the FS were simulated with the help of "Toy Monte Carlo" assuming that

1. the FToF wall detector is located at 7.5 m downstream of the PANDA spectrometer target;
2. hadrons are uniformly distributed in the selected momentum range from 0 to 5 GeV;
3. all hadron momentum distributions are normalized identically;
4. the momentum resolution of the FS spectrometer is  $\Delta p/p = 0.01$  (Gaussian distribution function);
5. the calculation is performed for ToF resolution  $\sigma_{ToF}$  (Gaussian distribution function) for 50, 100, 150 and 200 ps.

The particle mass is reconstructed using the following equation ( $c=1$ ):

$$m = p \sqrt{\frac{t^2}{t_c^2} - 1} \quad (4.1)$$

Here  $p$  is the particle momentum,  $t_c = L/c$ ,  $L$  is the length of the particle track starting from the IP (start point), or from a decay vertex, to the hit position in a FToF counter,  $c$  is the speed of light,  $t$  is the measured time of flight, i.e.,  $t/t_c = 1/v$ , where  $v$  is the particle velocity. The fractional uncertainty of the calculated mass can be estimated as

$$\frac{\delta m}{m} = \sqrt{\left(\frac{\delta p}{p}\right)^2 + \gamma^4 \left(\frac{\sigma_{ToF}}{t}\right)^2} \quad (4.2)$$

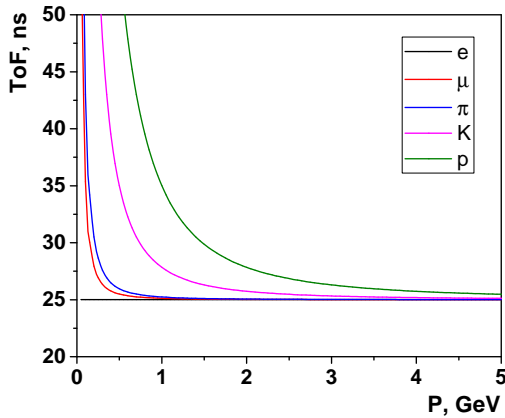


**Figure 4.1:** Time-of-flight of hadrons, muons and electrons between the target (IP) and the FToF wall detector positioned at 7.5 m downstream of the target versus particle momentum

where  $\gamma = 1/\sqrt{1-v^2}$ . Due to the relativistic  $\gamma$  factor, the time-of-flight resolution of 50 (or 100) ps gives the main contribution to the mass smearing for the particles with momenta  $p \geq 1$  GeV, while the momentum resolution of 1% has a much smaller effect. However, at  $p < 1$  GeV the momentum uncertainty becomes more important. The uncertainty in  $t_c$ , which comes from the track reconstruction in the magnetic field of the TS solenoid and the FS dipole, must also be taken into account. Here we assume that the contribution of this uncertainty is much smaller than that of  $\sigma_{ToF}$  in Eq.(4.2). Note that size of this contribution is still under question. It needs a MC study with FS tracking included. An uncertainty of FS track reconstruction at the level of  $\delta L/L \approx 0.001$  translates to  $\delta\sigma_{ToF}$  of about 25 ps for relativistic particles.

Results of the calculation for the hadron mass reconstruction (Eq.(4.1)) using a simplified model above (Toy MC) is presented in Fig. 4.2. Based on this approach, separation power functions showing capability to distinguish between various hadrons can be built, as displayed in Fig. 4.3.

Separation power for hadrons  $h_i, h_k, i, k = \pi, K, p$  have been calculated as  $|t_i - t_k|/(\sigma_i + \sigma_k)/2$ , where  $t_i$  and  $t_k$  is time-of-flight of hadrons  $h_i$  and  $h_k$ , respectively,  $\sigma_i$  and  $\sigma_k$  has been found by fit to probability density functions in Fig. 4.2 at given hadron momenta.

In a more realistic manner, hadron reconstructed mass distributions have been obtained in the frame of PANDAROOT MonteCarlo with tracking through the dipole magnet reproduced with

GEANT4, Fig. 4.4.

As it can be seen, the time-of-flight information obtained with the help of the FToF wall provides a reliable  $\pi$  and kaon identification up to the secondary particle momentum of 2.5 GeV at  $\sigma_{ToF} = 100$  ps (up to 3.5 GeV for simulations with  $\sigma_{ToF} = 50$  ps) and proton (antiproton) identification up to 4 GeV for  $\sigma_{ToF} = 100$  ps (up to 5.3 GeV for  $\sigma_{ToF} = 50$  ps). Note that at momenta smaller than 0.5 GeV the proton time-of-flight increases very sharply with a momentum decrease which results in worsening the mass reconstruction at very small momenta.

Construction of a dedicated start counter in the interaction point area is technically not feasible and not foreseen for the PANDA detector. The time-of-flight information is assumed to be obtained using the time correlations per interaction in the PANDA detector by the responses between two or more scintillation counters of the FToF wall and/or Barrel ToF detectors. The time of flight is extracted offline in combination with other criteria similar to the HADES experiment at GSI. The efficiency of such a procedure will depend on the multiplicity of particles produced in the reaction under investigation, the event topology and the background situation. As PANDAROOT Monte Carlo (MC) shows the efficiency is high for many benchmark reactions. A positive feature of this approach is that the overall time resolution in this case is improved with an increase of  $n$ , where  $n \geq 2$  is the number of counters with a hit.

To conclude, hadrons with the momentum range of 2 – 4 GeV will be identified by combining the information from the FToF and the forward RICH detectors. Over the whole momentum range, the FToF wall is used to establish the event start timestamp which is very important for the PANDA trigger-less data taking procedure.

It must be noted that a good timing resolution-per event is obtained in the offline analysis making use of the timing and amplitude information for each photomultiplier and the hit position information in the scintillation slab. The precision of the hit position measurement in vertical ( $y$ ) direction along the slab must be at the level of 1 mm, which corresponds roughly to 5 ps timing uncertainty. A tracking system satisfying this requirement in the FS is mandatory needed for obtaining the timing resolution of the order of 50 – 100 ps.

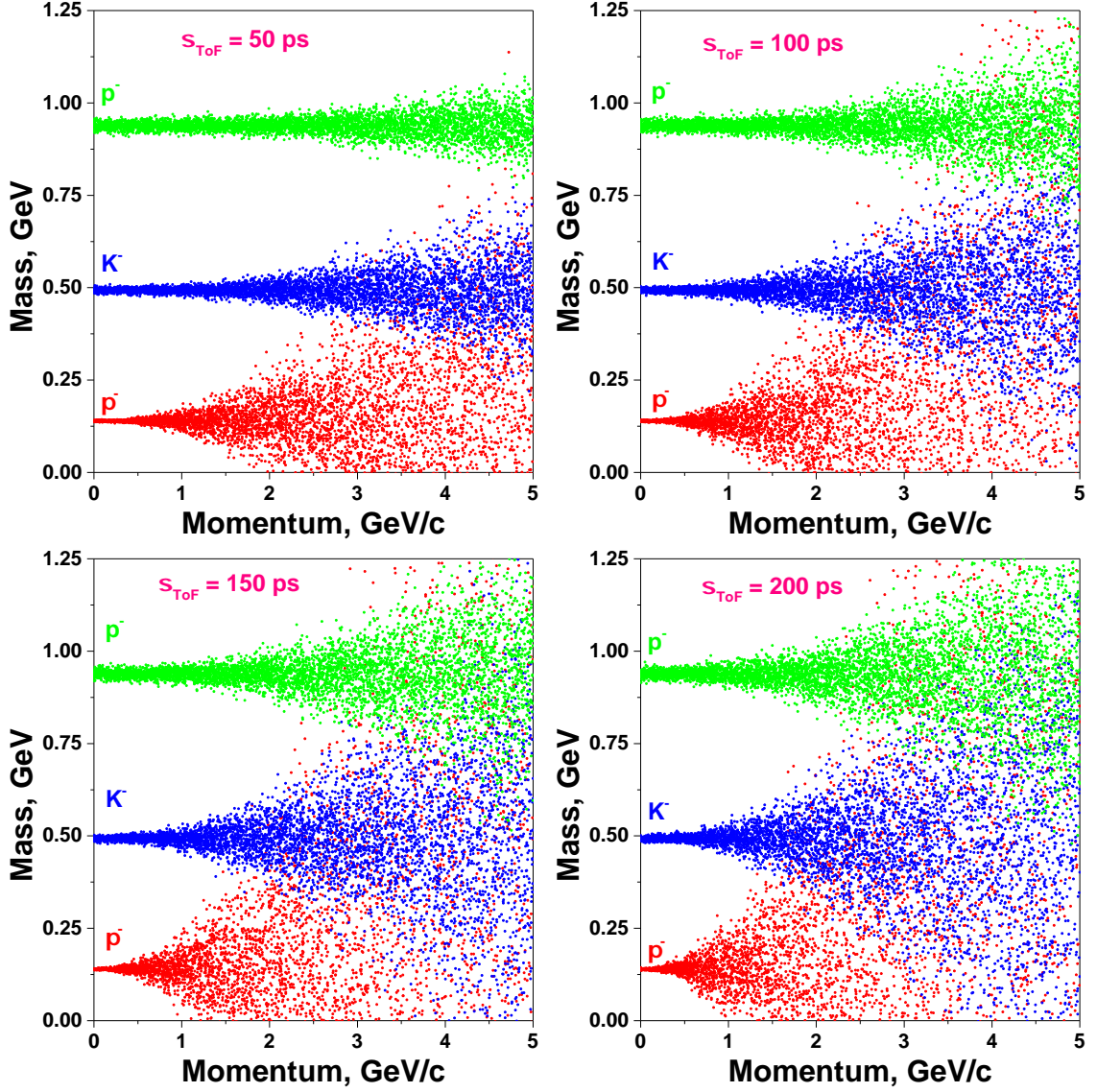


**Figure 4.2:** Hadron mass reconstruction using Toy Monte Carlo (probability density functions). Highly populated areas correspond approximately  $\pm 2.5\sigma$  deviation in reconstructed mass smearing

## 4.2 Count rate and background estimations

Some preliminary MC studies were done using PYTHIA6. However, the applicability of the PYTHIA package at the relatively low energy is questionable. Therefore, the performance of the FToF detectors was mostly investigated in the framework of the PANDAROOT MC with the Dual Parton Model (DPM) generator [2] applied for hadron production on the hydrogen target and the antiproton beam momentum in the range from 2 to 15 GeV.

The DPM generator produces a number of final states. The typical ones produced at 10 GeV antiproton beam are:  $\bar{p}p \rightarrow \bar{p}p$ ,  $\bar{p}p \rightarrow \bar{p}p\pi^0$ ,  $\bar{p}p \rightarrow \bar{n}n\pi^0$ ,  $\bar{p}p \rightarrow \bar{n}p\pi^0\pi^-$ ,  $\bar{p}p \rightarrow \bar{p}p\pi^+\pi^-$ ,  $\bar{p}p \rightarrow \bar{p}n\pi^+\pi^0$ ,  $\bar{p}p \rightarrow \bar{p}p\pi^+\pi^-\pi^0$ ,  $\bar{p}p \rightarrow \bar{n}p\pi^+\pi^-\pi^0$ ,  $\bar{p}p \rightarrow \bar{p}p\pi^+\pi^+\pi^-\pi^0$ ,  $\bar{p}p \rightarrow \bar{\Lambda}nK_L\pi^+\pi^-\pi^0$ , ... and many other states.

As one can see, the counting rate of both target and forward spectrometers is expected to be dominated by the hadrons. The integrated yield of reactions with meson production is approximately equal to that for elastic antiproton proton scattering. The latter is strongly peaked forward. It is important to note that the relative frequency

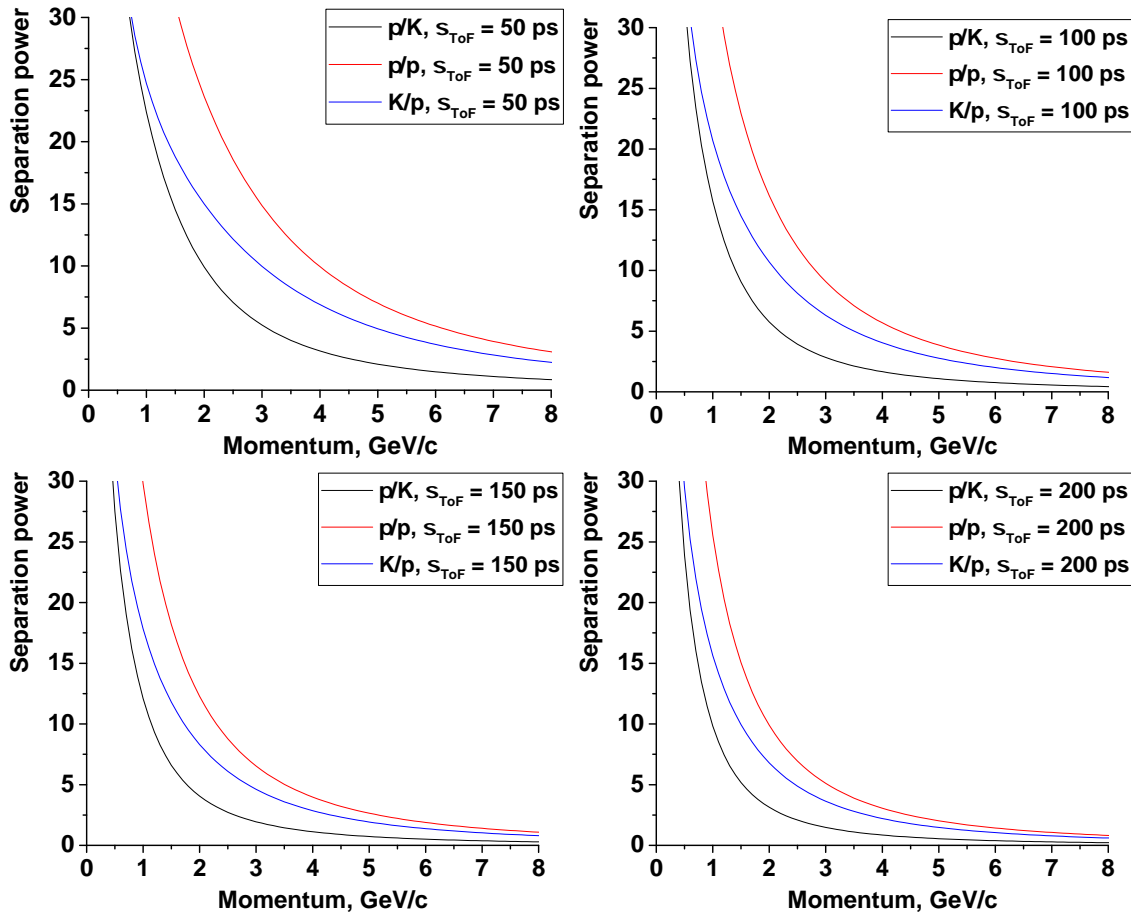


Figure 4.3: Separation power for various variants of time resolution.

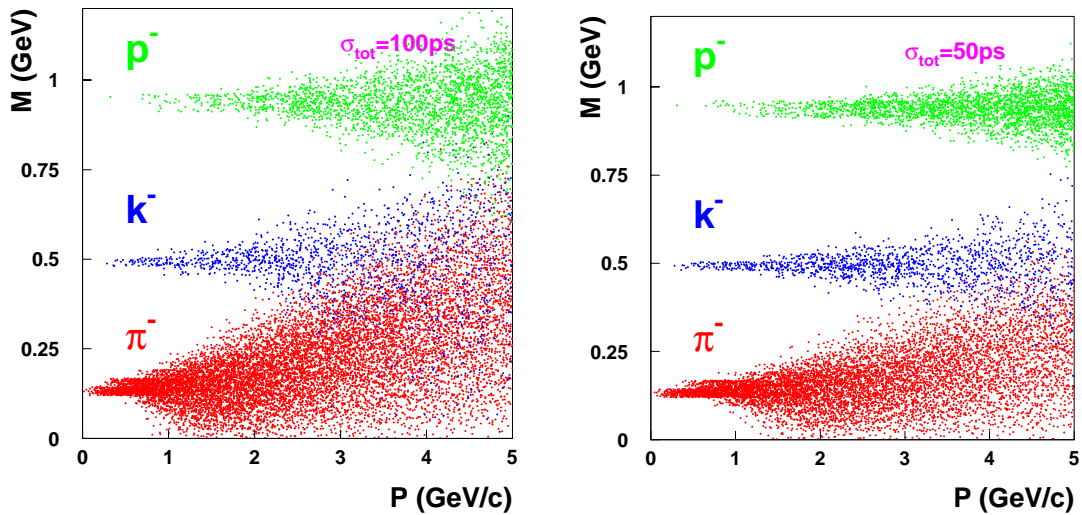
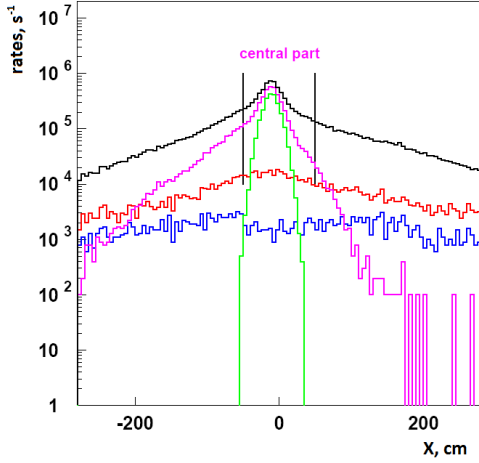


Figure 4.4: Hadron masses reconstructed using the time-of-flight information with the ToF resolution of  $\sigma = 100$  ps (left panel) and  $\sigma = 50$  ps (right panel). Highly populated areas correspond approximately  $\pm 2.5\sigma$  deviation in reconstructed mass smearing

**Table 4.1:** Integrated rates of hadrons within the acceptance of the FS at the HESR cycle-averaged luminosity  $L = 10^{32} \text{ cm}^{-2}\text{s}^{-1}$

$p_{\text{beam}}$ , GeV	2	5	15
$\pi$ rate, 1/s	$3.9 \times 10^5$	$6 \times 10^5$	$9.6 \times 10^5$
$K$ rate, 1/s	$2 \times 10^3$	$7.8 \times 10^3$	$4.7 \times 10^4$
Proton rate, 1/s	$1.2 \times 10^4$	$3.8 \times 10^4$	$3.2 \times 10^4$
$\bar{p}$ rate, 1/s	$1.1 \times 10^6$	$9.5 \times 10^5$	$8.2 \times 10^5$



**Figure 4.5:** FToF wall rates versus X axis perpendicular to the beam line at 15 GeV  $\bar{p}$  beam (PYTHIA6). The rates are normalized to  $10^7$  interactions in the target. The black curve is the total rate of all charged particles emitted from the target, the purple curve is the rate of  $\bar{p}$  both from elastic  $\bar{p}p$  scattering and inelastic reactions, the green curve shows  $\bar{p}$  from elastic scattering only, the red curve is all charged particles produced in the beam vacuum pipe, and the blue curve corresponds to  $e^+e^-$ -pairs produced in the beam vacuum pipe by  $\gamma$ -photons emitted from the target as products of the  $\pi^0 \rightarrow 2\gamma$  decay. The rates are calculated in bins equal to 10 cm (the slab widths in the side parts of the wall), both for the central and side parts

of  $\pi^0$  production is high which may result in a substantial  $e^+e^-$  background:  $e^+e^-$ -pairs are presumably produced in the spectrometer materials (e.g., in the walls of the beam vacuum pipe) by the  $\gamma$ -quanta from  $\pi^0$  decaying in the target.

The geometry of the FToF wall detector implemented in the MC-geometry file is shown in

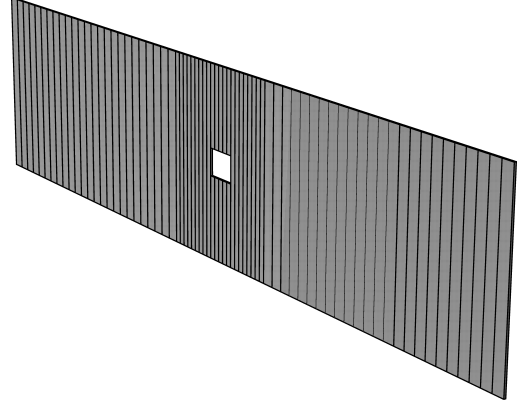


**Figure 4.6:** Schematic views of Forward ToF wall as implemented in PANDAROOT

Fig. 4.6. In the MC calculations, simple “box approximations” were used for the FToF wall scintillation counters, i.e., the counter is assumed to be fired provided that the particle track occurs within its sensitive volume.

The integrated rates of hadrons emitted within the FS acceptance are presented in Table 4.1 (PYTHIA6). The main contribution to the total rate in the  $\bar{p}$  beam momentum range under study is related to a sharp forward peak of  $\bar{p}p$  elastic scattering. As a source of background, this peak can be essentially suppressed by kinematical criteria. Other hadron count rates are found to be substantially lower.

The rates of individual slabs in the FToF wall related to various processes versus  $x$ , the axis perpendicular to the beam line in the horizontal plane, are shown in Fig. 4.5. These estimations had been performed using PYTHIA6. The rates are calculated in bins equal to the slab widths in the side parts of the wall, i.e., 10 cm for both, the central and side parts. Remember that the central part slab width is half wide (5 cm) and, therefore, their count rates, shown in Fig. 4.5, must be reduced by a factor of 2. One can conclude that even in the central part of the FToF wall the total rates are below the limit admitted by the technical characteristics of the fast scintillation counters.

The procedure of MC simulation in the PANDAROOT framework was as follows. The generated events were propagated through the  $\bar{P}$ ANDA detector model implemented in the PANDAROOT package based on the GEANT4 simulation tool. Both, the solenoid and dipole magnetic fields were included. The Barrel ToF (SciTil) was described in the geometry file in a simplified form as a

**Table 4.2:** Count rates of  $\bar{\text{PANDA}}$  time-of-flight detectors using PANDAROOT. The numbers obtained for 80000 generated events have been scaled to  $10^7$  interactions in the target of  $\bar{\text{PANDA}}$  spectrometer (scale factor = 125). Here efficiency is fraction of generated hadrons (with scale factor 125) detected with the detector, N is corresponding count rate

	Generated by DPM 80K events	Detected by BToF		Detected by DToF		Detected by FToF	
		eff	N, $\times 10^6 \text{s}^{-1}$	eff	N, $\times 10^6 \text{s}^{-1}$	eff	N, $\times 10^6 \text{s}^{-1}$
$\pi^-$	90693	0.36	4.08	0.01	0.14	0.23	2.59
$\pi^+$	90725	0.44	5.03	0.002	0.03	0.18	2.07
$K^-$	3022	0.09	0.03	0.001	0.0004	0.26	0.1
$K^+$	3082	0.25	0.09	0.003	0.001	0.12	0.04
$\bar{p}$	42095	0.007	0.04	0.0002	0.001	0.62	3.24
$p$	42003	0.61	3.19	0.002	0.012	0.07	0.35

cylindrical surface sensitive to charged particle hits with 100% detection efficiency which mimicked the sensitive layers of the real SciTil detectors. The FToF wall was implemented as discussed above. Since the electron/positron background seems to be important for the FToF wall, the materials of the beam vacuum pipe and forward EM calorimeter, as these can serve as secondary targets for  $e^+e^-$ -pair production, it has also been included.

The results of these calculations are shown in Table 4.2 where the hadron rates are specified for each time-of-flight detector. The count rates obtained in PANDAROOT are slightly larger than those for PYTHIA6. The average overall rate per scintillation slab of 10 cm width (side parts of the detector) is about  $1.5 \times 10^5 \text{ s}^{-1}$ . In the central part the rate per slab (5 cm width) is  $6.3 \times 10^5 \text{ s}^{-1}$  well below the admitted limit of a few MHz.

As mentioned above, the background rate related to  $\gamma$ -conversion to  $e^+e^-$ -pairs must be taken into account. The  $e^+e^-$ -pairs are produced on the ‘‘secondary targets’’, i.e., on  $\bar{\text{PANDA}}$  detector elements such as the beam pipe, FSTT or RICH materials, magnet coils, etc. The forward EM calorimeter located very close downstream of the FToF wall can also load the FToF wall slabs with  $e^+$  or  $e^-$  scattered backwardly.

The results of computations of the hadron count rates versus  $x$ , the position on the  $x$  axis, in comparison with that of electron (positron) background are presented in Fig. 4.7. The rate histograms are calculated in 5 cm bins. The numbers presented in Fig. 4.7 correspond to luminos-

ity  $2 \times 10^{32} \text{ cm}^{-2} \text{ s}^{-1}$  ( $10^7$  interactions). The black histogram shows the contribution from all hadrons (62%), the magenta area shows elastic scattering, the blue histogram demonstrates the total contribution from  $e^+$  or  $e^-$  (29%), the red histogram and dashed blue correspond to contribution of  $e^+e^-$ -pairs produced in the beam vacuum pipe and  $e^+$  or  $e^-$  scattered backwardly from the EM calorimeter, respectively.

It is important to notice that the momentum distributions related to pair productions are strongly peaked at small momenta and typically end up below 2 GeV as demonstrated in Fig. 4.8 and in Fig. 4.9. In this energy range the maximum energy deposit of electrons in the plastic scintillator of 2.5 cm thickness is 10.4 MeV (which corresponds to full absorption in plastic). For hadrons the maximum energy deposit corresponds to protons with energy 50 MeV. A typical energy deposit for relativistic hadrons is close to MIP, i.e., about 5 MeV. This defines the necessary dynamic range of the PMT pulse amplitude to be measured by the FToF electronics.

Two-dimensional plots show hit distributions in the  $xy$ -plane of the FToF wall together with their projections on the  $x$  and  $y$  axes are shown in Fig. 4.10. A small opening in the two-dimensional plots indicates the hole for the beam vacuum pipe.

A double-hit probability in a single bar can be estimated proceeding from the maximum  $\approx 1$  MHz count rate per a bar in the central part of the wall. Assuming a flat in time luminosity distribution and taking 20 ns as a dead time (necessary for the Time Over Threshold measurements [3],

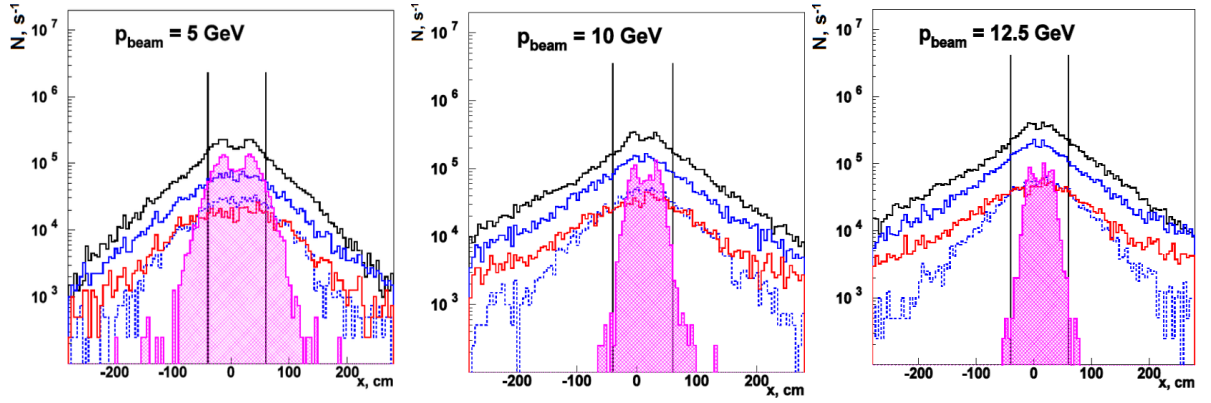


**Figure 4.7:** FToF wall rates versus  $x$  axis perpendicular to the beam line at 5 GeV (left panel), 10 GeV (central panel) and 12.5 GeV (right panel) calculated in the frame of PANDAROOT. Black histogram represents all charged hadrons, magenta area shows elastic  $\bar{p}$  scattering, blue histogram corresponds all  $e^+e^-$ , red histogram shows contribution of  $e^+e^-$ -pairs produced in the beam vacuum pipe, blue dashed histogram is contribution of  $e^+$  or  $e^-$  resulted from backward scattering in the forward EM calorimeter. The rates are calculated in bins equal to 10 cm (the slab widths in the side parts of the wall), both for the central and side parts

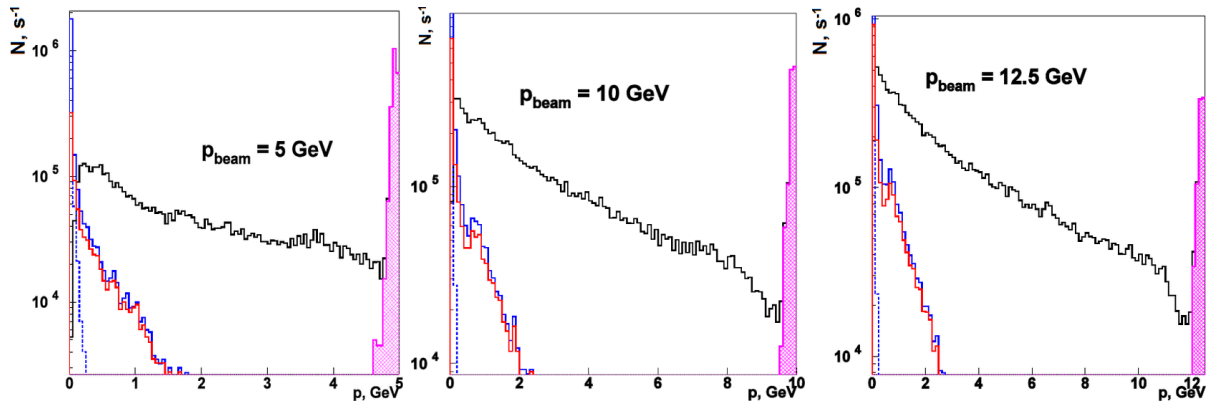


**Figure 4.8:** Momentum distribution of particles detected with forward ToF wall for  $\bar{p}$  beam energy 5 GeV, 10 GeV and 12.5 GeV. Color codes are the same as in Fig. 4.7

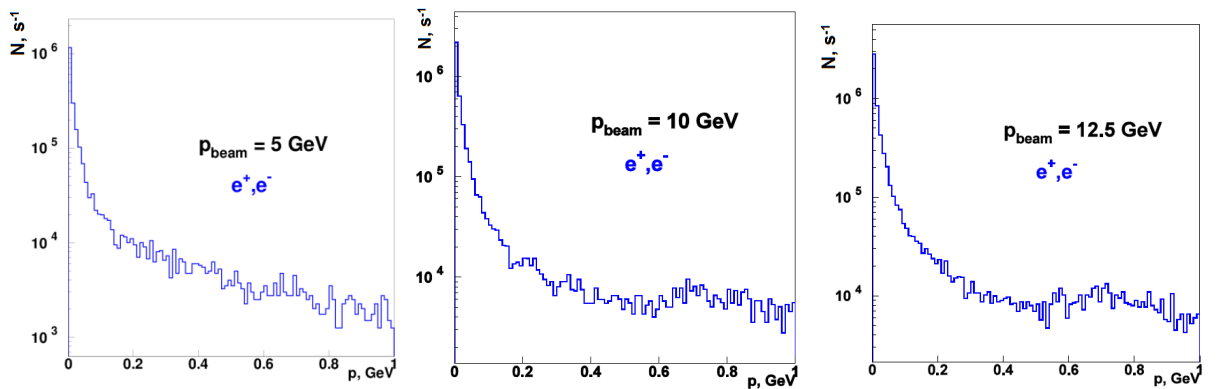


**Figure 4.9:** Momentum distribution of  $e^-(e^+)$  detected with forward ToF wall for  $\bar{p}$  beam energy 5 GeV, 10 GeV and 12.5 GeV in larger scale

**Table 4.3:** Generated and detected with FToF  $\bar{\Lambda}$  and  $\Lambda$  events in inclusive  $\Lambda$ ,  $\bar{\Lambda}$  hyperon production at  $0.72 \times 10^6$   $\bar{p}p$  interactions in the target

	Generated	Detected with FToF wall	Detection efficiency
$\bar{\Lambda}$	19874	3840	0.193
$\Lambda$	19518	100	0.005

[4] pulse duration) one obtains 2%. The probability to hit two adjacent bars can be estimated for hadrons (no secondary showers) proceeding from FS angular acceptance and bar thickness (2.5 cm) and its width (5 or 10 cm). One obtains less than 5% and 2% for the bar width of 5 and 10 cm, respectively. These events are not lost for the analysis as the track information and an energy deposition criterion can be applied.

### 4.3 $\Lambda$ hyperon detection with FToF wall

According to the qualitative arguments given in Sec. 4.1 the forward spectrometer is expected to detect decaying anti-hyperons with a high efficiency. As it is seen from Table 4.3, the efficiency to detect both  $\bar{p}$  and  $\pi^+$  from  $\bar{\Lambda}$  decay in inclusive hyperon production ( $\bar{p}+p \rightarrow \bar{\Lambda}+X$ ,  $\bar{\Lambda} \rightarrow \bar{p}+\pi^+$ ) is about 20%. The detection efficiency of  $\Lambda$ -hyperon is essentially lower. A relatively high  $\bar{\Lambda}$  count rate (more than 3 kHz) at the maximal projected  $\bar{\text{P}}\text{ANDA}$  experiment luminosity ( $2 \times 10^{32} \text{ cm}^{-2}\text{s}^{-1}$  or  $10^7$   $\bar{p}p$  interaction in the target) provides a possibility for tuning and calibration of the detector jointly with other FS detectors (FSTT, RICH, forward EMC).

The MC simulations were performed with the DPM generator at 10 GeV antiproton beam and all possible final states have been taken into account (see Sec. 4.2). The generated momentum and angular distributions in the laboratory frame for  $\Lambda$  and  $\bar{\Lambda}$ -hyperons are presented in Fig. 4.11. As one can see these distributions are very different for  $\Lambda$  and  $\bar{\Lambda}$  confirming the considerations about the target and beam hadronization kinematics. Thus  $\Lambda$  momenta are peaked around 1 GeV while the  $\bar{\Lambda}$  momentum increases reaching the maximum at 7.5 GeV just a little smaller than the beam momentum. The  $\Lambda$  angular distribution is flat practically up to an angular limit of  $50^\circ$ .

Contrary to that,  $\bar{\Lambda}$  polar angles show a strong angular dependence staying below  $2.5^\circ$  and being strongly peaked at very small angles. The  $\bar{\Lambda}$  decay kinematics is such that the decay  $\bar{p}$  is also moving forward with the momentum close to that of the parent  $\bar{\Lambda}$  and both  $\bar{p}$  and  $\pi^+$  having an angular limit with respect to the parent momentum. Due to these kinematical features and production mechanism dynamics the probability to detect the two hadrons ( $\bar{p}$  and  $\pi^+$ ) from  $\bar{\Lambda}$  is expected to be high, as confirmed by the simulations. Also, the above considerations help to understand why the detection efficiency for  $\Lambda$  is so much smaller than that for  $\bar{\Lambda}$ .

In the simulations, all particles produced with DPM were propagated through the  $\bar{\text{P}}\text{ANDA}$  detector model incorporated into the PANDAROOT using the GEANT4 program. Since the forward track reconstruction program had not been yet developed, the information on particle momentum, track length, as well as  $\bar{\Lambda}(\Lambda)$  decay vertex position were taken to be as those obtained with GEANT4. Time-of-flight and time stamp of particle arrival at a slab of the FToF detector were calculated and the time-of-flight was smeared using a Gaussian with  $\sigma = 100$  ps.

All combinations of hadron pairs with opposite charges which were produced in a generated event and produced hits in the FToF detector (crossed the sensitive area of the FToF) were selected. In order to isolate  $\Lambda(\bar{\Lambda})$  peak the invariant mass of two hadrons with opposite charges containing their 4-momenta must be built. The FS tracking system gives a 3-momentum of the hadron. Missing is the hadron mass. If the observed hadrons come from  $\Lambda(\bar{\Lambda})$  decay, the negative (positive) hadron should have the proton mass while the positive (negative) hadron must be a pion. As most of the detected pairs are  $\pi^+\pi^-$ -pairs, this condition, i.e., only assumption on the detected hadron mass (criterion A), strongly suppresses the pion background and  $\bar{\Lambda}$  peak is clearly seen in Fig. 4.12 (left panel). Contrary to that, a similar criterion (A) applied for  $\Lambda$  selection does not result in a peak Fig. 4.12 (right panel). This shows that criterion A is not sufficient in the case of much less intensive  $\Lambda$  production within FS acceptance.

In order to suppress better the background contribution the timing criterion was applied (criterion B). The time-of-flight is calculated for both hadrons in a selected pair using the criteria A hypothesis for hadrons masses, their momenta and track lengths. In the case of the wrongly as-

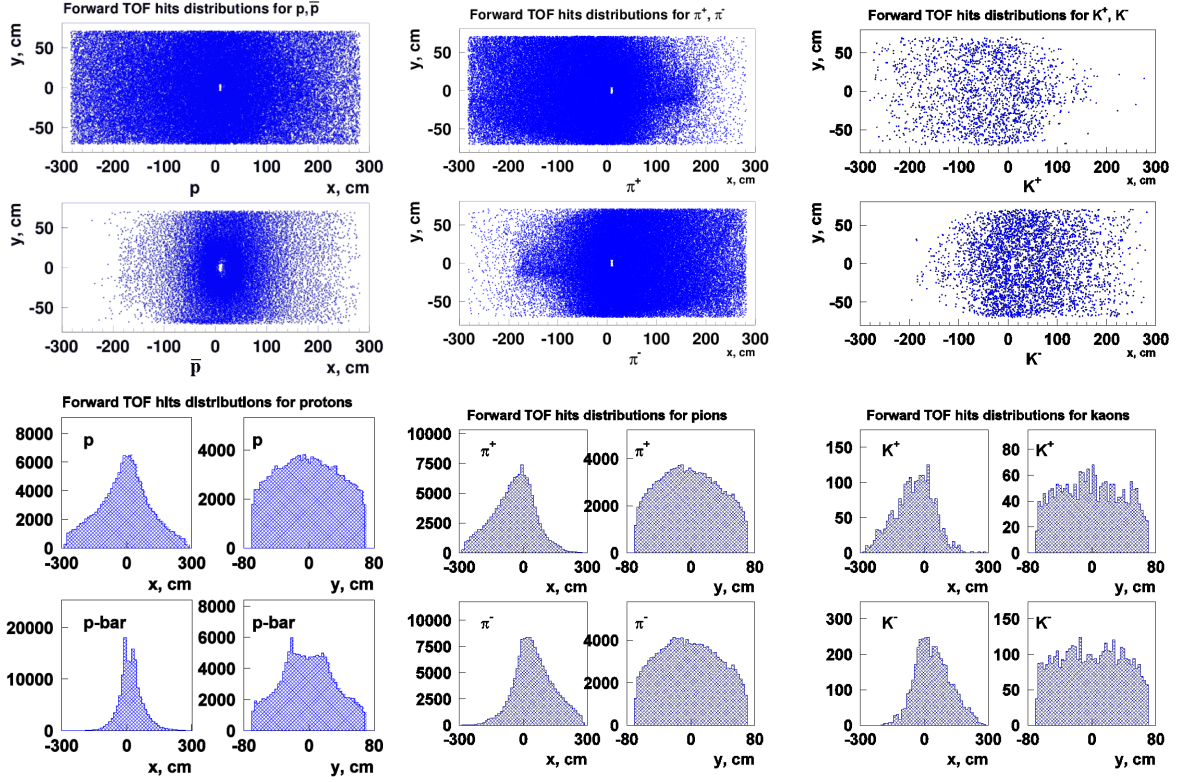


**Figure 4.10:** Hits distributions in the FToF  $xy$ -plane (top) and their  $x, y$ -projections (bottom) for  $p, \bar{p}, \pi^+, \pi^-, K^+$  and  $K^-$

signed mass, e.g. the pion is assumed to have a proton mass, the calculated time-of-flight will be wrong and the timing condition will not be fulfilled. In the real experiment this is equivalent to the PID using the time-of-flight criterion. The timing criterion was quantified by the condition  $|t_{h1} - t_{h2}| < 100$  ps where  $t_{h1}$  and  $t_{h2}$  are time stamps of the hadron 1 and 2 in the decay vertex, respectively. Here we remind that the time resolution in the time-of-flight calculations was taken to be  $\sigma = 100$  ps. As one can see in Fig. 4.13 (left panel) the criterion B resulted in a very strong suppression of the combinatorial background and some decrease of real  $\bar{\Lambda}$  events (due to nonzero  $\sigma$ ). For  $\Lambda$  event selection, the effect of the timing requirement is shown in Fig. 4.13 (right panel). The  $\Lambda$  peak is seen. The number of events in the peak is estimated with the background interpolated with a straight line.

In Fig. 4.14 the  $\bar{\Lambda}$  decay length distribution is shown. The further strong background suppression can be made by a cut on the decay length, or vertex separation  $z_2 - z_1$ . The above example on reconstruction of a weak signal from  $\Lambda$  decay may be instructive in the case of even weaker signals

**Table 4.4:** Probability of coincidences between FToF wall and ScTil detectors

$p_{\text{beam}}$	2.5 GeV	5.0 GeV	10.0 GeV	12.5 GeV
$\epsilon$	23.6%	31.5%	45.4%	48.3%

of decaying particle like, e.g.,  $\bar{\Lambda}_c \rightarrow \bar{\Lambda} + \pi^-$ ,  $\bar{\Lambda} \rightarrow \bar{p} + \pi^+$ . The secondary vertex position is reconstructed with the help of PANDA tracking detectors like the MVD with a high precision. The effect on background suppression due to the vertex separation is expected to be very helpful.

## 4.4 Interplay between FToF wall and SciTil detectors

There is no dedicated start counter in the PANDA detector. In order to use the time-of-flight criterion for the pattern recognition, the timing condition for the time stamps of the particle coming from the IP, or from the decay vertex, must be ap-

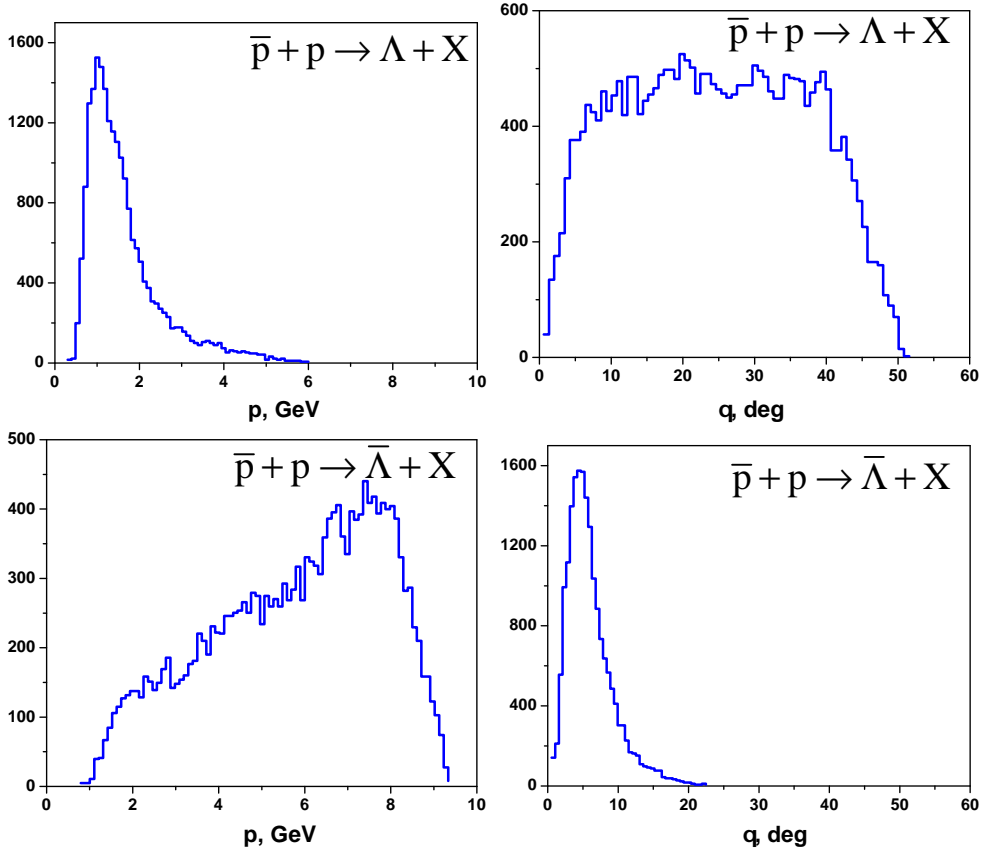


**Figure 4.11:** Momentum and angular distributions for  $\Lambda$  (upper panels) and  $\bar{\Lambda}$  (lower panels) hyperons

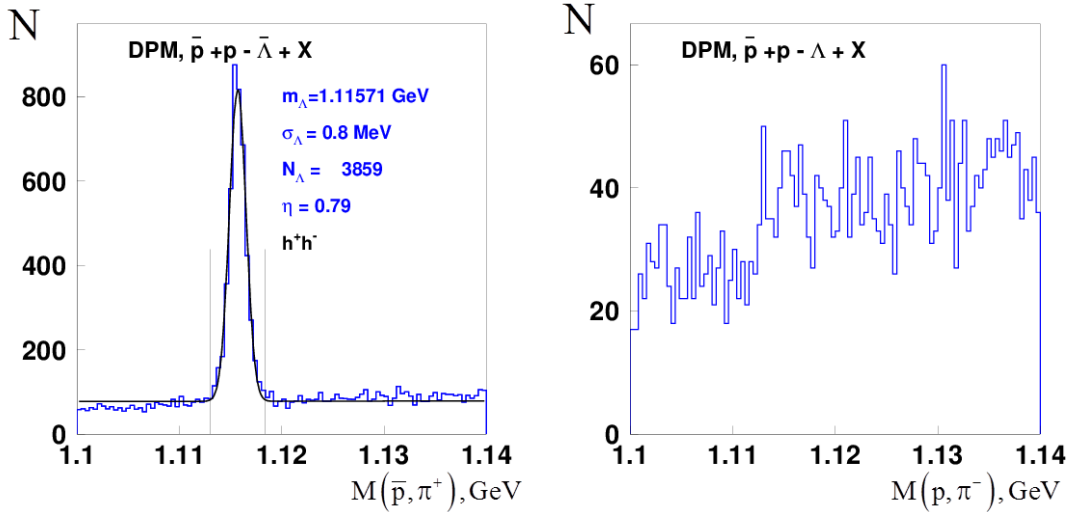


**Figure 4.12:** Invariant mass distribution for  $\bar{\Lambda}$  (left panel) and for  $\Lambda$  (right panel) with selection criteria A. The solid line in  $\bar{\Lambda}$  case shows result of fit performed with a Gaussian and second order polynomial. Fitting parameters are  $m_\Lambda$  ( $m_{\Lambda,PDG} = 1.11683$  GeV),  $\sigma_\Lambda$  (Gaussian peak dispersion),  $N_\Lambda$  (number of  $\bar{\Lambda}$  events) and  $N_{bgr}$  (background contribution under the peak),  $\eta = N_\Lambda / (N_\Lambda + N_{bgr})$

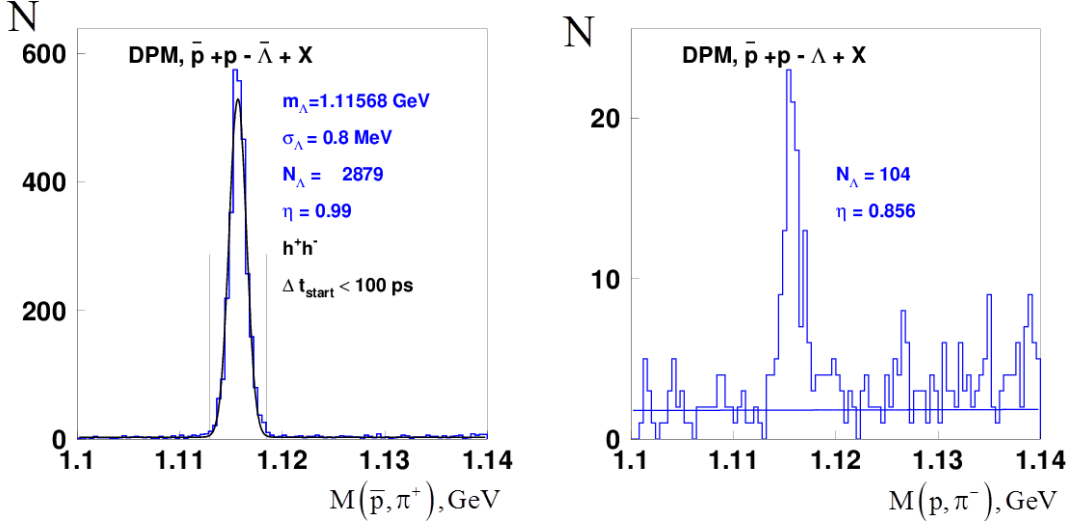


Figure 4.13: Invariant mass distribution for  $\bar{\Lambda}$  (left panel) and for  $\Lambda$  (right panel) with selection criteria A and B

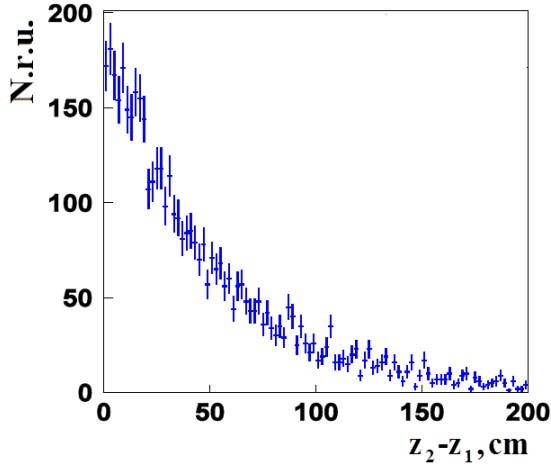


Figure 4.14:  $\bar{\Lambda}$  decay vertex distribution. Here  $z_1$  and  $z_2$  are production vertex (target) position and decay vertex position along the spectrometer axis, respectively

plied. For that, at least two hits must be detected by either ToF detector. The hit multiplicity distribution per event calculated for the  $\bar{\text{P}}\text{ANDA}$  time-of-flight detectors SciTil (BToF), FToF wall and, tentatively, for Dipole ToF are presented in Fig. 4.15.

The probability to detect more than one hit (double hit probability) may be defined as  $\epsilon = \frac{\sum_{i>1} N_i}{\sum_{i>0} N_i}$ , where  $i$  is a hit multiplicity. These numbers at 10 GeV  $\bar{p}$  beam are 48% and 38% for SciTil and FToF wall detectors, respectively. For the dipole

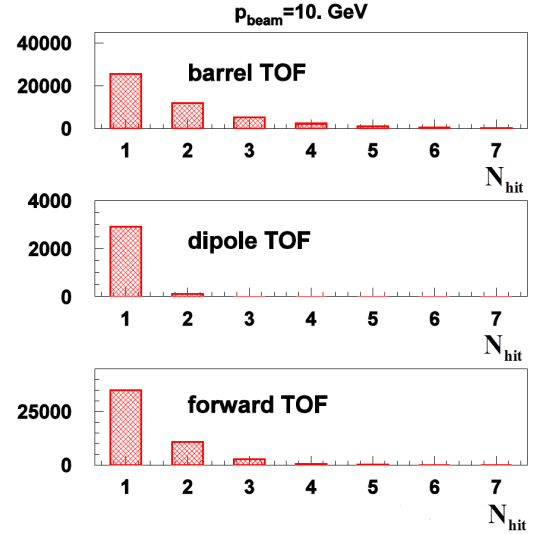
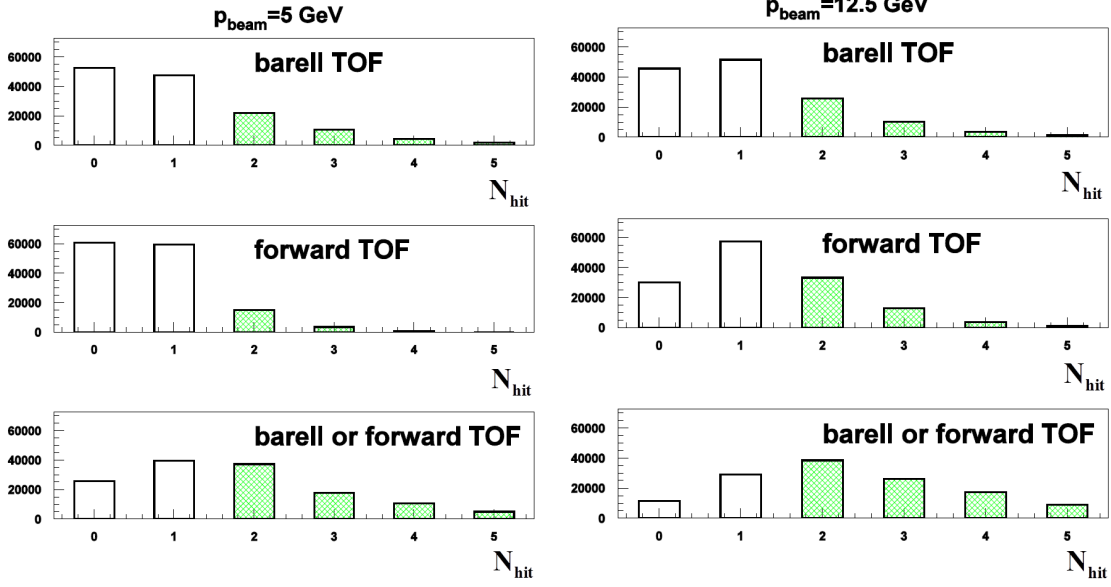


Figure 4.15: Hits multiplicity distributions for SciTil (barrel ToF), dipole ToF (DToF) and FToF wall (forward ToF) at 10 GeV  $\bar{p}$  beam

ToF the counting rate is by an order of magnitude less and the double hit probability is less than 5%. As it is seen from Fig. 4.16 the double hit probability increases with the beam momentum. In the lower panels of Fig. 4.16 the hit multiplicity distributions are shown with a green color for the case when either SciTil or FToF wall (at least) would detect more than one hit. The corresponding probabilities  $\epsilon$  are 61% and 80% for the beam momentum 5 GeV and 12.5 GeV, respectively.



**Figure 4.16:** Hits multiplicity distributions for SciTil (barrel ToF) and FToF wall (forward ToF) at 5 GeV and 12,5 GeV  $\bar{p}$  beam. The lower panels shows hits distributions for the case case when either SciTil or FToF wall (at least) would detect more than one hit

Another option for the application of the time-of-flight criterion is the coincidence between the two ToF detectors. The coincidence probabilities given in Table 4.4 increase with the beam momentum.

To conclude, the MC simulation confirms that the FToF wall is an important component of the PANDA experiment. It is used for hadron PID at the particle momenta below 4 GeV. With the help of FToF wall information the event start time can be obtained. The timing criterion for event reconstruction can be applied in many cases with a high efficiency. The count rate per a scintillation counter in the wall at the maximal luminosity stays below 1 MHz. The forward emitted  $\Lambda$  baryons can be used for calibrations and tuning of the detector.

## 4.5 Time-dependent Monte Carlo simulation

A study of the FToF wall detector performance using PANDAROOT is still in progress. The goal is to analyze particle hits detected with the FToF wall in a chronological sequence in order to find out how hits produced in consecutive events can be separated. The calculations with 5 GeV and 15 GeV beam for the high luminosity mode ( $2 \times 10^7$

interactions/s) have been performed. It has been preliminary shown that at 5 GeV there is practically no event overlap. However, this fraction is increasing with the beam momentum. The pileup effect is estimated to be small for the FToF wall. More detailed studies with information from other detectors included in the analysis will be done in the near future.

## 4.6 Optimization of the scintillator thickness and light guide configuration

For a fast PMT the time resolution is mostly determined by the PMT TTS (time transition spread) and number of the photons in the leading edge (front part) of the photon bunch arriving at the PMT photocathode. A Monte Carlo study of the light propagation in the plastic scintillator and the light guide has been performed in order to determine the number of photons in the leading edge of the photon pulse depending on the scintillator thickness. In the simulations, the 1 GeV proton track passed the slab through its center. The result is shown in Fig. 4.17.

As one can see, the optimal slab thickness is around 2.5 cm. Further enlarging the slab thick-

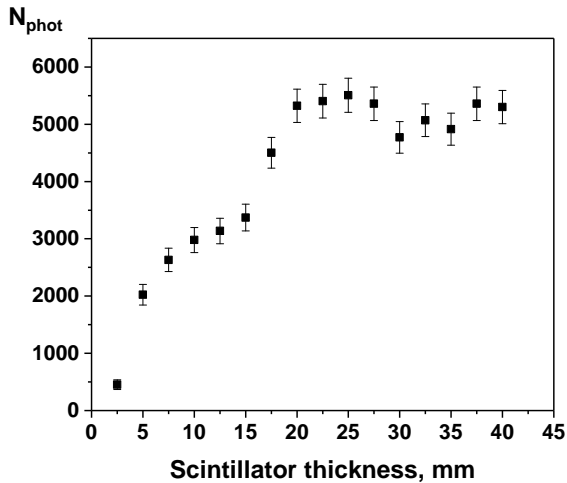


**Figure 4.17:** Number of photons in the leading edge of the photon pulse depending on the scintillator thickness

nesses does not increase the number of photons in the front part of the signal. In a similar way an optimal length of the light guide is found to be 12.5 cm which close to that assumed to use for the large slabs in this project.

## 4.7 PID and time resolution variants

The best time resolution ( $< 100$  ps) will be reached only off-line with all corrections done. It is important to know how sensitive the PID to the quality of time measurements, e.g., for preliminary analysis, one may use raw time measurements with much worse time resolution than the final one with all corrections made. The results of calculation of hadron mass reconstruction depending on time resolution is shown in Fig. 4.2.

## References

- [1] M. Kotulla et al. Technical Progress Report for PANDA: Strong Interaction Studies with Antiprotons. 2005.
- [2] A. Capella, U. Sukhatme, C-I Tan, and J. Tran Thanh Van. Dual parton model. *Phys. Rept.*, 236:225–329, 1994.
- [3] T. Orita, K. Shimazoe, and H. Takahashi. The dynamic time-over-threshold method for multi-channel {APD} based gamma-ray detectors. *Nuclear Instruments and Meth-*

*ods in Physics Research Section A: Accelerators, Spectrometers, Detectors and Associated Equipment*, 775:154 – 161, 2015.

- [4] I. Kipnis et al. A time-over-threshold machine: The readout integrated circuit for the BaBar silicon vertex tracker. *IEEE Trans. Nucl. Sci.*, 44:289–297, 1997.



## 5 Experimental study of prototypes

### 5.1 Study of photodetectors using test-station

#### 5.1.1 Test-station. General remarks.

The test-station is designed and built to examine the performance of commercially fabricated photo-detectors: photomultiplier tubes PMTs and silicon photomultipliers SiPMs (multi-pixel photon counters MPPC made up of multiple avalanche photodiodes). These studies are focused on the measurements of time characteristics and the optimization of their timing resolution. The measurements with the test-station help to select candidates for further prototyping with the help of proton beams. It is also planned that the approach worked out using the test-station is to be applied for tests and the preliminary calibration of the FToF wall modules in the process of their mass production.

#### 5.1.2 Investigation of PMTs

The test-stand layout for PMT investigations is shown in Fig. 5.1.

A cubic plastic scintillator with dimensions  $1 \times 1 \times 1 \text{ cm}^3$  made of BC-408 is viewed with two PMTs: PMT\_0 and PMT\_1, their photocathode face plates being attached to the scintillator at the opposite sides. An optical contact is provided with optical grease BC-630. The whole system is placed in a closed metal-tube box. The scintillator is irradiated by the electrons with energies up to 2.28 MeV from the  $^{90}\text{Sr}$   $\beta$  decay. The electrons pass through the window of  $100 \mu\text{m}$  thick black-paper sheet. The  $^{90}\text{Sr}$  radioactive source is placed in a lead container. Emitted electrons are collimated as shown in Fig. 5.1. The distance  $L$  varies from 20 mm for 1" PMTs to 30 mm for 2" PMTs.

The SCDA (continuous-slowng-down approximation) range for a 2 MeV electron is  $0.938 \text{ g/cm}^2$  with the radiation yield less than 0.6% [1] so that practically all emitted within the collimator acceptance electrons are stopped in the plastic scintillator. The maximum energy deposit is about 2 MeV. According to the BC-408 specification, this corresponds to the irradiation of  $2 \times 10^4$  photons.

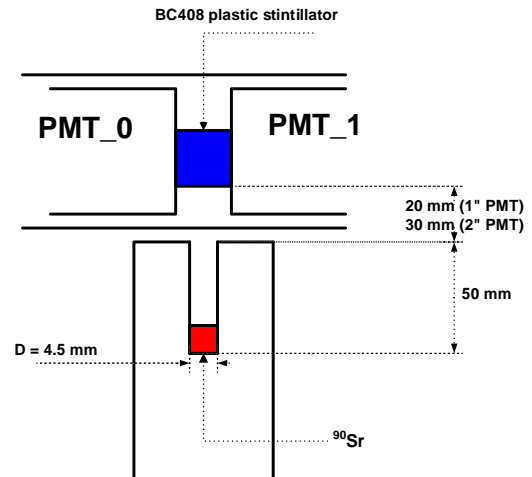


Figure 5.1: Layout of test-stand

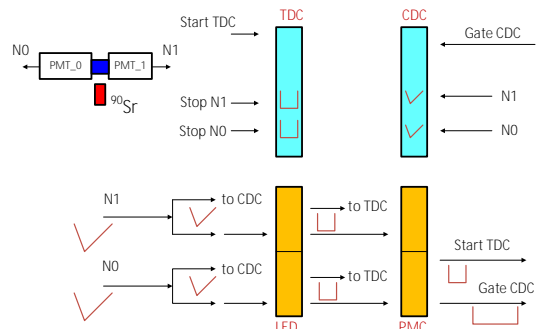


Figure 5.2: General layout of the test station electronics.  $N_0$  and  $N_1$  are signals of PMT\_0 and PMT\_1, CDC is charge-to-digital converter (LeCroy ADC 2249A, 250 fK/ch.), TDC is time-to-digital converter (16 Ch. CAEN V775 N, 35 ps/ch), LED is leading edge discriminator (8 Ch LeCroy 623B), PMC is programmable coincidence matrix (PNPI electronics 155/08)

The time resolution of a PMT under investigation is deduced from the  $t_1 - t_0$  spectrum measured with a simultaneous control of the PMT signal amplitudes. Here  $t_1$  and  $t_0$  are the time stamps of the PMT\_1 and PMT\_0 signals, respectively. The readout electronics scheme is shown in Fig. 5.2.

The signals  $N_0$  and  $N_1$  of PMT\_0 and PMT\_1 are divided into two halves with the help of passive splitters. One half of each signal comes to the

CDC to be used for the offline amplitude correction. Another half, after shaping with the help of the LED, goes to the PMC which produces a fast “Start TDC” pulse and “Gate CDC” signal. The LED threshold is set to 50 mV while the pulse amplitude varies typically in the range from 0.5 to 2 V. The time difference  $t_1 - t_0$  is measured between the time stamps given by “Start TDC” and “Stop  $N_1$ ” pulses. Time difference spectrum between “Start TDC” and “Stop  $N_0$ ” is used for the estimation of timing uncertainty due to electronics, e.g. due to resolution of the TDCs. The parameters of photomultipliers under investigation are listed in Table 5.1.

The signal and noise dependencies on HV values for the investigated Hamamatsu PMTs are presented in Fig. 5.3.

The following pairs of PMTs were investigated using the test station (Table 5.2).

When studying the PMTs pairs of the same type the HV was tuned such that the CDC distributions of the PMT\_0 and PMT\_1 were practically identical. In the analysis of obtained results, the time resolutions of the two PMTs were assumed to be equal in the corresponding data sample.

The typical raw spectra obtained for the R2083/R2083 pair are shown in Fig. 5.4. The amplitude spectra of the PMTs are practically identical. The “raw” time resolution measured with the TDC\_1 is  $RMS_{TDC.1} = 8.03 \text{ ch} \times 35 \text{ ps/ch} = 281 \text{ ps}$ .

The time resolution of the pair is improved to  $RMS_{TDC.1} = 2.74 \times 35 \text{ ps} = 96 \text{ ps}$  after cutting off low energy deposits (low CDC amplitudes) as shown in Fig. 5.5. The TDC\_0 spectrum, used to control the timing resolution in a “self start/stop” variant, is also somewhat improved giving  $RMS_{TDC.0} = 0.9 \text{ ch}$  (31.5 ps) thus showing that the contribution to the time resolution from electronics is mostly defined by the resolution of the used TDC.

Note that the CDC spectra after cutting off the low amplitudes are still having some residual amplitude spread which affects the time resolution. Further improvement of the time resolution can be achieved with the help of (offline) amplitude corrections as discussed in [2, 3, 4] where several variants of the amplitude correction are considered. The time walk of a PMT signal after LED correlates strongly with its amplitude. This correlation is shown in Fig. 5.6 where TDC\_1 is plotted versus  $1/\sqrt{Q_i} - 1/\sqrt{Q_k}$ . Here  $Q_0$  and  $Q_1$  is the charge collected by CDC 0 and 1, respectively.

The amplitude correction has been made by a fit to the data as described in details in Sec. 5.2.4. After this correction, it has been finally obtained  $\sigma_{TDC.1} = 72.6 \text{ ps}$  (Fig. 5.7).

The experimentally obtained time resolution of the R2083/R2083 pair can be decomposed as follows:

$$\sigma_{TDC.1}^2 = 2\sigma_{R2083}^2 + \sigma_{el}^2 + \sigma_S^2 \quad (5.1)$$

where  $\sigma_{R2083}^2$  characterizes the “net” time resolution of the PMT under study,  $\sigma_{el}^2$  is the contribution from electronics, and  $\sigma_S^2$  represents timing uncertainty due to the track position spread of the emitted electron in the plastic scintillator. Proceeding from above, the electronics contribution is  $\sqrt{\sigma_{el}^2} = 31.5 \text{ ps}$ . A conservative estimation of the track position uncertainty gives  $\sqrt{\sigma_S^2} = 3 \text{ mm} \times 5.27 \text{ ps/mm} = 15.81 \text{ ps}$ . Here we neglect a small difference in the scintillator position for the measurements with 1 inch and 2 inch PMTs. With these estimations one obtains  $\sigma_{R2083}^2 = 45 \text{ ps}$ . In order to obtain the resolution for R9779 the equation

$$\sigma_{R9779}^2 = \sigma_{TDC.1*}^2 - \sigma_{TDC.1}^2 \quad (5.2)$$

can be used, where  $\sigma_{TDC.1*}^2$  corresponds to the measurements for the R2083/R9779 pair. In a similar way the pairs of XP2020/XP2020, R4998/R4998 and R4998/R9800 have been analyzed. The results are summarized in Table 5.3.

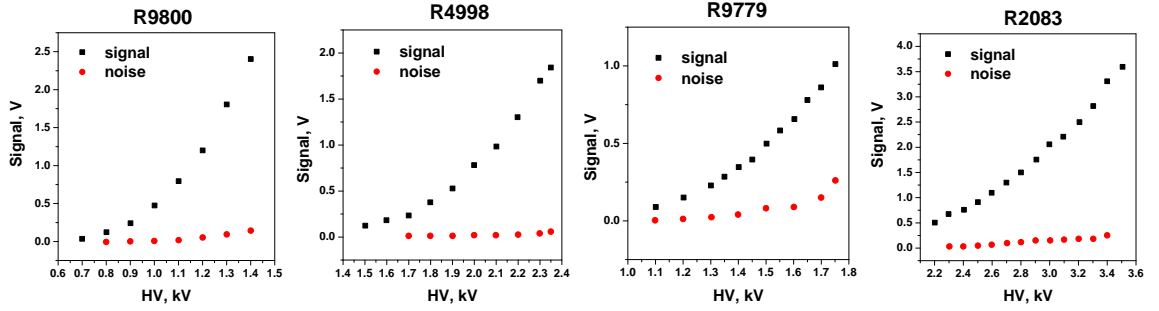
### 5.1.3 Measurement of SiPM characteristics

The studies of SiPM characteristics have been organized using the test-station described in Sec. 5.1.2. with minor mechanics and electronics modifications. As schematically shown in Fig. 5.8, two sets of MPPC modules have been studied: Hamamatsu S10931-50p, with an effective photosensitive area  $3 \times 3 \text{ mm}^2$  (variant A), and KETEK 6660, with an active sensor area  $6 \times 6 \text{ mm}^2$  (variant B). The dimensions of plastic scintillators used in the A and B variants are specified in Fig. 5.8. The scintillators were irradiated with the same radioactive source  $^{90}\text{Sr}$  as in Sec. 5.1.2. The maximum energy deposit of the emitted electrons is less than in the PMT case. It is estimated to be 0.75 MeV and 1.37 MeV for variants A and B, respectively.

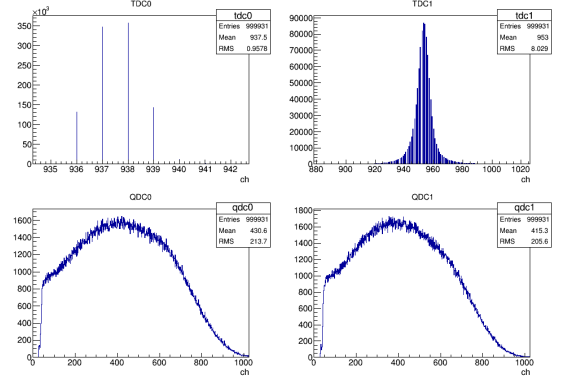
The SiPM signals are typically at the level of 50 - 80 mV being essentially less than those from

**Table 5.1:** Parameters of photomultipliers under investigation

PMT	Photocathode diameter, (mm)	Anode pulse rise time, (ns)	$e^-$ transition time, (ns)	Transition time spread, (ps)	Gain, $\times 10^6$	Typical voltage, (V)
R4998	25 (1")	0.7	10	160	5.7	2250
R9800	25 (1")	1.0	11	270	1.1	1300
R2083	51 (2")	0.7	16	370	2.5	3000
R9779	51 (2")	1.8	20	250	0.5	1500
XP2020	51 (2")	1.6	28	-	30	2000

**Figure 5.3:** Signal and noise versus applied HV for investigated PMTs**Table 5.2:** Pairs of PMT selected for investigations

1" PMTs			
PMT_0	PMT_1	Applied HV <sub>0</sub> (kV)	Applied HV <sub>1</sub> (kV)
R4998	R4998	2.0	1.9
R4998	R9800	2.0	1.35
2" PMTs			
PMT_0	PMT_1	Applied HV <sub>0</sub> (kV)	Applied HV <sub>1</sub> (kV)
R2083	R2083	2.7	2.7
R2083	R9779	2.7	1.6
XP2020	XP2020	2.35	2.25
XP2020	XP2020	2.5	2.36

**Figure 5.4:** CDC (QDC) and TDC spectra measured for pair of identical PMTs R2083/R2083.

overall the electronics time resolution.

The measurement results have been analyzed in the same way as in Sec. 5.1.2.

For variant A, it has been obtained  $\sigma_{TDC,1} = 550$  and 195 ps before and after cutting off low signal amplitudes. A correlation TDC/CDC similar to that shown in Fig. 5.6 has been also observed for SiPMs. After the amplitude correction the time resolution has been improved to  $\sigma_{TDC,1(corr)} =$

PMTs. A fast preamplifier (4AMP 165.37, PNPI made electronics with 3 ns rise time and adjustable voltage gain from 4 to 8) has been used for the amplification of the SiPM signals. It must be noted that introducing a fast preamplifier in the electronics scheme does not practically worsen

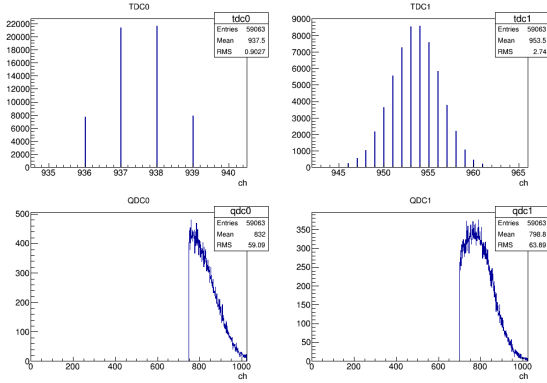


**Figure 5.5:** Same as in Fig. 5.4 after cuts on CDC spectra.

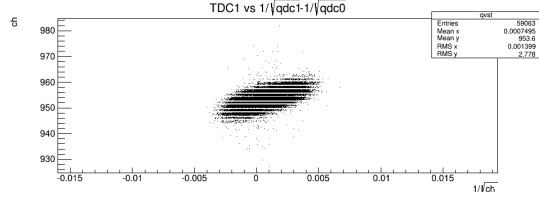


**Figure 5.6:** Correlation between TDC\_1 and value of  $1/\sqrt{Q_i} - 1/\sqrt{Q_k}$

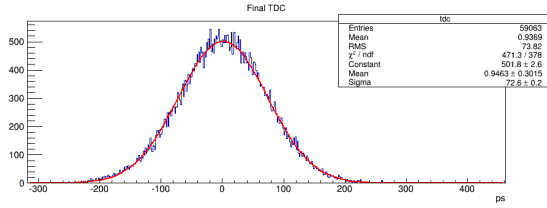


**Figure 5.7:** Final TDC-1 spectrum after amplitude correction.

**Table 5.3:** Time resolutions obtained at test station

PMT_1	$\sigma_{TDC_1}$ (ps)	$\sigma_{PMT}$ (ps)
R4998 (4998/4998)	72.0	44.4
R9800 (4998/9800)	86.0	64.6
R2083 (2083/2083)	72.6	44.9
R9779 (2083/9779)	64.0	56.5
XP2020 (2020/2020)	82.0	52.3

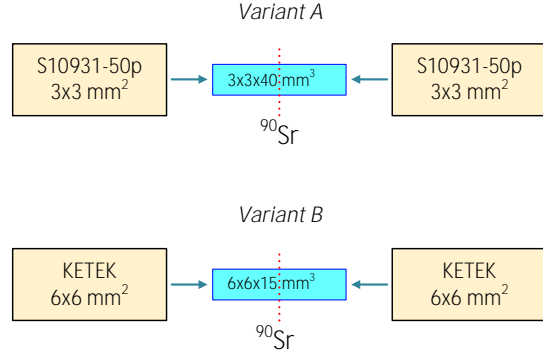


**Figure 5.8:** Two variants of measurements of SiPM characteristics

150 ps. Using Eq.5.1 with the same values of  $\sigma_{el}^2$  and  $\sigma_s^2$  as in Sec. 5.1.2. one obtains  $\sigma_{S10931}=103$  ps.

More promising results have been obtained for KETEK 6660 (Table 5.4). The best resolution of 66 ps is just a little worse than those for PMTs. One should remember that the amount of irradiated photons here is less than in the PMT tests.

The “raw” signal of KETEK 6660 SiPM has a long tail of about 150 ps. This limits the maximal count rate to  $\sim 50$  KHz in a practical utilization of these MPPC array. Besides, it complicates CDC measurements. The latter difficulty can be solved using of a RC differentiating circuit at the output. The pulses of two KETEK 6660 SiPMs passed through the differentiator with  $RC = 1 \text{ k}\Omega \times 500 \text{ pF}$  are shown in Fig. 5.9.

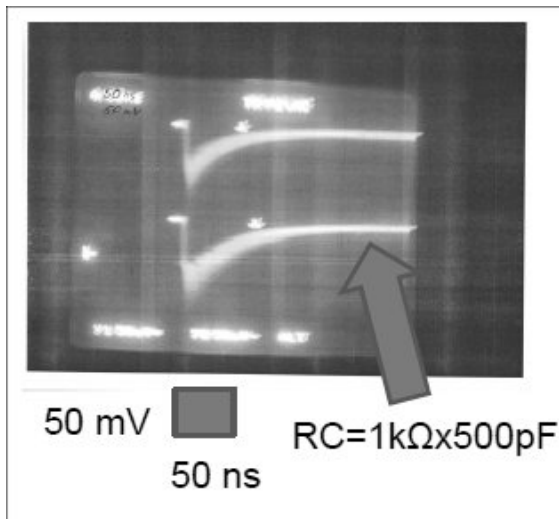
In practical applications of SiPMs, an important issue is their radiation hardness. We have performed a very preliminary study of the SiPM radiation hardness exposing a not powered S10931-50p SiPM ( $3 \times 3 \text{ mm}^2$ ) sample to a 1 GeV extracted proton beam of the PNPI synchroclotron. The beam intensity during the tests was  $2.1 \times 10^8 \text{ cm}^{-2}\text{s}^{-1}$ . The sample was irradiated in ten successive periods about 10 minutes each. The integrated number of protons which passed through the active area of the sample was  $0.45 \times 10^{11}$ . The characteristics of the investigated SiPM sample were measured at the test-stand before and after the irradiation run. The results shown in Table 5.5 demonstrate that the not powered sample could not tolerate the irradiation dose mentioned above. Further detailed studies are needed in order to investigate to which integrated radiation dose a SiPM module is operational.

**Table 5.4:** Main parameters and time resolution of KETEK 6660

Supply voltage (V)	Signal amplitude (mV)	Noise amplitude (mV)	Current without $^{90}\text{Sr}$ ( $\mu\text{A}$ )	Current with $^{90}\text{Sr}$ ( $\mu\text{A}$ )	$\sigma_{TDC.1}$ (ps)	$\sigma_{TDC.1}/\sqrt{2}$ (ps)	$\sigma_{KETEK}$ (ps)
26.35	20÷30	~0.3	7.5	9	120	84.8	81.1
26.85	70÷90	~0.5	11	13	100	70.7	66.1

**Table 5.5:** Signal amplitude, noise count rate and dark current of the S10931 SiPM sample before and after exposition to the 1 GeV proton beam

Supply voltage (V)	Signal amplitude before irradiation (mV)	Noise before irradiation (kHz)	Dark current before irradiation ( $\mu\text{A}$ )	Signal amplitude after irradiation (mV)	Noise after irradiation (kHz)	Dark current after irradiation ( $\mu\text{A}$ )
72.06	40	1.55	0.15	4	2.8	81
72.53	80	4.2	0.3	6	99	113

**Figure 5.9:** Pulses of two KETEK 6660 SiPMs passed through the differentiator

## 5.2 Study of prototypes using proton beam

### 5.2.1 Introduction

The configuration of the plastic scintillators for the FToF wall and selection of the corresponding photo detectors were discussed above. All PMTs selected for the tests using proton beams had been preliminary investigated using the test sta-

tion Sec. 5.1. Based on this information, several scintillation counters were assembled (Table 5.6). The plastic scintillators were made of BICRON 408 (BC408). The light guides were made of Plexiglas. Optical contacts were provided with an optical grease BC630. The light guide with a truncated cone (fish tail) configuration for the PMT of 1" or 2" diameter is shown in Fig. 5.10. Small scintillation counters with plastic scintillators  $2 \times 2 \times 2 \text{ cm}^3$  or  $1 \times 1 \times 1 \text{ cm}^3$  were also used in the test experiments. The small scintillation counter was coupled with a single, either, Hamamatsu R4998 or Electron 187 PMT.

A series of measurements were performed at the 1 GeV PNPI synchrocyclotron during the period from year 2008 to 2014. Preliminary results of these studies can be found in [1]. In the year 2012, there was a run of test measurements at the 2 GeV proton beam at the Jessica area of the COSY accelerator in Jülich.

### 5.2.2 Test of scintillation counter prototypes at the PNPI synchrocyclotron

The measurements were performed with the help of one arm of the experimental facility used in a series of experiments on polarization in quasi-elastic ( $p, 2p$ ) scattering [5][6][7]. A 1 GeV extracted proton beam of the PNPI (Gatchina) synchrocyclotron was focused onto a polyethylene

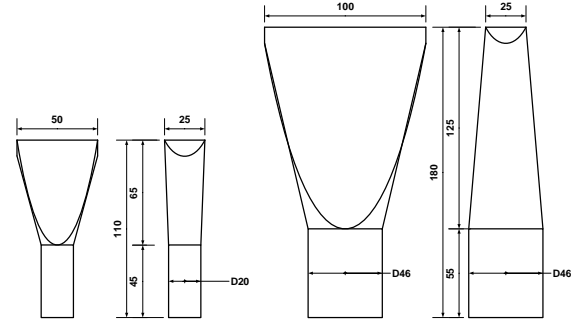
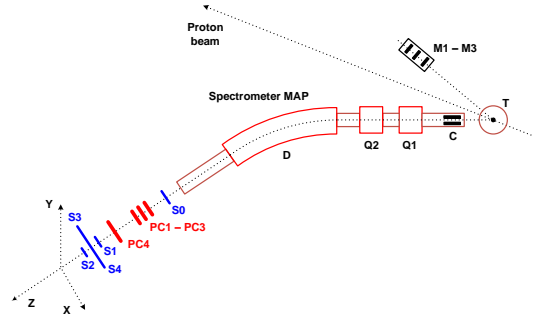
**Table 5.6:** Prototypes of scintillation counters tested at proton beams

Scintillator dimensions, cm	Photomultipliers
$1.5 \times 5 \times 140$	Hamamatsu R4998 (both ends)
$1.5 \times 10 \times 140$	Hamamatsu R2083 (both ends)
$2.5 \times 2.5 \times 140$	Hamamatsu R4998 (both ends)
$2.5 \times 5 \times 140$	Hamamatsu R4998 (both ends)
$2.5 \times 10 \times 140$	Hamamatsu R2083 (both ends)
$2.5 \times 2.5 \times 140$	Electron 187 (both ends)
$2.5 \times 5 \times 140$	Electron 187 and Hamamatsu R4998
$2.5 \times 5 \times 140$	Electron 187 (both ends)
$2.5 \times 10 \times 100$	Electron 187 (both ends)
$2.5 \times 10 \times 100$	Electron 187 and Hamamatsu R4998

target of the MAP spectrometer (Fig. 5.11). The protons scattered elastically from hydrogen in the target were selected by the spectrometer at a certain scattering angle  $\theta_p$ . The spectrometer was mounted on a movable platform which allows one to vary the angle  $\theta_p$  and thus to set a appropriate scattered proton energy  $E_p$ . The measurements were performed at two sets of the proton energies and angles:  $E_p=730$  MeV at  $\theta_p = 26.0^\circ$  and  $E_p = 920$  MeV at  $\theta_p = 13.5^\circ$ .

The momentum uncertainty of the scattered protons was defined by the energy spread of the extracted beam [8], the spectrometer angular acceptance  $\theta_p$  and the momentum resolution of the spectrometer, the latter ( $\Delta p/p$ ) being about 0.005.

A conservative estimation of the overall uncertainty of the scattered proton momentum was  $\pm 5$  MeV/c. The target dimensions seen by the spectrometer were  $\pm 11$  mm in a horizontal plane and  $\pm 7.5$  mm in a vertical direction. The spectrometer horizontal and vertical angular acceptances were restricted to  $\pm 0.007$  and  $\pm 0.016$ , respectively, by the collimator C. The protons scattered from the target were focused by two quadrupole lenses  $Q_1$

**Figure 5.10:** The light guides for the plastic scintillators of 2.5 cm thickness, 5 cm width (left) and for the plastic scintillators of 2.5 cm thickness, 10 cm width (right)**Figure 5.11:** The experimental setup to study scintillation counter prototype characteristics at the PNPI proton beam. M1-M3 is scintillation telescope to monitor beam intensity, T is polyethylene target, C is collimator restricting horizontal and vertical spectrometer acceptance,  $Q_1$ ,  $Q_2$  are focusing quadrupoles, D is dipole magnet. Vacuum system of the spectrometer is shown with thin red lines. PC1, PC2 and PC3, PC4 are multiwire proportional chambers to measure  $x, y$  coordinates of a track, S0 is start scintillation counter producing common trigger. S1, S2 are small scintillation counters ( $2 \times 2 \times 2$  cm<sup>3</sup>). S3 and S4 are PMTs at both ends of the slab of the scintillation counter S34.

and  $Q_2$ , and partly by the dipole, onto the focal plane located in between the multiwire proportional chamber PC2 and PC3. The scattered protons (as well as the beam) were mostly transported in vacuum. The proportional chambers PC1, PC2 and PC3, PC4 with 1 mm and 2 mm wire spacing, respectively, were used to measure the  $x, y$  coordinates of a track at the location of the scintillation counter S34 (S3,S4) under investigation.

A long slab of the tested scintillation counter S34 was placed horizontally behind the PC4 (see pho-

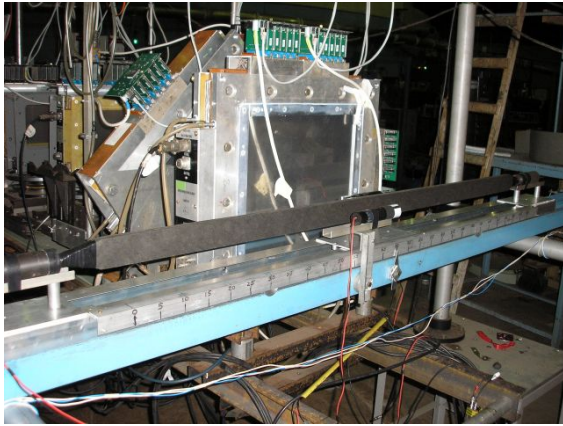


**Figure 5.12:** The scintillation counter prototype S34 mounted on the movable platform behind the multiwire proportional chamber PC4. A proportional chamber seen upstream of the PC4 with wires rotated by  $45^\circ$ . The PC4 was not used in these measurements.

tograph in Fig. 5.12) at 126 cm downstream of the spectrometer’s focal plane. The counter was mounted on a movable platform equipped with remotely controlled electric motors. Measurements were carried out at 14 positions of the slab moving along the  $x$  axis starting from the end of the slab viewed with the S3 PMT. As shown in Fig. 5.11 the right-handed coordinate system is used with  $z$  directed along the spectrometer axis, the  $x$ -axis perpendicular to the  $z$ -axis in the horizontal plane and  $y$  axis perpendicular to the horizontal plane. The slab position along the  $x$  axis was fixed by the value of  $x$  measured from the center of the slab. For a slab of 140 cm length  $x$  ranges from -70 to 70 cm. The positions of the small scintillation counters S1 and S2 were fixed. The counters were aligned along the  $z$ -axis and centered at  $x = y = 0$ . The S1(S2) PMT collected photons moving antiparallel (parallel) to the  $x$ -axis in direction (opposite) to S3 PMT. In most of the measurements, the slab was set at  $y = 0$ . The  $y$  position of the slab could be changed under manual control. It was also possible to turn the S34 counter around the  $x$ -axis in order to vary the effective energy deposition in the scintillator.

The start counter S0 was made large enough not to restrict the spectrometer acceptance. A part of the data were taken “inclusively” based on S0 triggers only. In this case, the peak of elastic  $pp$ -scattering projected on the slab formed a spot of  $35 \text{ mm} \times 60 \text{ mm}$ . The inclusive count rate of the S34 counter was mostly determined by the proton hits within this spot.

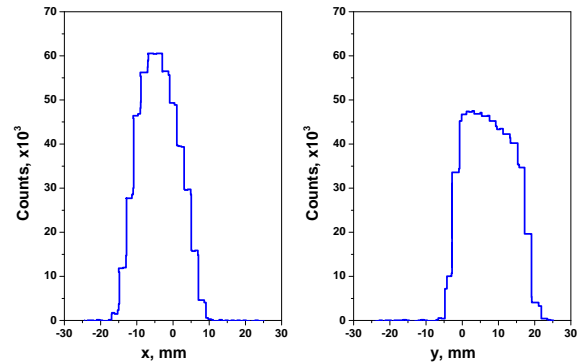


**Figure 5.13:**  $x$  distribution (left) and  $y$  distribution (right) at the slab measured under the condition of S0S1S2 coincidences

Most of the data were collected under the condition of the S0S1S2 coincidences. Owing to this condition the proton hit area was restricted to a smaller spot defined by the geometry and the mutual positions of the S1 and S2 scintillators. The corresponding distributions are shown in Fig. 5.13.

The hit position on the slab was specified within this spot due to the tracking information obtained with the help of PCs. The overall uncertainty of the hit position on the slab in the  $x$ -coordinate is estimated as  $\sigma_x \approx 1.8 \text{ mm}$ . Taking into account the refractive index (1.58 for the plastic scintillator BC408), this corresponds to a timing uncertainty of  $\sigma_t \approx 9.5 \text{ ps}$ .

### 5.2.3 Readout electronics

Implementation of the readout electronics sketched in Fig. 5.14 was similar to that described in Sec. 5.1. Both, the timing and amplitude information from each scintillation counter as well as the tracking system information on the hit position was needed for the precise determination of timing intervals in the offline analysis. An analog signal from each PMT (S1, S2, S3, S4) was split into two halves with the help of a passive splitter. One signal after the splitter came to a QDC module (LeCroy ADC 2249A, 250 fC/ch) for offline amplitude correction. Another signal came to a Leading Edge Discriminator LED (LeCroy 623B) which produced a fast pulse at the “STOP” input of the TDC (CAEN V775N, 35 ps per channel). The pulses “START” TDC and “GATE” QDC were activated by the signal from the S0 PMT passing through the CFD (Constant Fraction Discriminator) under

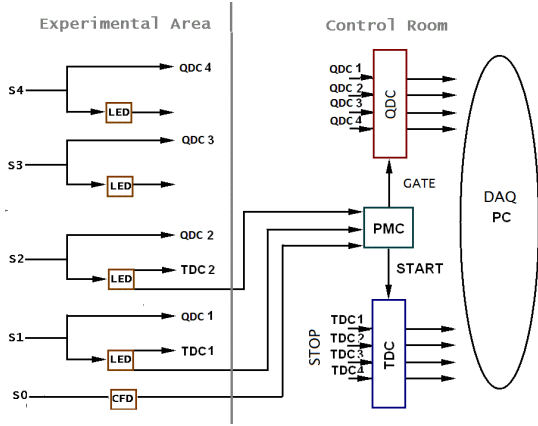


**Figure 5.14:** Scheme of readout electronics, explanations are given in text

the condition of coincidences among S0S1S2. The coincidences were realized with the help of the programming coincidence matrix PMC (production of PNPI). The LED threshold was adjusted to 50 mV while a typical amplitude of the analog signal at the LED input was 0.5 - 2.5 V and the pulse rise time was about 2 ns.

As far as the analog PMT signal was always well within the “GATE” pulse, the measured integrated charge was proportional to the pulse amplitude. Thus, a correction can be made to compensate on event basis for the timing uncertainty of the discriminator (LED) (time walk) because of the pulse amplitude variations.

As shown in the Fig. 5.14, a part of the electronics is situated in the experimental hall (a frontend part) while the other in the Control Room. They are labelled with “Experimental Hall” and “Control Room”, respectively. The connecting cables were of 50 m length.

In addition to the information from the TDC and QDC, an *event* contained the tracking information from the PCs together with Slow Control data, like slab positions, inclusive count rates of the scintillation counters, proton beam characteristics, etc.. The local data acquisition (DAQ) system was capable to accumulate events at the rate of 10kHz.

## 5.2.4 Data analysis

A typical example of the integrated charge  $Q$  distribution of the S3 and S4 PMTs (raw QDC distributions) is presented in Fig. 5.15.

The data have been obtained at tests of the slab

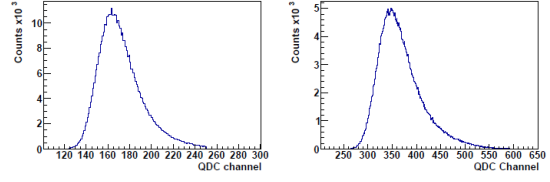


**Figure 5.15:** Integrated charge  $Q$  distributions of S4 PMT (left) and S3 PMT (right), measured at 920 MeV for the slab  $2.5 \times 5 \times 140 \text{ cm}^3$  positioned at  $x = -60 \text{ cm}$

with dimensions  $2.5 \times 5 \times 140 \text{ cm}^3$  using 920 MeV protons with the scintillation slab coupled to two R4998 PMTs. The slab was positioned at  $x = -60 \text{ cm}$ .

The observed distributions are intermediate ones between Landau and Gaussian type distributions. One may try to interpret this shape as a fluctuation of the proton energy loss in the slab. For relativistic protons a standard deviation  $\sigma$  of the Gaussian distribution can be estimated as [9]:

$$\frac{\sigma}{\Delta E} = \frac{\sqrt{0.153 m_e \frac{Z}{A} \rho t \frac{E_p}{M_p}}}{\Delta E} = 0.097 \quad (5.3)$$

Here  $\Delta E$  is the energy deposition in the slab,  $m_e$  and  $M_p$  are the electron and proton mass,  $E_p$  is the proton energy,  $\rho$  and  $t$  are the scintillator density and thickness,  $Z/A$  for BC408 is 0.542. The Landau equation gives a close value:  $\sigma/\Delta E \sim 0.1$ . Experimentally,  $\sigma_{meas} = 0.126$  and  $0.132$  have been obtained for QDC3 and QDC4, respectively. It is important that the  $Q$  fluctuations are quite moderate and thus may be corrected for offline.

In order to simulate the time-of-flight measurements experimentally, the time interval  $t_{ik} = t_k - t_i$  distributions obtained with the help of TDCs were analyzed. Here  $t_i(t_k)$  is a time stamp for the detected particle to pass through the plastic scintillator of the counter  $S_i(S_k)$ ,  $i(k) = 1, 2, 3, 4$  ( $k > i$ ). In the measurements of timing resolutions one of the small counters was conditionally assumed to be a “start” while S3 or S4 was a “stop”. An example of the raw TDC distributions is shown in Fig. 5.16. In addition to the measured time-of-flight, a raw distribution contains two dependencies: dependence on pulse amplitude (time walk due to frontend electronics threshold) and variation of the delay of photon pulse arrival at the PMT photocathode related to spread of hit positions of the detected particle along the scintillator. The two dependencies are kept under con-

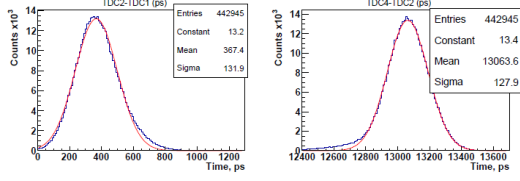


**Figure 5.16:** Typical raw spectra for time differences  $t_{21}$  (left) and  $t_{42}$  (right) measured at 920 MeV for the slab  $2.5 \times 5 \times 140 \text{ cm}^3$  positioned at  $x = 60 \text{ cm}$

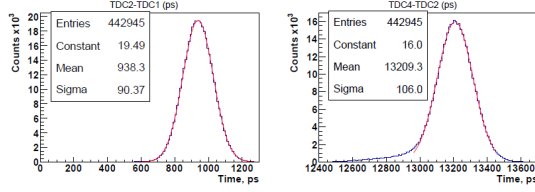


**Figure 5.17:** Same as in Fig. 5.16 after amplitude correction

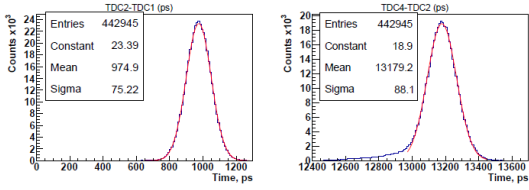


**Figure 5.18:** Same as and in Fig. 5.16 after amplitude and hit position corrections

trol in the experiment, and the "net" measured time-of-flight can be found after correction for these dependencies. The distributions corrected for the pulse amplitude and for the pulse amplitude and hit position as well are shown in Fig. 5.17 and Fig. 5.18, respectively.

The applied corrections are based on the correlations between the observed values of the raw  $t_{ik}$  and the pulse amplitudes  $Q_i$ ,  $Q_k$  or the hit position are presented in Fig. 5.19 and Fig. 5.20. The correlations are most pronounced in the case of small counters ( $t_{12}$  in Fig. 5.19). A linear dependence of  $t_{12}$  on the hit position is clearly seen. Various types of dependencies on  $Q_i$ ,  $Q_k$  were probed in [2], though a sensitivity to a type of the dependence was not too high. The latter can be easily understood taking into account that the fractional variation of the  $Q$ -value is not large ( $\pm 13\%$ ). Naively, one would expect that the am-

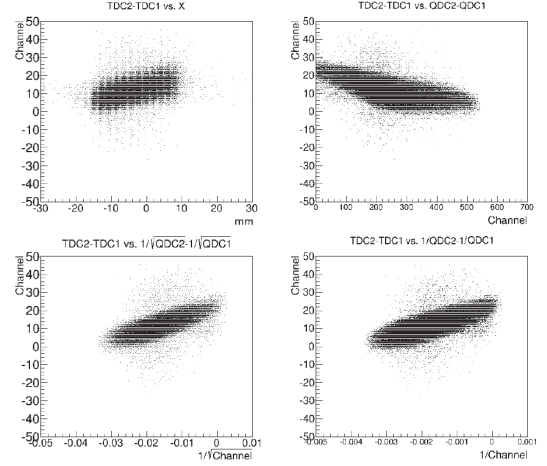


**Figure 5.19:** Time-coordinate and time-charge correlations for the  $t_{12}$  time-of-flight

plitude correction for an individual counter is proportional to  $1/Q$  provided that a linear rise time of the PMT pulse is realized while  $1/\sqrt{Q}$  is expected for the rise time of parabolic shape [2]. The corrections are made for a given event using the following equation:

$$t_{ik} = t_{ik}^{raw} - f^{corr} = t_{ik}^{raw} - Ax - B \left( \frac{1}{\sqrt{Q_i}} - \frac{1}{\sqrt{Q_k}} \right) - C \quad (5.4)$$

where  $t_{ik}$  and  $t_{ik}^{raw}$  represent the corrected and raw time intervals, respectively, measured with  $\text{TDC}_k - \text{TDC}_i$ . For a given data sample, the parameters  $A, B, C$  are found from the fit performed by means of minimizing the functional 5.5 which represents the dispersion of the  $t_{ik}$  distribution:

$$\langle t_{ik}^2 \rangle - \langle t_{ik} \rangle^2 = \frac{1}{N} \sum_{n=1}^N t_{ik,n}^2 - \left( \frac{1}{N} \sum_{n=1}^N t_{ik,n} \right)^2 \quad (5.5)$$

Here  $n$  is the event number and  $N$  is the total number of events in a data sample. Thus  $t_{i,k}^{raw}$  ( $n = 1 \dots N$ ) is corrected with the help of the  $f^{corr}$  function on the event basis and, finally, a corrected distribution over  $t_{ik}$  can be built with the time resolution given by the dispersion  $\sigma$  of this distribution.

To conclude, the correction for the hit position and pulse amplitude spread is crucially important to obtain a timing resolution better than 100 ps. Having the corrections applied, here it has been obtained  $\sigma(t_{24}) = 88 \text{ ps}$ . If S1 was taken as a

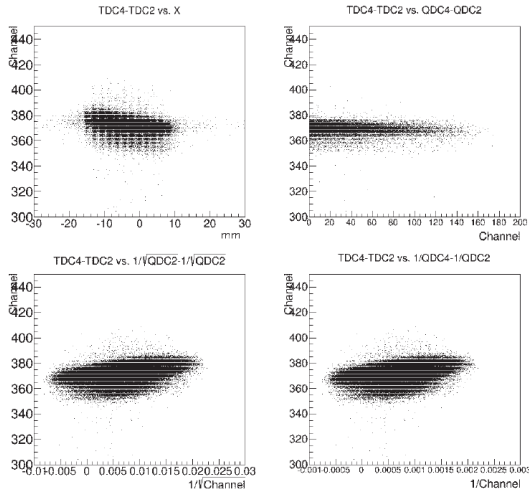


**Figure 5.20:** Time-coordinate and time-charge correlations for the  $t_{24}$  time-of-flight

start counter the result was just somewhat worse:  $\sigma(t_{14}) = 94$  ps. The timing resolution of the S3 at the opposite end of the slab was much worse (170 ps) because of much less number of photons reached the PMT3 photocathode. However, the overall timing resolution of the S34 scintillation counter  $\sigma_{34}$  is always better than 100 ps as it is given by the weighted mean of the measurements made with both S3 and S4 PMTs, i.e.  $1/\sigma_{34}^2 = 1/\sigma_3^2 + 1/\sigma_4^2$ .

### 5.2.5 Tests with 730 MeV protons

This was the first test run at the proton beam. A scintillation counter to be tested was assembled on a  $1.5 \times 5 \times 140$  cm<sup>3</sup> slab viewed with a R4998 PMT (S3) from one side only. The time-of-flight resolution of  $t_{12}$  (between S1 and S2 counters) was measured at first. It was found to be  $\sigma = 70$  ps after offline corrections. An important part of the program was to study the dependence of the timing resolution on the energy deposition in the slab. In order to perform this study a possibility was realized of turning the slab around the  $x$ -axis and thus varying the effective thickness of the scintillator in the range from 1.5 to 5 cm. The result of the measurements is demonstrated in Fig. 5.21.

The timing resolution for hits in the middle of the slab is improving with the increase of the energy deposition as expected. The scintillator thickness, however, should be optimized proceeding from several, other than the best timing resolution, considerations. A serious limitation of the

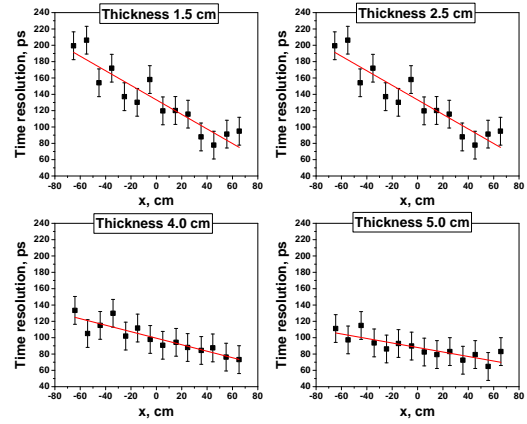


**Figure 5.21:** Timing resolution versus effective thickness of the plastic scintillator: 1.5 cm (left upper panel), 2.5 cm (right upper panel), 4 cm (left lower panel) and 5 cm (right lower panel)

scintillator thickness is the admitted extent of the ToF wall along the PANDA spectrometer axis and the fact that it will be situated in front of the FS calorimeter. A thickness of more than 2.5 cm will be hardly possible because of the limitations discussed above.

As seen from Fig. 5.21, the timing resolution is getting better with increasing  $x$  (proton hit position approaching the PMT S3). Such a behavior is well approximated with a linear dependence. At 2.5 cm thickness, the timing resolution is 125 ps in the middle of slab. The weighted mean then (provided the slab is viewed from both ends) would be better than 90 ps which meets the requirements of the PANDA experiment. Furthermore, this is true for any hit positions on the slab.

A further consideration here is that the energy loss of the 730 MeV protons is by a factor of 1.2 larger than that for minimum ionizing particles (MIP). One would expect then a somewhat worse resolution for the increasing proton momenta up to that corresponding to the MIP particles. However, due to a gradual perfection of the experimental techniques, no worsening of the timing resolution was observed at tests in the latest series of the measurements made with 920 MeV protons (see next section) and at a higher proton momentum at a test beam in Jülich.

### 5.2.6 Tests with 920 MeV protons

A wide program of tests has been performed in recent years in a series of runs using 920 MeV protons. All the types of large scintillation coun-

ters listed in Table 5.6 were tested and some of them tested several times. In the latest run in May 2014, a scan on the inclusive count rate of a slab was made in order to define the maximum count rate at which the scintillation counter prototype could still operate.

In addition to the slabs of 140 cm length, the 100 cm slabs preliminary foreseen for the installation in the dipole magnet were investigated using PMT187. According to Electron firm specification these mesh dynode PMTs can operate in magnetic fields up to 0.5 T.

The main results on the timing resolution measured at 920 MeV are presented in Fig. 5.22. The best timing resolution of 43 ps ( $\sigma$ ) given by the weighted means was obtained for the slab with cross section  $2.5 \times 2.5$  cm<sup>2</sup>. A value of 60 ps was obtained for  $2.5 \times 5$  cm<sup>2</sup> and slightly worse than that for the slab with cross section  $2.5 \times 10$  cm<sup>2</sup>. In all the cases the requirement “better than 100 ps” was satisfied.

Most of measurements were made at  $y = 0$  position. In principle, the number of photons collected at the PMT photocathode and time resolution might also depend on the  $y$ -position of the hit. However, no effect of the  $y$ -position of the slab on the timing resolution was experimentally seen.

Of particular interest was the timing resolution of the PMT 187. In a “well focused photons case” which had been realized for the  $2.5 \times 2.5 \times 140$  cm<sup>3</sup> slab they showed a good resolution of about 80 ps (Fig. 5.23). For a wider slab ( $2.5 \times 10 \times 100$  cm<sup>3</sup>) the resolution deteriorated to 120 ps.

According to Monte Carlo simulations the integrated rate of the central slab in the ToF wall is expected to be the highest one, being related mostly to elastic  $\bar{p}p$  scattering (Sec. 4.2). At the maximum luminosity corresponding to about  $10^7$  interactions in the target the central counters should stand against an inclusive count rate of  $2 \times 10^6$ .

In the PNPI test experiments the inclusive count rate of the S34 counter was monitored (with scalers not shown in Fig. 5.14). As most of the timing resolution measurements were performed at a moderate count rate of about 10 kHz, a scan on the beam intensity was made while monitoring the inclusive S34 rate. The  $2.5 \times 5 \times 140$  cm<sup>3</sup> slab assumed as a prototype for the central part of the ToF wall was tested. The results are given in Table 5.7. Here the rates have been corrected (multiplied) by a factor of 2.5 due to not a ho-

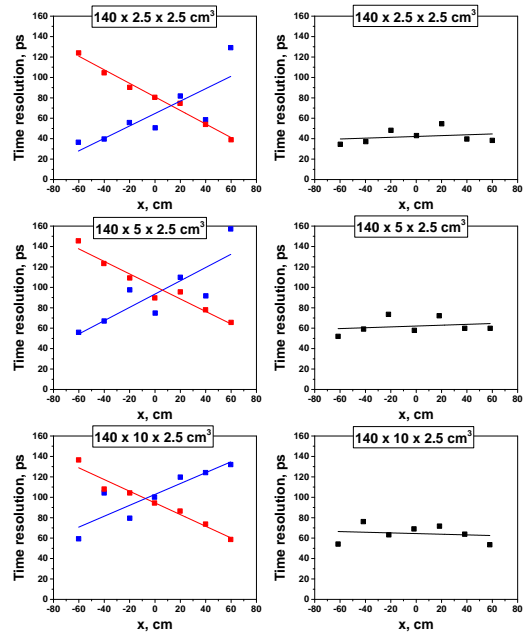


**Figure 5.22:** Timing resolution for various scintillation counter prototypes with S3 (red line) and S4 (blue line) PMT versus slab position (left panels) and corresponding weighted means (right panels). From top to bottom, the slabs investigated are:  $2.5 \times 2.5 \times 140$  cm<sup>3</sup> with PMT R4998,  $2.5 \times 5 \times 140$  cm<sup>3</sup> with PMT R4998 and  $2.5 \times 10 \times 140$  cm<sup>3</sup> with PMT R2083, respectively

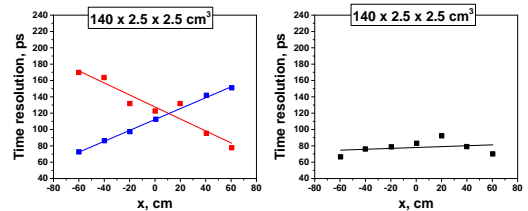


**Figure 5.23:** Timing resolution for scintillation counters with PMT Electron 187, S3 (blue line) and S4 (red line), versus slab position (left panel) and corresponding weighted means (right panel)

mogeneous time-macro-structure of the extracted proton beam (correction for duty factor). No deterioration of the timing resolution was observed for increasing the integrated rate of scattered protons up to  $2 \times 10^6$  s<sup>-1</sup>.

## 5.2.7 Measurements with 2000 MeV proton test beam of COSY accelerator

In December 2012 a scintillation counter prototype built of the scintillation slab  $1.5 \times 5 \times 140$

**Table 5.7:** Timing resolution at high inclusive rates of the S3S4 counter

Inclusive count rate, kHz	600	1100	1700	2000
$\sigma$ (weighted mean), ps	67	76	75	76

cm<sup>3</sup> equipped with two PMTs R4998 was tested in the Jessica area at the COSY proton ring in Jülich.

The measurements at COSY were aimed at the following tasks:

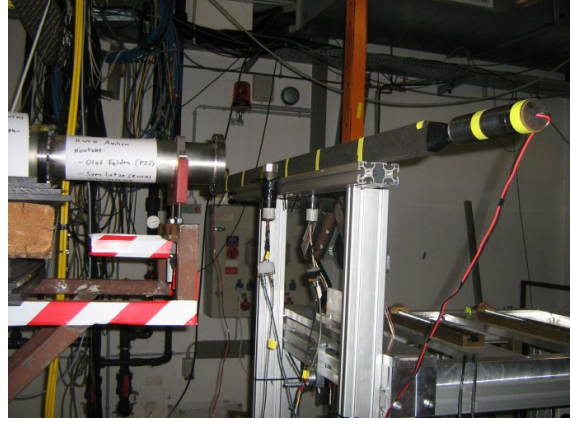
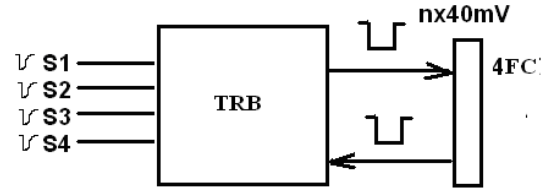
1. To repeat measurements at another proton energy which would approximately correspond to the minimum energy deposition in the slab;
2. To measure the timing resolution of slabs with 2.5 cm thickness and 1.5cm thickness;
3. There was an opportunity to carry out the measurements with TRB 2 (Trigger and Readout Board, version 2) readout. This system was formerly developed for the HADES experiment [10] and now it is in an upgrade phase for PANDA.

The measurements were performed using a 2 GeV proton beam at the relatively low beam intensity of  $10^4 \text{ s}^{-1}$ . The beam spot on the slab was about 30 mm diameter.

The measurement principle was basically the same as in PNPI. Two small counters S1, S2 switched in coincidence determined (roughly) the hit position area on the slab. In these measurements, the S1, S2 scintillators with dimensions of  $1 \times 1 \times 1 \text{ cm}^3$  were used. These small scintillators were viewed with the PMTs 187. Since no tracking system was used the contribution on the timing resolution from the hit position uncertainty was larger than in the PNPI tests being estimated as  $\sigma \approx 25 \text{ ps}$ .

The scintillation slab with PMTs situated at the COSY test beam is shown in Fig. 5.24. An option was foreseen to move the slab perpendicular to the beam (along the  $x$ -direction in terms of the coordinate system defined above).

The TRB-2 version was used for the readout. The width of the TDC channel was reduced to 24 ps in order to minimize contribution to the timing resolution from the readout electronics. In the 24 ps per channel mode, the TRB-2 board had 32 input

**Figure 5.24:** View of the test measurement setup up at Jessica area at COSY**Figure 5.25:** The TRB-2 based readout electronics scheme used at COSY test beam

channels with 4 of them connected to the output analog signals of PMTs S1,S2,S3,S4 (Fig. 5.25). The scheme provided coincidences of at least 2 of 4 signals from these counters. The TRB-2 produced the output  $n \times 40 \text{ mV}$  signal with  $n$  the number of counters in coincidence. The 4FC discriminator (production of PNPI) with threshold 50 mV activated the TRB-2 to store the event information under the condition  $n > 1$ .

Having stored 100 MB (250 MB for TRB-3) the accumulated data were transferred to a computer.

The timing resolution of the small counters viewed with PMTs 187 was found to be at the level of  $\sigma = 70 \text{ ps}$ . The uncertainty in the hit position was somewhat larger than that in the PNPI measurements. The timing resolution of the S3 and S4 PMT ranges from 120 to 170 ps depending on the slab position with respect to the beam (slab  $x$ -position). Despite the different experimental conditions this result was not far from that measured in PNPI with a similar slab.

### 5.2.8 Comments on the necessity of hit position measurements and time resolution

As discussed above the required time resolution better than 100 ps is obtained provided the hit position on the slab is measured with a precision of  $\sigma = 2$  mm. In the  $\bar{P}$ ANDA Forward Spectrometer, the information on the track (hit) position is assumed to be obtained with the help of the Forward Tracking system (FT). By a coarse estimation made without taking into account multiple scattering, an expected space resolution ( $\sigma$ ) in the vertical direction (along the scintillation slab) is about 5 mm which would worsen the obtained numbers of time resolution by  $3 \div 5\%$ . The multiple scattering of 1 GeV protons enlarges  $\sigma$  to 11 mm which translates into a timing uncertainty of 58 ps (!). This deterioration of the space and time resolution is mostly due to material budget of the Forward RICH detector located upstream of the FToF wall.

In principle, one may use the combination of TDC data based only on the time-of-flight without the information on the hit position but containing only the amplitude walk uncertainties of the counters 2, 3 and 4-”mean-time variant”. In a simplified form, one can write:

$$\begin{aligned} T_3 &= T_2 + t + \tau_3 \\ T_4 &= T_2 + t + \tau_4, \end{aligned}$$

where  $\tau_3$  ( $\tau_4$ ) is the time of propagation of photon bunch through the plastic scintillator from the particle hit position to the counter 3(4) photocathode,  $t$  is the time-of-flight of the particle between the start counter 2 ( $T_2$ ) and the scintillation slab. It is obvious that  $\tau_3 + \tau_4 = \tau$  is constant depending on the length of the scintillator and properties of scintillator material. Combining the sum  $T_3 + T_4$  one can write  $2t = (T_3 - T_2) + (T_4 - T_2) = T_3 + T_4 - 2T_2$ . Here all not essential for the time resolution delays which assumed to be constant, e.g.,  $\tau$ , are omitted. We select here start counter 2 with the resolution estimated to be 49 ps (which is somewhat better than that of the start counter 1).

The time resolution provided by the sum  $T_3 + T_4$  is

$$\sigma_{34} = \frac{1}{2} \sqrt{\sigma_3^2 + \sigma_4^2 + 4\sigma_2^2}. \quad (5.6)$$

Here  $\sigma_3, \sigma_4$  represent the time resolutions of the counters 3 and 4. As one can see, the time start uncertainty ( $\sigma_2$ ) dominates the time resolution in the mean-time variant Eq. 5.6.

Symmetrically, one may build a combination not comprising either time-of-flight  $t$  or start counter but containing information on the hit position:  $\Delta\tau = \tau_3 - \tau_4 = T_3 - T_4$ . Thus, the hit position in the center of slab would correspond  $\Delta\tau = 0$ . The dispersion of  $T_3 - T_4$  represents the net time uncertainty related to the counters 3 and 4:  $\sigma_{34-} = \frac{1}{2} \sqrt{\sigma_3^2 + \sigma_4^2}$ . Remind that the weighted mean  $\sigma_{wm}$  (see above) is given by  $\frac{1}{\sigma_{wm}^2} = \frac{1}{\sigma_3^2} + \frac{1}{\sigma_4^2}$ .

An example of the discussed above combinations measured recently at the 920 MeV protons with the slab  $2.5 \times 5 \times 140$  cm<sup>3</sup> readout with R4998 PMTs at each end presented in Table 5.8.

Assume that the hit is in the middle of the slab and  $\sigma_3 = \sigma_4 = \sigma$ . In this case  $\sigma_{wm} = \sigma_{34-} = \sigma/\sqrt{2}$ . As seen from Table 5.8 the net mean time resolution is somewhat worse: 73.5 versus 64 ps.

The  $\sigma_{wm,start}$  column in Table 5.8 shows the real time resolution which can be achieved in time-of-flight measurements provided that the start signal has a dispersion at the level of 50 ps. As  $\bar{P}$ ANDA has no dedicated start counter it is subject to MC studies to estimate a real time resolution for each reaction under investigation. For example, if a start comes from the BToF detector one would expect  $\sigma_2 \approx 100$  ps and  $\sigma_{wm,start} \approx 100$  ps. It must be understood that the *effective offline time resolution* will depend on many factors like reaction kinematics, particle multiplicity, particle momenta etc. It is important to note, that FS tracking system must provide necessary hit position resolution as the time resolution in mean time variant ( $\sigma_{34}$ ) is substantially worse.

The combination  $\Delta\tau$  can be used to determine roughly the hit position internally without the FT information. The dependence of  $\Delta\tau$  on  $x$  is fitted very well with a linear function (Fig. 5.26). Using the slope parameter obtained in the fit one may determine the time needed for the propagation of a photon bunch from one end of the scintillator to the other:  $\tau_{sci} = 59.12$  ps/cm  $\times$  140 cm = 8276.8 ps. The average photon bunch velocity is  $v_b = 1/59.12 = 0.169$  mm/ps which is close to the speed of light in BC408 (0.1899 mm/ps).

Using the  $T_4 - T_3$  difference one can determine the hit position with a precision of  $\sigma_x = \sigma_{43}v_b$ , where  $\sigma_{43} \sim 85.5$  ps,  $\sigma_x \sim 14.5$  mm. This can only be used for a coarse estimation of the hit position on a scintillation slab.

**Table 5.8:** Time resolutions using the hit position correction in the time stamp measurements with the counter 3 and 4 and in the mean-time variant of the analysis. Here  $\sigma_{34-}$  and  $\sigma_{34}$  are dispersions of corresponding distribution  $(T_4 - T_3)/2$  and  $(T_4 + T_3 + 2T_2)/2$ , respectively,  $\sigma_3$  and  $\sigma_4$  are dispersions of the individual counters 3 and 4 measured with the hit defined and with the contribution from the start counter subtracted, the weighted mean  $\sigma_{wm}$  is defined in text,  $\sigma_{3,start}$ ,  $\sigma_{4,start}$ ,  $\sigma_{wm,start}$  are dispersions with contribution from the start counter 2 included,  $\sigma_2 = 49$  ps

$x$ (cm)	$(T_4 - T_3)/2$ (ps)	$(T_4 + T_3 + 2T_2)/2$ (ps)	$\sigma_{34-}$ (ps)	$\sigma_3$ (ps)	$\sigma_4$ (ps)	$\sigma_{wm}$ (ps)	$\sigma_{3,start}$ (ps)	$\sigma_{4,start}$ (ps)	$\sigma_{wm,start}$ (ps)	$\sigma_{34}$ (ps)
60	1503.5	11580	90	61	158	57	78.2	165	70.7	133
40	2770.5	11510	74	80	111	65	93.8	121.3	74.2	123
20	3904	11630	90.5	96	109	72	107.8	119.5	80.0	133.4
0	5025	11580	73.5	84	99	64	97.2	110.5	73	122.5
-20	6255	11630	81.5	111	75	62	121.3	89.6	72	127.5
-40	6890	11560	84	125	68	59	134.2	83.8	71	129
-60	8655	11600	85.5	147	57	53	155	75.1	67	130

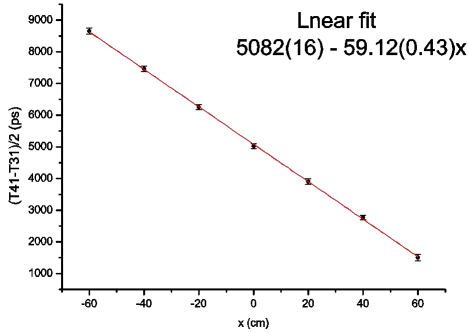


**Figure 5.26:**  $(T_4 - T_3)/2$  versus  $x$  with linear fit

### 5.3 Summary of experimental study of prototypes

Here we summarize the results of the prototype tests using the test station and proton beams. At the test station, an attempt has been undertaken to measure the “net” time resolution of a photodetector selected for the FToF. Several types of PMTs have been tested with a high enough amount of photons ( $\sim 10^4$ ) irradiated the PMT photocathodes.

After the amplitude corrections and subtraction of the contributions from electronics ( $\sigma_{el}$ ) and electron track position ( $\sigma_s$ ) uncertainties it has been obtained that for all the investigated PMTs the

time resolution ( $\sigma$ ) ranges from 45 to 65 ps. The best time resolution was observed for two types of Hamamatsu PMTs: R4998 1” and R2083 2”. They had been selected for prototyping using proton beams with plastic scintillators of 140 cm length and various widths and thicknesses. In addition the PMT 187 (Electron firm) has also been probed at the proton beams without a pre-test at the test station.

The energy of the proton beams used for the prototyping was in the energy range from 740 to 2000 MeV. The corresponding stopping power in plastic scintillators ranged from 2.5 to 2.1 MeV  $g^{-1} cm^2$ , respectively. The latter numbers are close to those for a MIP particle. In distinction from the tests with a small plastic scintillator at the test station, the number of photons at the PMT photocathode of a large counter varies strongly depending on the track position in the scintillation slab. For a MIP particle, the number of photons at photocathode may reach  $2.5 \times 10^4$  if the particle track crosses the scintillator close to the PMT and decreases significantly if the track crosses at far end of the slab (Sec. 3.3, Fig. 3.4). The time resolution varies respectively being worse than 100 ps in the last case. However, the overall resolution defined by the weighted mean of both (independent) measurements at opposite sides of the slab was always better than 80 ps.

The time resolution of a particular PMT was calculated on the event basis using raw TDC and QDC information together with the proton track position information in the slab measured with the help of multi-wire proportional cham-

bers. The correction for the pulse amplitude and hit position was made and a contribution from the small start counter S1 (or S2) to the time resolution was subtracted.

The main outcomes of PMT studies are itemised below:

1. The time resolution of 60 - 65 ps was obtained for the scintillation counters recommended for prototypes for the FToF wall.
2. The time resolution of 50 ps was obtained for the slabs of 2.5 cm width. A practical application of such slabs however would result in increase of the number of channels which may confront the detector cost limitation.
3. The time resolution of 80 ps was obtained for the scintillation counter based on the slab of 2.5 cm width viewed with the Electron PMT 187. These mesh PMTs can operate in magnetic fields up to 0.5 T without a deterioration of the time resolution.
4. Samples with slabs of 1.5 cm thickness originally projected for the FToF wall showed essentially worse time resolution than those of 2.5 cm thickness.
5. A precise measurement of the hit position is crucial to get the timing resolution on the level of 60 ps. It has been demonstrated that without independent information on the hit position the best timing resolution which can be achieved is twice worse.

The prototype samples of interest investigated at proton beams are listed in Table 5.9.

The vertical dimension of the scintillation slabs in Table 5.9 was dictated by the requirements of the FS vertical acceptance. The scintillator thickness of 2.5 cm was optimized in a dedicated experiment (Fig. 5.21). The selected granularity (slab width) was defined proceeding from PANDAROOT MC study fulfilling the condition that counting rate per a scintillation slab should stay below 1-2 MHz (Sec. 4). The count rate drops down in the horizontal direction left and right from the FS spectrometer axis. The last counters left and right in the side parts of the wall counts about 1/70 of the count in the central part. This limitation comes from an admitted width of the FToF wall and effective acceptance of the FT system to detect low momentum particles strongly deflected by the FS dipole magnet.

It should be noted that the time resolutions presented in Table 5.9 are obtained with a negligible contribution from the track hit position uncertainty ( $\sim 1$  mm) and with time uncertainty of the start counter subtracted. In other words, they are "net" time resolutions.

The selection of the Hamamatsu R2083 and R4998 PMTs was mostly based on the test station measurement results. The selected samples demonstrate excellent performance. One should keep in mind, however, a possible progress in the PMT technology now and in the future.

Having in mind the future Dipole TOF detector, various applications of the photodetectors which could stand against a strong magnetic field has been investigated.

The "Electron" PMT 187 is hardly applicable for the dipole ToF subdetector as the level of the magnetic field inside the dipole is essentially higher than 0.5 T. An alternative choice might be a SiPM matrix. The timing characteristics of SiPMs were tentatively investigated using the PNPI test station. A satisfactory result was obtained for KETEK PM6660 samples. A raw timing resolution of  $\sigma = 71$  ps (per a SiPM sample) was directly measured, and after the corrections it was obtained  $\sigma_{PM6660} = 66$  ps.

A big advantage of SiPMs is that they can operate in high magnetic fields. The KETEK 6660 has an active area of  $6 \times 6$  mm<sup>2</sup>, geometrical efficiency of 40% and gain  $\sim 10^7$ . It looks like that, presently, the SiPM matrices are the only option to build the dipole ToF detector. However, more R&D is needed. Thus we could not find an information about aging of these detectors. A thorough study of the SiPM radiation hardness is of particular importance.

A very tentative test of the radiation hardness of SiPMs has been made in PNPI using not powered S0931-50p SiPM ( $3 \times 3$  mm<sup>2</sup>) sample exposed to 1 GeV proton beam. It was found that the radiation dose equivalent to  $0.45 \times 10^{11}$  protons having passed through the active area of the sample is crucial for its operation capabilities. More detailed information on the radiation hardness of the SiPMs is needed together with a radiation dose map inside the PANDA dipole magnet.

To conclude,

- BC408 plastic scintillator is selected for the FToF wall. Measured in beam tests light attenuation along the slab made of BC408 corresponds to specification;

**Table 5.9:** Prototype samples with experimentally obtained timing resolution calculated as weighted mean for large scintillators

Scintillation slab dimensions (cm)	PMT	Timing resolution $\sigma$ (ps)	Comment
$140 \times 10 \times 2.5$	Hamamatsu R2083 (both ends)	63	Recommended for a prototype for the FToF wall
$140 \times 5 \times 2.5$	Hamamatsu R4998 (both ends)	60	Recommended for a prototype for the FToF wall
$140 \times 2.5 \times 2.5$	Hamamatsu R4998 (both ends)	43	Variant of prototype with smaller scintillator width
$140 \times 5 \times 1.5$	Hamamatsu R4998 (both ends)	$\approx 88$	Projected originally for the FToF wall
$140 \times 2.5 \times 2.5$	Electron 187 (both ends)	78	Magnetic field protected, tentatively projected for the dipole ToF
$1 \times 1 \times 1$	Electron 187, Hamamatsu R4998	49	“net” timing resolution of one PMT

- Two types of fast Hamamatsu PMTs are selected for the FToF wall as they have demonstrated the best performance both at the test station and on beam tests;
- The scintillator thickness has been experimentally optimized. It is selected for the FToF to be of 2.5 cm. The beam tests showed that smaller thickness resulted in worse time resolution (Table 5.8);
- The measured average velocity of photon bunch propagation along the the BC408 scintillator is 0.169 mm/ps. In order to minimize a corresponding time uncertainty the particle hit position must be measured with a precision of a few mm. Then one may guarantee the time resolution better 100 ps;
- Without the hit position measurement, the FToF wall can provide time resolution on the level of 120-130 ps (mean time variant).

## 5.4 Outlook for further experimental studies

It is planned to continue the high time resolution investigations of the prototype using a fast UV laser and (if necessary) the 1 GeV proton beam of the PNPI accelerator. The Picosecond Pulsed Diode laser PDL-800, available at the PNPI since June 2017, provides excellent conditions for measurements with a good simulation of the light

pulse produced by a real particle. It also allows to control the pulse amplitude and length (down to 50 ps), to change the laser frequency from a single shot to 40 MHz, to vary pulse power, etc. A room with the necessary infrastructure is available. A mechanical mount to work with the large scintillation blocks is in process of fabrication.

A first test has already been done with the PDL-800 irradiating a small scintillator coupled with a PMT Hamamatsu R4998. A time resolution of about 40 ps has been obtained.

A number of tasks are planned to perform using the system based on the PDL-800:

- Optimization of PMT parameters together with optimization of the active divider
- Detailed studies with the proposed sizes of the scintillation slabs. Comparison of the Bicron408 and EJ200 characteristics
- Measurements of the attenuation lengths of the large scintillators
- Experimental study of the light guides with large scintillators (comparison to Monte Carlo analysis, section 4.6)
- Measurements with readout electronics boards in the final configuration
- Final adjustment to the PANDA experiment requirements

## References

- [1] S.L. Belostotski et al. Test of scintillation counter for the PANDA time-of-flight detector at 730 MeV proton beam. *Preprint-PNPI*, 2010.
- [2] N. Rabin. Status and possibilities of the time-of-flight measurement technique using long scintillation counters with a small cross section. *Instrum. Exp. Tech.*, 50:579–638, 2007.
- [3] W. Braunschweig, E. Konigs, W. Sturm, and W. Wallraff. A Large Area Time-Of-Flight System with a Resolution of 0.5 ns fwhm. *Nucl. Instrum. Meth.*, 134:261–266, 1976.
- [4] T. Tanimori, T. Kageyama, K. Nakamura, M. Yoshioka, J. Haba, H. Kawai, M. Kobayashi, T. S. Nakamura, and N. Sasao. A TEST OF 150-CM X 20-CM WIDE TIME-OF-FLIGHT SCINTILLATION COUNTERS. *Nucl. Instrum. Meth.*, 216:57–65, 1983.
- [5] O. V. Miklukho et al. Polarization in quasi-elastic (p, 2p) reaction on  $^7\text{Li}$  nucleus in complete kinematics at 1 GeV. *Nucl. Phys.*, A683:145–156, 2001.
- [6] V. A. Andreev et al. Polarizations for proton knockout reactions from s(1/2) orbits at 1-GeV. *Phys. Rev.*, C69:024604, 2004.
- [7] O. V. Miklukho et al. Polarization effects in the quasi - elastic ( $p, 2p$ ) reaction with the nuclear S-shell protons at 1 GeV. *Phys. Atom. Nucl.*, 76:871–880, 2013.
- [8] S.L. Belostotskii, G.D. Alkhazov, G.M. Amalskii, A.A. Verobev, and Yu.V. Dotenko. Use of Extracted Synchrocyclotron Beam to Investigate Scattering of 1-GeV Protons by Nuclei. *JETP Lett.*, 17/2:101.
- [9] S.M.Seltzer and M.J.Berger. Energy loss straggling of protons and mesons. *Studies in Penetration of Charged Particles in Matter, Nuclear Science Series*, 39, 1964.
- [10] I. Fröhlich et al. TRB for HADES and FAIR experiments at GSI. In *Astroparticle, particle and space physics, detectors and medical physics applications. Proceedings, 10th Conference, ICATPP 2007, Como, Italy, October 8-12, 2007*, pages 973–977, 2008.



## 6 Calibration and monitoring

The FToF counter is dedicated to measure the time stamp  $t$  corresponding to a particle passing through the sensitive area of the FToF wall. Note that the crossing time through the scintillator (of 2.5 cm thickness) is not zero. For relativistic particles the  $\Delta t$  to cross the scintillator is 75 ps. We determine the time stamp position by crossing the upstream surface of the scintillator. The time  $t$  is counted from some reference signal (PMT1 or PMT2) as conditionally shown in Fig. 6.1. The scintillation bar is read out from both ends with PMT3 and PMT4.

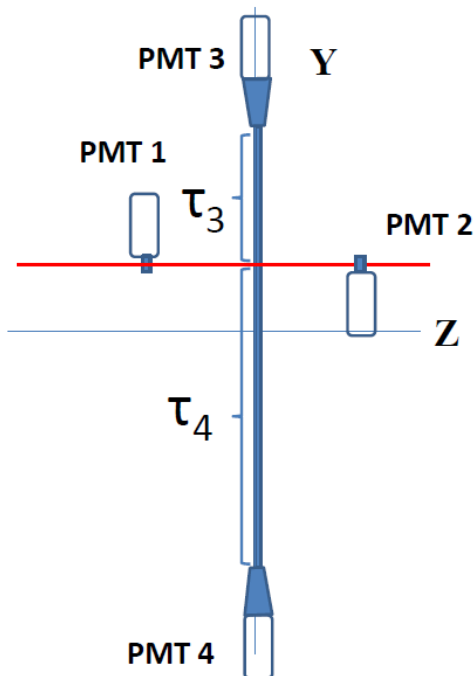


**Figure 6.1:** Calibration scheme of a large scintillation slab

One can write in a simplified way

$$T_3 = t + \tau_3 + \delta_3 + d_3$$

$$T_4 = t + \tau_4 + \delta_4 + d_4$$

Here  $T_3$  ( $T_4$ ) is the time difference measured with TDC3 (TDC4) between a STOP signal from the PMT3 (PMT4) and the START signal from a reference counter (e.g. PMT1),  $\tau_3$  ( $\tau_4$ ) is the effective time of the light pulse to reach the PMT3 (PMT4) photocathode,  $\tau_3$  ( $\tau_4$ ) contains the fluctuating part of  $T_3$  ( $T_4$ ) related to fluctuations

of the number of photoelectrons, fluctuations of transition time in PMT(s), readout electronics resolution, etc.,  $d_3$  ( $d_4$ ) includes all latencies in a given channel (cables, PMT transition time, electronics) which may slowly vary due to temperature change and other external environmental conditions. The value of  $\tau_3 + \tau_4 = \tau$  has been measured using  $T_3 - T_4$  difference for the prototype sample slab of  $140 \times 5 \times 2.5$  cm<sup>3</sup> made of BC408: it has been found  $\tau = 8277$  ps and light pulse velocity  $v = 0.169$  mm/ps (Sec. 5.2). These values are to be specified for each individual counter.

Here we first consider "on beam" calibrations using particles produced off the  $\bar{P}$ ANDA spectrometer target. In principle, the value of  $\tau_3$  ( $\tau_4$ ) can be determined provided the hit position is independently measured. This information could come from the FS tracking system. An expected contribution to the time resolution from the hit position uncertainty is however not small in this case (10 to 50 ps). In order to exclude this uncertainty one may build the sum

$$T_3 + T_4 = 2t + \tau + \delta_3 + \delta_4 + d_3 + d_4 = 2t + \tau + \delta + d$$

where  $\tau = \tau_3 + \tau_4$ ,  $d = d_3 + d_4$  (meantime variant).

Assume that a bunch of events with known  $t_i$ , where  $i$  is event number, is used for the calibration (determination of all latencies). Unknown latencies can be then found as

$$\hat{\delta} + d = \hat{T}_3 + \hat{T}_4 - 2\hat{t} - \tau$$

Where  $\hat{\delta}$ ,  $\hat{T}_3$ ,  $\hat{T}_4$  and  $\hat{t}$  are averaged over the data sample. Note that individual values of  $d_3 + \hat{\delta}_3$ ,  $d_4 + \hat{\delta}_4$  can be determined using additional equation

$$\hat{T}_3 - \hat{T}_4 = \frac{2x}{L}\tau + (d_3 + \hat{\delta}_3) - (d_4 + \hat{\delta}_4)$$

Here  $x$  is hit position (counted from the center of slab),  $L$  is slab length.

It must be noted that the average value of  $\delta_3$  ( $\delta_4$ ) is not zero. In the TOT (time over threshold) variant of readout electronics, the average value of the time walk depends on the pulse amplitude. The latter is proportional to the energy deposit in the scintillator which, according to our expectations, varies from 5 to 50 MeV (Sec. 3.3). Therefore the

$\delta_3(\delta_4)$  calibration must be performed at several points within this dynamic range and at various electronic thresholds.

Calibration using elastically scattered  $\bar{p}$ . The elastically scattered  $\bar{p}$  (protons in the case of HESR proton test beam) can be easily selected with the help of the dipole magnet. The momentum spread in the selected data sample for each scattering angle is on the level of 1% and time-of-flight per event ( $t_i$ ) is well defined. The energy deposit in the plastic scintillator is about 5 MeV (MIP). However, these protons are available for calibration at a high enough rate mostly for the central part of the detector (see Fig. 4.16 in Sec. 4).

Calibration using inclusively produced hadrons. The protons and pions unclusively produced are much less peaked at small angles (Fig. 4.10) and can be used for calibration of the side parts of the FToF wall together with FRICH information (provided that the particle momentum is higher than RICH threshold).

Calibration using  $\bar{\Lambda}$  decay  $\bar{\Lambda} \rightarrow \bar{p} + \pi^+$ . The  $\bar{\Lambda}$  peak is well seen after very modest selection criteria (Sec. 4.3), the event rate can reach a few kHz. The  $\bar{p}$  from  $\bar{\Lambda}$  decay are again strongly peaked at small angles while pions cover much wider angular range. It is important that the decay vertex would be reconstructed and both  $\bar{p}$  and pion momenta are well reconstructed.

Laser calibration. Modern picosecond lasers provide excellent opportunities for calibrations of multichannel time-of-flight systems. A possibility to vary light pulse amplitude would help to scan the dynamic range. A high repetition rate allows to study the saturation effects in PMTs. There are many commercially available suitable lasers. As an example, characteristics of Pil040 laser (405 nm) are listed below

	<b>PiLas</b>
Center wavelength	375 nm - 2 $\mu$ m
Pulse duration	20 ps - 1 ns variable
Pulse peak power	25 - 1000 mW
Pulse repetition rate	single shot - 120 MHz
Output	free space or fiber output
PER	> 23 dB
Timing Jitter	< 3 ps rms
Warm-up time	< 5 minutes
Size laser head	95 $\times$ 31 $\times$ 147 mm <sup>3</sup>
Size control unit	235 $\times$ 88 $\times$ 326 mm <sup>3</sup>
Power consumption	< 15 W
Weight laser head	0.45 kg
Weight controller	2.5 kg

A laser calibration system built of commercially available optical components is described in detail in [1]. Here we plan to build a similar system. The laser calibration may operate in beam pauses during data taking period and thus be used for a continuous monitoring of the ToF detector parameters. The laser light pulse passing through a splitter is delivered to the middle of a scintillation slab with the help of a 3 m optical fiber. The splitter serves to calibrate a multichannel system of the scintillation counters. All the optical components necessary for the calibration as well as the laser itself are included in the FToF cost matrix.

The cost estimation is included in the cost matrix of the FToF wall.

## References

- [1] R. Bertoni, M. Bonesini, A. de Bari, and M. Rossella. A laser diode based system for calibration of fast time-of-flight detectors. *JINST*, 11(05):P05024, 2016.

## 7 Project management

---

### 7.1 Responsibility

The FToF detector is designed, prototyped and tested in PNPI. The PNPI group is fully and the only one responsible for realization of this project. The project will be realized with the help of the PNPI Electronic department and Technical - Manufacturing department. The project is strongly supported by the PNPI administration.

The PNPI group involved in  $\bar{P}$ ANDA experiment consists of six physicists, PhD student, expert on FEE electronics and one technician. The PNPI suggested financial and infrastructure help in organization of the test station with a picosecond UV laser and space for mass production.

### 7.2 Work packages

As has been presented above, the FToF wall is to be assembled of standard modules those consisting of commercially procured elements (large scintillation slabs and PMTs). The supporting structure is to be designed and fabricated in PNPI. The readout electronics will be based on PADIWA interface and TRB-3 modules being currently worked out in GSI. Expertise of the GSI electronic group is (will be) very helpful.

The project is planned to organize (in work packages -WPs) as follows in Table 7.1.

### 7.3 Timelines and milestones

Timelines are presented in Table 7.2. It is planned that the FToF wall detector will be built in the PNPI. All the commercially available components will be delivered to the PNPI, assembled and tested there. The system is modularized: one block consists of a scintillation slab, two fast PMTs and an optical connector in the middle of the slab. The tests of an individual module will be organized with the help of the fast UV-laser (Laser head LDH-P-C-3758, Laser driver PicoQuant PDL 800-B):

- Wavelengths between 375 nm and 1550 nm
- Pulse widths as short as 70 ps (FWHM),
- Time stamp at 3 ps precision,
- Peak power up to 1 W,
- Repetition rate from single shot to 80 MHz.

The laser is available since recently in the PNPI.

As far as the UV laser is planned to be in common use (e.g. for R3B tests) the FToF calibration system is based on a dedicated laser PiLas as described above.

The readout electronics will be the PADIWA and TRB-3 (FPGA platform) according to the prototyping presented in the TDR. All the mechanical components will be fabricated in the PNPI.

**Table 7.1:** Work packages and responsibilities

WP	WP content	Involved groups, organizations
WP1	HV system together with PMT dividers	PNPI Electronics Division
WP2	Laser calibration system	PNPI Electronics Division
WP3	FPGA based frontend electronics	GSI, Darmstadt, PNPI
WP4	PMTs and plastic scintillators	Hamamatsu, Bicron, other relevant firms
WP5	Mechanical components: supporting frame, patch panels, PMT housings	PNPI Design division, PNPI Workshop
WP6	PANDAROOT MC studies: benchmark reactions in time-dependent MC-simulations. FToF wall time resolution and PID	

**Table 7.2:** Timelines and milestones

TDR presented to $\bar{P}$ ANDA collaboration	12.2016
Organization of working place for assembling and tests of scintillation counter modules in PNPI	01.2017 - 12.2018
Approval of TDR by FAIR [M3]	06.2018
Prepare funding request	06.2018 - 03.2018
Funding established	03.2019
Tendering	03.2019 - 12.2019
Prepare contract	04.2019 - 11.2019
Contract is signed [M4]	12.2019
Tender completed	12.2019
Prepare manufacturing concept and documentation for tests and mass production	01.2019 - 12.2019
Procurement of necessary equipment for tests and calibrations (components not yet available)	06.2019 - 12.2019
Procurement materials for mass production (scintillators, PMTs, etc)	06.2019 - 12.2019
Preparation of drawings for mechanical items. Fabrication of mechanical items.	06.2018 - 12.2019
Mass production. Assembly, tests and calibration of scintillation modules	01.2020 - 06.2021
Preassembly of the FToF wall	06.2021 - 12.2021
Shipment to GSI	01.2022 - 06.2022
Integration in $\bar{P}$ ANDA detector [M11]	06.2022 - 06.2023
Pre-tests, on beam tests [M12]	06.2023 - 12.2023

## 8 Conclusion

---

We presented here the design, experimental tests and Monte Carlo simulation studies of the FTOF wall sub-detector dedicated to measure the event start  $T_0$  and time-of-flight of hadrons in the Forward Spectrometer of the  $\bar{\text{P}}\text{ANDA}$  experiment. The FTOF wall is situated at 7.5 m downstream the interaction point. It covers practically all acceptance of the Forward Spectrometer. According to design considerations, the wall can be built using commercially available plastic scintillators, photomultiplier tubes and other optical components. The FEE electronics is based on the FPGA platform (TRB-3 and PADIWA) developed in GSI.

The experimental tests performed with 920 MeV protons have demonstrated that the proposed scintillation wall meets all the requirements of the  $\bar{\text{P}}\text{ANDA}$  experiment. The experimentally measured (offline) time resolution was obtained to be  $\sigma \approx 70$  ps. The time lines for detector construction complies with general  $\bar{\text{P}}\text{ANDA}$  planning.

## Acknowledgments

We acknowledge financial support from the Russian funding agency "State Corporation for Atomic Energy Rosatom", the administration of the High Energy Physics Division of the B. P. Konstantinov Petersburg Nuclear Physics Institute of National research Center Kurchatov Institute, the Forschungszentrum Jülich GmbH.

We are grateful to Dr. M. Traxler for his help in tuning and development of the TRB-3 platform for the FToF detector. We are grateful to the accelerator crews of the PNPI and Jülich IKP for their help in organization of on-beam tests. In particular, we are grateful to Prof. J. Ritman for his help in providing our experimental studies with necessary materials and for very useful discussions. We are grateful to Dr. H. Orth for his valuable advises on TDR drafting. Especially, we are grateful to Dr. Anastasios Belias for his very useful help in drafting this document.